A Precise Measurement of the $\pi^+ \to \pi^0 e^+ \nu$ Branching Ratio

Weidong Li
Mudanjiang, China

B.S., Jilin University, 1992
M.S., Jilin University, 1997

A Dissertation presented to the Graduate Faculty of the University of Virginia in Candidacy for the Degree of Doctor of Philosophy

Department of Physics
University of Virginia
May, 2004

Abstract

A precise measurement of the pion beta decay branching ratio allows an accurate testing of the unitarity of the Cabbibo-Kobayashi-Maskawa (CKM) quark mixing matrix, of the Conserved Vector Current Hypothesis, and of the radiative corrections. The PIBETA collaboration set out to measure this branching ratio with an accuracy of better than 0.5%, using a detector specifically designed and a experiment scheme optimized for this measurement. The first phase of data taking was finished by the end of year 2001 and more than 60,000 pion beta decay events were collected. This work describes the main points of the experiment and the results of a comprehensive data analysis. The measured branching ratio for the decay $\pi^+ \to \pi^0 e^+ \nu$ is: $\Gamma_{\pi\beta} = (1.032 \pm 0.004\,(\mathrm{stat.}) \pm 0.005\,(\mathrm{sys.})) \times 10^{-8}$ is found to be in excellent agreement with the CVC hypothesis and CKM unitarity.

Acknowledgments

I would like to thank my research adviser Dr. Dinko Počanić for his inspiration and direction throughout my research in the PIBETA collaboration. His knowledge, enthusiasm, and careful advice have been a very positive and helpful influence for these years. I would also like to thank Dr. Emil Frlež for sharing his expertise on numerous topics, his invaluable advice and help in the author's research can not be over-stated. Many thanks to Dr. Heinz-Peter Wirtz for his advice in maintaining experiment and the knowledge of DSC and hardwares the author learned from him. I would also like to thank Dr. Stefan Ritt for his tremendous help in software and computer knowledge. Thank you Maxim, Brent and Ying for wonderful time we spent as a group and enlightening discussions we had.

I would like to thank all the PIBETA collaborators who have created such a pleasant and productive group. I would also like to thank my wife Yonghong, without her encouragement, support and understanding, this work can not be done.

Contents

List of Figures

List of Tables

Chapter 1

Introduction

Modern particle physics is based on the standard model of particles and their interactions which is summarized in table 1.1. According to this model, all matter is built from a small number of fundamental spin $\frac{1}{2}$ particles, or fermions: six quarks and six leptons and interactions are described in terms of the exchange of characteristic boson mediators.

In the Standard Model, electroweak interactions have $SU(2) \times U(1)$ as the gauge group, both the quarks and leptons are assigned to be left-handed doublets and right-

Table 1.1: the fundamental fermions and boson mediators

particle	flavor		
quarks	u	c	t
	d	s	b
leptons	e	μ	τ
	ν_e	ν_μ	ν_τ

Interaction	Mediator
strong	gluon, G
electromagnetic	photon, γ
weak	$W^{\pm}$, Z^0
gravity	graviton, g

handed singlets. The quark mass eigenstates are not the same as the weak eigenstates. The matrix relating these bases was defined for six quarks and called the Cabibbo-Kobayashi-Maskawa (CKM) matrix:

$$\begin{pmatrix} d' \\ s' \\ b' \end{pmatrix} = \begin{pmatrix} V_{ud} & V_{us} & V_{ub} \\ V_{cd} & V_{cs} & V_{cb} \\ V_{td} & V_{ts} & V_{tb} \end{pmatrix} \begin{pmatrix} d \\ s \\ b \end{pmatrix}$$

The CKM quark mixing matrix has a special significance in modern subatomic physics as a cornerstone of a unified and systematic description of the weak interaction phenomenology of mesons, baryons and nuclei. In a universe with three quark generations the present 3×3 CKM matrix must be unitary, barring certain classes of hitherto undiscovered processes not contained in the Standard Model. hence, an accurate experimental evaluation of the CKM matrix unitarity provides a sensitive test of new physics.

There are many relationships among the nine elements of the matrix that can be tested by experiment. One such test of unitarity is that the first row of CKM matrix should be unity,

$$|V_{ud}|^2 + |V_{us}|^2 + |V_{ub}|^2 = 1$$

V_{us} is obtained [1] from K_{e3} decays and yields $|V_{us}| = 0.2196 \pm 0.0023$. V_{ub} from Particle Data Group (PDG) [1] data is $|V_{ub}| = (3.6 \pm 0.7) \times 10^{-3}$, dominated by the theoretical uncertainty. The leading element, V_{ud}, only depends on quarks in the first generation and is the element that can be determined most precisely. It also is the dominant part which needs to be determined as accurately as possible.

The value of V_{ud} can be determined from three distinct sources: nuclear superallowed Fermi beta decays, the decay of the free neutron, and pion beta decay.

Nuclear superallowed Fermi beta decay ($0^+ \rightarrow 0^+$) depends uniquely on the vector part of the weak interaction and, in the allowed approximation, the nuclear matrix element for these transitions is given by the expectation value of the isospin ladder operator which is independent of any details of nuclear structure and is given simply as an $SU(2)$ Clebsch-Gordan coefficient. Thus, the experimentally determined $ft-$Values are expected to be very nearly the same for all $0^+ \rightarrow 0^+$ transitions between states of a particular isospin, regardless of the nuclei involved. To extract V_{ud} from experimental data, the procedure is to determine the $ft-$values for a variety of different nuclei having the same isospin, and then to test if they are self-consistent. Once passing the test, their average is used to determine a value for the weak vector coupling constant (G_V), and from it, V_{ud}. The result thus obtained [2] is:

$$|V_{ud}| = 0.9740 \pm 0.0005.$$

The unitarity sum is [2]

$$\sum_i V_{ui}^2 = 0.9968 \pm 0.0014$$

The experimental result for nuclear Fermi beta decay rates can be very accurate (the uncertainty contributed from experiment would be only 0.0001). The largest contributions to the $|V_{ud}|$ uncertainty are from nuclear structure dependent corrections and nucleus-independent part of radiative correction which have no easy solutions.

Free neutron decay has an advantage over nuclear decays since there are no nuclear-structure dependent corrections to be calculated. However, it is not purely vector-like but has a mix of vector and axial-vector contributions. Thus, in addition to a lifetime measurement, a correlation experiment is also required to separate the vector and axial-vector pieces. Both types of experiment present serious experimental challenges. The results obtained from free neutron decay experiments demonstrated this complexity. The unitarity sum can be $2.3\,\sigma$ above unity to $3.0\,\sigma$ below unity, as illustrated in following two results. [1]

$$\sum_i V_{ui}^2 = 1.0096 \pm 0.0044 \text{ (from Erozolimskii [3])}$$

and

$$\sum_i V_{ui}^2 = 0.9917 \pm 0.0028 \text{ (from Perkeo II [4])}$$

The uncertainty associated with $|V_{ud}|$ obtained by neutron decay is dominated by experimental results. With improving experimental technologies, the experimental uncertainty will decrease and eventually will be lower than the theoretical correction, which is common to both nuclear and neutron decays.

Pion beta decay has an advantage over nuclear beta decays in that there are no

[1] Although the Erozolimskii et. al. result was later retracted, the remaining neutron decay results are not in very good agreement. It is significant that the most accurate result from Perkeo II deviates significantly from the rest.

nuclear structure-dependent corrections to be made. It also has the same advantage as the nuclear decays in being a purely vector transition, $0^+ \to 0^+$, so no separation of vector and axial-vector components is required. The disadvantage, however, is the small decay rate of $\pi^+ \to \pi^0 e^+ \nu$, at the order of 10^{-8}, which presents a big experimental challenge.

The previous experiments measuring the pion beta decay branching ratio result in good agreement with the Standard Model but with rather large uncertainties. For example, Depommier et al. [5] used a carbon degrader and an active CH_2 target to stop 77 MeV pions at a rate of $\sim 3.5\times10^4$/s. Their calorimeter consisted of an array of eight lead-glass counters that covered 60% of the 4π solid angle. The radial thickness was equivalent to 6.8 radiation lengths. The detector efficiency was calibrated using the charge exchange reaction $\pi^- + p \to \pi^0 n$ (SCX) followed by $\pi^0 \to \gamma\gamma$ with a precision of 3.6 %. This way they obtained a branching ratio of $1.00^{+0.08}_{-0.1} \times 10^{-8}$.

Before this work, the experiment of McFarlane et al [6] had the best uncertainty on pion beta decay branching ratio of 3.8 %. This uncertainty translates to 1.7 % uncertainty on $|V_{ud}|$ and 3.2 % uncertainty on the unitarity sum. The McFarlane group used an intense pion beam (2×10^8/s) and measured the pion decay in flight. This helped to reduce the background positrons due to the Michel decay of the muon at the cost of a low detector acceptance for γ pairs from π^0 which is the signature of pion beta decay. For the calibration, they inserted either a liquid hydrogen target or a CH_2 target close to the pion decay region to obtain the energy scale, conversion efficiency and absolute timing of their apparatus by detecting monoenergetic π^0 s from either single charge exchange (SCX) or $\pi^+ + \mathrm{C} \to \pi^0 + \mathrm{X}$ ($\pi^- + \mathrm{C} \to \pi^0 + \mathrm{X}'$), respectively. The total number of pions was determined using the averaged counting rate of three monitors.

The high uncertainties associated with the above experiments are due to both a low total number of pion beta decay events and to the determination of the detector efficiency or acceptance. A measurement of the pion beta decay branching ratio with high precision requires both an intense pion beam which the accelerator in the Paul Scherrer Institut, Switzerland offers and a high detection efficiency our specifically designed PIBETA detector can provide.

To avoid the uncertainties associated with the determination of the pion rate and absolute acceptance of detector, the $\pi^+ \to \pi^0 e^+ \nu$ decay branching ratio was normalized against the $\pi^+ \to e^+ \nu$ decay, which is known to a precision of 0.3 % [7]. To utilize the maximum detector size (thus high acceptance), a stopped pion experiment scheme was adopted. The major difficulty was the large backgroud of positrons from the $\mu^+ \to e^+ \nu \overline{\nu}$ (Michel) decay. Howerver the Michel positron background can be well seperated with a good energy resolution of detector since the positron from $\pi^+ \to e^+ \nu$ has an energy of 69.78 MeV while the positron from Michel decay has an endpoint of 52.83 MeV. The Michel positron spectrum can be further supressed using its long life time of 2.2 μs, as opposed to 26 ns of pion life time. Furthermore, the signal from the hadronic interaction (mostly SCX) of pions was supressed by utilizing its time structure (10^{-23} s).

The work described in this thesis is a summary of the pion beta decay experiment carried out in the Paul Scherrer Institut, Switzerland, using its high intensity pion beam. The data analyzed at this stage give an uncertainty on the pion beta decay branching ratio of $\sim 0.6\,\%$.

Chapter 2

Theory of pion beta decay

2.1 Weak interaction and CVC hypothesis

2.1.1 Weak interaction

The weak interaction was first developed by Fermi in 1932 in explaining β decay. Inspired by the structure of the electromagnetic interaction, the invariant amplitude for β decay describing interaction 2.1 is formulated as:

$$A + B \rightarrow C + D \tag{2.1}$$

$$\mathcal{M} = G\left(\overline{\mu}_C \gamma^\mu \mu_A\right)\left(\overline{\mu}_D \gamma^\mu \mu_B\right), \tag{2.2}$$

where G is the weak coupling constant which remains to be determined by experiment; G is called the Fermi constant. Note that only the vector-vector form is shown in the

Eq. 2.2 which means parity is conserved. In 1956, Lee and Yang [10] made a critical survey of all the weak interaction data and proposed that parity is not conserved in the weak interaction. The cumulative evidence of many experiments [11] is that only the right-handed anti-neutrino and the left-handed neutrino are involved in weak interactions. The absence of the "mirror image" states, left-handed anti-neutrino and right-handed neutrino, is a clear violation of parity invariance. Also, charge conjugation, C, invariance is violated, since C transforms a left-handed neutrino state into a left-handed anti-neutrino state. From experimental results, the $V - A$ form of the weak interaction is developed which has a weak current form of

$$J_\mu = \overline{\mu}_C \gamma^\mu \frac{1}{2} \left(1 - \gamma^5\right) \mu_A, \tag{2.3}$$

and the weak interaction amplitudes are of the form:

$$\begin{aligned} \mathcal{M} &= \frac{4G}{\sqrt{2}} J^\mu J_\mu, \\ &= \frac{G}{\sqrt{2}} \left[\overline{\mu}_C \gamma^\mu \left(1 - \gamma^5\right) \mu_A\right] \left[\overline{\mu}_D \gamma_\mu \left(1 - \gamma^5\right) \mu_B\right]. \end{aligned} \tag{2.4}$$

Modern physics describes the weak interaction with $W^\pm$ and Z^0 vector bosons as mediators, thus the amplitude for the weak interaction mediated by $W^\pm$ is of the form [1]

$$\mathcal{M} = \left(\frac{g}{\sqrt{2}}\overline{\mu}_C\gamma^\mu\frac{1}{2}\left(1-\gamma^5\right)\mu_A\right)\frac{1}{M^2-q^2}\left(\frac{g}{\sqrt{2}}\overline{\mu}_D\gamma_\mu\frac{1}{2}\left(1-\gamma^5\right)\mu_B\right). \tag{2.6}$$

in which M is the mass of $W^\pm$ ($\sim 81\,\mathrm{GeV}$) and q is the momentum carried by the weak boson. $g/\sqrt{2}$ is a dimensionless weak coupling. For most situations (including our experiment), the momentum q is small relative to the mass of the W and Eq. 2.6 reverts to Eq. 2.4 with

$$\frac{G}{\sqrt{2}} = \frac{g^2}{8M^2}, \tag{2.7}$$

and the weak currents interact essentially at a point.

2.1.2 CVC hypothesis and $\pi^+ \to \pi^0 e^+ \nu$ decay

In the forms of the weak current for leptonic and hadronic interactions, a fundamental difference is seen between their associated currents:

$$\begin{aligned}\text{leptonic weak current:}\quad j_l^\mu &= \overline{\Psi}\gamma^\mu\left(1-\gamma^5\right)\Psi,\\ \text{hadronic weak current:}\quad j_h^\mu &= \overline{\Psi}\gamma^\mu\left(G_V - G_A\gamma^5\right)\Psi,\end{aligned}$$

where $G_A/G_V \sim 1.26$ and $G_V \sim 1$. It is striking that the G_V from hadronic β decay is almost the same as that from leptonic decay [12]. Hadrons interact strongly with the surrounding virtual pion field, and consequently it is to be expected that even

[1] The propagator, after summing over three spin states of weak interaction boson, is of the form

$$\frac{i\left(-g^{\mu\nu} + p^\mu p^\nu/M^2\right)}{p^2 - M^2}. \tag{2.5}$$

here we only discuss qualitatively.

if the fundamental coupling constants are the same for all interactions, the coupling constants for the particles that also have strong interactions should be screened off because of "renormalization effects" and assume an effective value which is different from the fundamental value. From this point of view, it is not surprising that the G_A is different for hadronic weak interaction and leptonic weak interaction. [2] It is a surprise, however, that the G_V from these two weak interactions is the same. The Conserved Vector Current (CVC) hypothesis was proposed by several physicists [13] to explain this phenomenon.

We start with the analogy with the electromagnetic interaction. There it was found that conservation of the electric current implied conservation of electric charge. If we compare the electron and the proton, these particles have experimentally the same value for their effective electric charge. Nevertheless, the proton interacts strongly with virtual π-mesons and even if we assume that the original or "bare" charges of the two particles are the same, one might expect that the effective charge of the proton should be smaller than the effective charge of the electron because the first quantity should be screened by virtual π-mesons created because of interactions. The usual explanation offered for this fact is that the electric charge fulfills an exact conservation law. Consequently, the possible virtual states that can be created from the proton must always involve such a configuration of π-mesons that the total

[2] A so-called Partial Conserved Axial Vector Current (PCAC) attempts to explain the small difference between G_A from hadronic weak interaction and leptonic weak interaction.

charge of the virtual state is exactly the same as the bare one-proton state. That is exactly what is required here. Regardless of the clouds of virtual particles around the n and p, the net weak charge is required to be constant. Therefore, assume there is a conserved vector current (CVC) for the weak interaction:

$$\frac{\partial (j^V)^\mu}{\partial x^\mu} = 0,$$

$$\left(j^V\right)^0 = \int_{(x_0=t)} dx^3 \left(j^V\right)^0 (x) = \text{constant}, \tag{2.8}$$

Suppose that j^V has a definite strong interaction symmetry; it transforms under I-spin as an I-spin vector. Thus suppose it has the symmetry of the isospin raising operator T^+. If this is true, then the same result should be obtained for matrix elements of j^V for any two processes a and b, if the initial state of a has the same I-spin symmetry as the initial state of b, and if the final state of a has the same I-spin symmetry as the final state of b.

The CVC hypothesis also assumes that the weak vector current j^V is part of the same current as the electromagnetic current multiplet. The electromagnetic current is spatially a pure vector current. However, as a function of I-spin, it is a mixture of I-spin vector and I-spin scalar. In order to give 1 for a proton and 0 for a neutron, it must be $\propto$ $(1 + \tau_3)/2$, The weak current is a mixture of V and A spatially but is a pure I-spin vector since it is a charged current. This assumption relates the spatial-vector and I-spin vector parts of the two currents. It says that, for this part, the electromagnetic current is a third component (neutral) and the weak current is a charged component of the same current. This implies a deep connection between the electromagnetic and the weak interactions.

2.2 $\pi^+ \to \pi^0 e^+ \nu$ decay and radiative correction

With the above assumptions, the rate of $\pi^+ \to \pi^0 e^+ \nu$ decay should be calculable, given the nuclear β-decay matrix elements. To state these assumptions mathematically, Eq. 2.8 implies the existence of a new contribution to the weak interaction Hamiltonian given by [15]

$$\begin{aligned} \delta H_1 &= g \int d^3x \left[\varphi_0(x) \frac{\partial \varphi^*(x)}{\partial x_\mu} - \varphi^*(x) \frac{\partial \varphi_0(x)}{\partial x_\mu} \right] \times \\ &\times \; \overline{\psi}_e(x) \gamma_\mu (1+\gamma^5) \psi_\nu(x) + \text{herm. conj.} \end{aligned} \tag{2.9}$$

where $\varphi(x)$ is the complex π-meson field. We find [15, 16]

$$\frac{1}{\tau_0} = \frac{G_\mu^2 \left|V_{ud}\right|^2}{30\pi^3} \left(1 - \frac{\Delta}{2M_{\pi^+}}\right)^3 \Delta^5 f\left(\epsilon, \Delta\right), \tag{2.10}$$

and

$$\begin{aligned} f\left(\epsilon, \Delta\right) &= \sqrt{1-\epsilon} \left(1 - \frac{9}{2}\epsilon - 4\epsilon^2\right) \\ &+ \frac{15}{2}\epsilon^2 \ln \frac{1+\sqrt{1-\epsilon}}{\sqrt{\epsilon}} - \frac{3}{7} \frac{\Delta^2}{\left(M_{\pi^+} + M_{\pi^0}\right)^2}. \end{aligned} \tag{2.11}$$

in which G_μ is the Fermi weak coupling constant determined in muon decay. Under the CVC hypothesis, $G_V = G_\mu V_{ud}$ obtained from nuclear $0^+ \to 0^+$ β-decay can be applied to pion β-decay. G_V has a value of [2] $G_V/(\hbar c)^3 = 1.1136 \pm 0.0006\,\mathrm{GeV}^{-2}$. $\Delta = m_{\pi^+} - m_{\pi^0} = 4.5936 \pm 0.0005\,\mathrm{MeV}$ from PDG02 [1]. $\epsilon = m_e^2/\Delta^2$. $M_{\pi^0} = 134.9766 \pm 0.0006\,\mathrm{MeV}$. $M_{\pi^+} = 139.57018 \pm 0.00035\,\mathrm{MeV}$. The branching ratio is thus calculated to be

$$R = \frac{\tau_{\pi^+}}{\tau_0} = (1.0048 \pm 0.0012) \times 10^{-8}. \tag{2.12}$$

Therefore, the measurement of the $\pi^+ \to \pi^0 e^+ \nu$ decay branching ratio will test the CVC hypothesis. However, one must be cautious here even if the agreement is good. The reason is that the very existence of the rare decay $\pi^+ \to \pi^0 e^+ \nu$ is not a unique prediction of the conserved vector-current formalism. As soon as the π-mesons are strongly coupled to the nucleons one can always imagine a process where the π-meson forms a virtual nucleon-antinucleon pair. The virtual nucleon, e.g., then decays through the ordinary β-interaction and changes its own charge. The remaining nucleon annihilates again with the antinucleon with the emission of a π-meson. The π-meson in the final state will then have a different charge than the original π-meson. Since the strong interaction takes place very rapidly, the rate of such an anomalous decay is essentially determined by the rate of the β-decay of the virtual nucleon. Consequently, it is to be expected that any formalism of this kind will give a formula for the lifetime of the anomalous decay essentially equivalent to what we have developed here. Therefore the existence of the $\pi^+ \to \pi^0 e^+ \nu$ decay and the order of magnitude of the lifetime are not a confirmation of the CVC hypothesis. The characteristic features of this special formalism is rather the exact value (Eq. 2.12) for the branching ratio. Therefore, more accurate experiments are needed to decide whether or not the conserved current hypothesis is justified.

Radiative Correction

Eq. 2.12 did not include the radiative correction. The calculation of the radiative correction can be taken from the nuclear independent radiative corrections to $0^+ \to 0^+$ transitions in nuclear β-decay. At $O(\alpha)$, these corrections neglect the strong interaction effects in nuclear β-decay. This radiative correction function is based on a function $g(E, E_m, m)$ which has been derived by Sirlin [14] and takes the form

$$\begin{aligned} g(E, E_m, m) &= 3\ln\left(\frac{m_p}{m}\right) - \frac{3}{4} + 4\left[\frac{\tanh^{-1}\beta}{\beta} - 1\right] \times \\ &\times \left[\frac{(E_m - E)}{3E} - \frac{3}{2} + \ln\frac{2(E_m - E)}{m}\right] + \frac{4}{\beta} L\left(\frac{2\beta}{1+\beta}\right) \\ &+ \frac{1}{\beta}\tanh^{-1}\beta\left[2\left(1+\beta^2\right) + \frac{(E_m - E)^2}{6E^2} - 4\tanh^{-1}\beta\right]. \end{aligned} \tag{2.13}$$

where m is the electron mass, E_m is the electron end-point energy, p is the electron momentum, $\beta = p/E$, and $L(x)$ is the Spence function:

$$L(x) = \int_0^x \frac{\ln(1-t)}{t} dt. \tag{2.14}$$

when applied to pion beta decay and averaged over the electron spectrum, the function $\overline{g}(E_m, m)$ becomes [17]

$$\overline{g}(E_m, m) = \frac{\int_{m_e}^{E_m} \frac{(E_m - E)^2 p_e E}{\left[1 + \frac{2m_{\pm}}{m_0}(E_m - E)\right]} g(E, E_m, m)\, dE}{\int_{m_e}^{E_m} \frac{(E_m - E)^2 p_e E}{\left[1 + \frac{2m_{\pm}}{m_0}(E_m - E)\right]} dE}, \tag{2.15}$$

where m_+ is the π^+ mass and m_0 is the π^0 mass. The calculation with Maple [18] yields $\overline{g}(E_m, m) = 8.9619$.

The radiative correction (δ_R) is derived by Marciano and Sirlin [19] and takes the form

$$\left\{1 + \frac{\alpha}{2\pi}\left[\ln\left(\frac{m_p}{m_A}\right) + 2C\right] - \frac{\alpha(m_p)}{2\pi}\left[\overline{g}(E_m) + A_g\right]\right\} S(m_p, m_z), \tag{2.16}$$

where $S(m_p, m_z)$ is a QED short-distance enhancement factor equal to 1.02256, and $\alpha(\mu)$ is is a running QED coupling which satisfies

$$\mu\frac{d}{d\mu}\alpha(\mu) = b_0\alpha^2(\mu) + \text{higher orders}, \tag{2.17}$$

such that $\alpha(0) = 1/137.089$ and $\alpha(m_p) = 1/133.93$. A_g is a small perturbative QCD correction estimated to be -0.34, and C is a nuclear structure-dependent correction which is 0 for $0^+ \to 0^+$ transitions. m_A is a low energy cutoff applied to the short-distance part of the γW box diagram, and ranges from 400 MeV to 1600 MeV. Using this range of m_A, the radiative correction to $0^+ \to 0^+$ transition rates is found to be between 1.0324 and 1.0340.

Other calculations using different models have essentially consistent results, e.g., Jaus [20] calculated the radiative correction using a light-front quark model and yielded $1 + (3.230 \pm 0.002) \times 10^{-2}$.

The total decay rate $1/\tau_{\pi\beta}$ can be separated into the uncorrected expression, denoted by $1/\tau_0$, and an overall factor as

$$\frac{\tau_{\pi^+}}{\tau_{\pi\beta}} = \frac{\tau_{\pi^+}}{\tau_0}\delta_R, \tag{2.18}$$

2.3 Kinematic variables

Values of kinematic variables used in the experiment are presented without detailed calculations [33].

$\pi^+ \to \pi^0 e^+ \nu$ ($\pi\beta$ decay)

$$\begin{array}{rcccr} 134.973 & \leq & E_{\pi^0}\,(\mathrm{MeV}) & \leq & 135.048 \\ 0.511 & \leq & E_e\,(\mathrm{MeV}) & \leq & 4.519 \\ 0.000 & \leq & E_{\nu_e}\,(\mathrm{MeV}) & \leq & 4.023 \end{array}$$

The maximum kinetic energy of the π^0 is about 75 KeV, this results in a spread of angles between the two γ's from π^0 decay. The maximum deviation from 180° is 3.8°. This also results in a spread of γ energy which is half of the π^0 mass ($m_{\pi^0}/2 = 67.49\,\mathrm{MeV}$) if the π^0 decays at rest.

$\pi^+ \to e^+ \nu$ ($\pi 2e$ decay) This two body decay yields $E_e = 69.273\,\mathrm{MeV}$.

$\pi^+ \to \mu^+ \nu_\mu$ this two body decay yields muon kinetic energy of $KE_\mu = 4.118\,\mathrm{MeV}$. Nearly all μ^+'s with this energy remain in the target.

Michel ($\mu^+ \to e^+ \nu \overline{\nu}$) decay.

$$\begin{array}{rcccr} 0.511 & \leq & E_e\,(\mathrm{MeV}) & \leq & 52.830 \\ 0.000 & \leq & E_{\nu_e}\,(\mathrm{MeV}) & \leq & 52.828 \\ 0.000 & \leq & E_{\overline{\nu}_\mu}\,(\mathrm{MeV}) & \leq & 52.828 \end{array}$$

The positron energy, E_e, distribution has the form:

$$\Gamma(\epsilon)d\epsilon \sim \left\{1 - \epsilon - \frac{2}{9}\rho\,(3 - 4\epsilon)\right\} \epsilon^2 d\epsilon. \tag{2.19}$$

where $\epsilon = 2E_e/m_\mu$, and ρ is equal to 0.75 in the event of exact V–A structure of the weak charged current [15].

Chapter 3

Beamline and Detector

3.1 Beamline

The experiment was carried out in the πE1 area in the Paul Scherrer Institut, Switzerland. The beam line layout is shown in Fig. 3.1 in which the E-target is a 60 mm long graphite production target, QTB51, QTH51, QTH53 are half-quadrupole magnets, ASZ51, ASY51, ASL51 are dipole magnets, QSL54, QSL53, QSL52, QSL51, QTB52, QTB51 are quadrupole magnets, KSG51 is the beam plug, FSH51 are vertical slits, FS51 are horizontal and vertical slits, FSH52 horizontal slits controlling momentum band acceptance.

The ring accelerator accelerates protons to an energy of 590 MeV. The $\sim$1.5 mA proton beam is transported along the primary proton channel to two target stations where pions and muons are generated and transported via secondary beam-lines to the

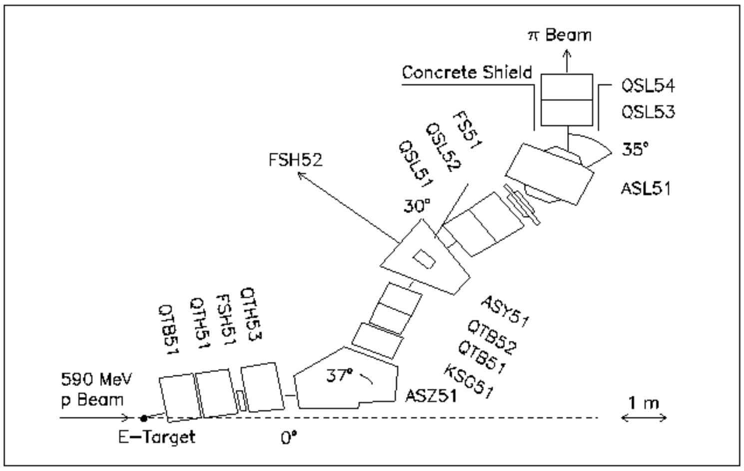

Figure 3.1: Beamline layout in πE1 area.

experimental areas. The accelerator operates at the frequency of 50.63 MHz producing a microscopic beam structure of 1 ns wide proton pulses separated by 19.750 ns.

After protons hit a graphite target, pions are extracted at an angle of 8° with respect to the incident protons. Operating in a high-flux optical mode, the πE1 beam line can deliver a pion beam with a maximum momentum of 280 MeV/c, a Full-Width-Half-Maximum (FWHM) momentum resolution of $< 2\%$ and an accepted production solid angle of 32 msr. The primary proton current in the ring cyclotron during the PIBETA data acquisition periods in the years 1999-2001 was 1.6 mA DC on average.

We have tuned the π^+ beam at the momentum 113.4 MeV/c with FWHM resolution $\Delta p/p \leq 1.3\%$ and maximum nominal π^+ beam intensity of $I_\pi = 1.4 \times 10^6 \pi$/s, reached at the full cyclotron current of 1.7 mA. The choice of a particular beam momentum is governed by the need for good time-of-flight (TOF) separation of pions, positrons and muons between the production target E and the first beam defining counter BC, as well as between the beam counter BC and the stopping target AT. The intensity is determined by the data acquisition time (computer dead time) and the beam profile spread in the target.

To reduce positron contamination due to the π's and μ's decaying in flight, a 4 mm thick carbon degrader is inserted in the middle of the ASY51 dipole magnet. Pions and positrons have different energy losses in the carbon absorber and are therefore spatially separated in a horizontal plane. Unfortunately, this also broadens the beam phase space. We have used TRANSPORT [21] and TURTLE [22] beam transport codes to develop a nontraditional beam optics with foci in both the horizontal and vertical planes at the FSH52 momentum-limiting slit. The resulting beam tune reduces the phase space broadening introduced by the carbon degrader. A significantly higher luminosity at the PIBETA target position is thus achieved and the pions are stopped in a laterally smaller region. Fig. 3.2 shows the beam tune as the output of the TRANSPORT program calculation. The TURTLE momentum spectrum of π^+'s incident on the front face of the degrader counter (AD) is shown in Fig 3.3.

The layout of the πE1 area following Fig. 3.1 is depicted in Fig. 3.4. A lead brick collimator PC with a 7 mm pin-hole located 3.985 m upstream of the detector center restricts the spatial spread of the incident π^+ beam. The beam particles are first

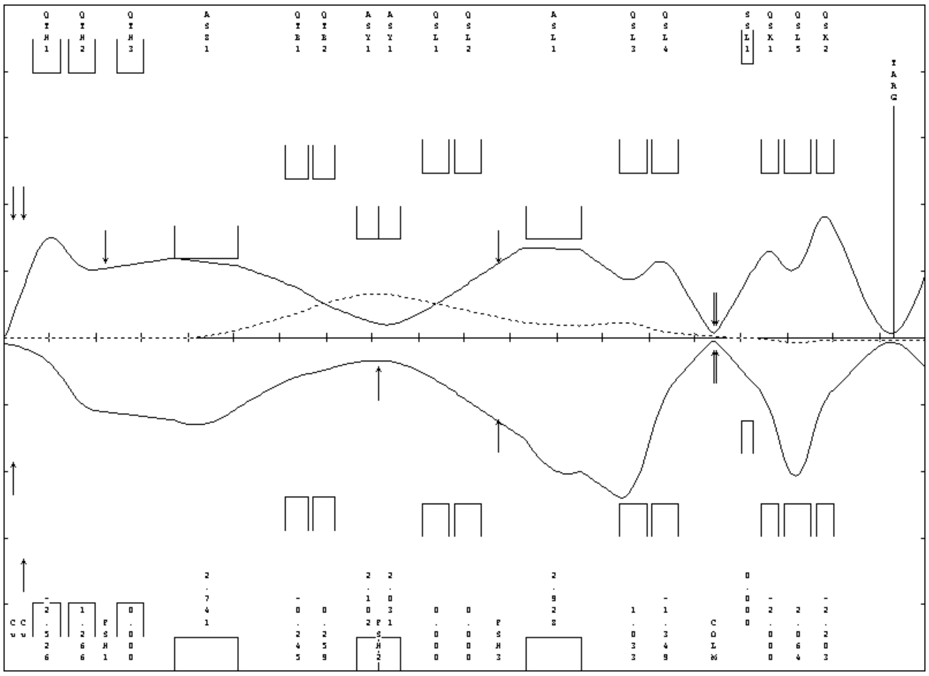

Figure 3.2: The beam tune from the TRANSPORT program calculation. The top part of the graph represents the x direction, and the bottom the y direction. Arrows indicate collimation, and the dotted line describes the beam momentum dispersion, measured in cm/%.

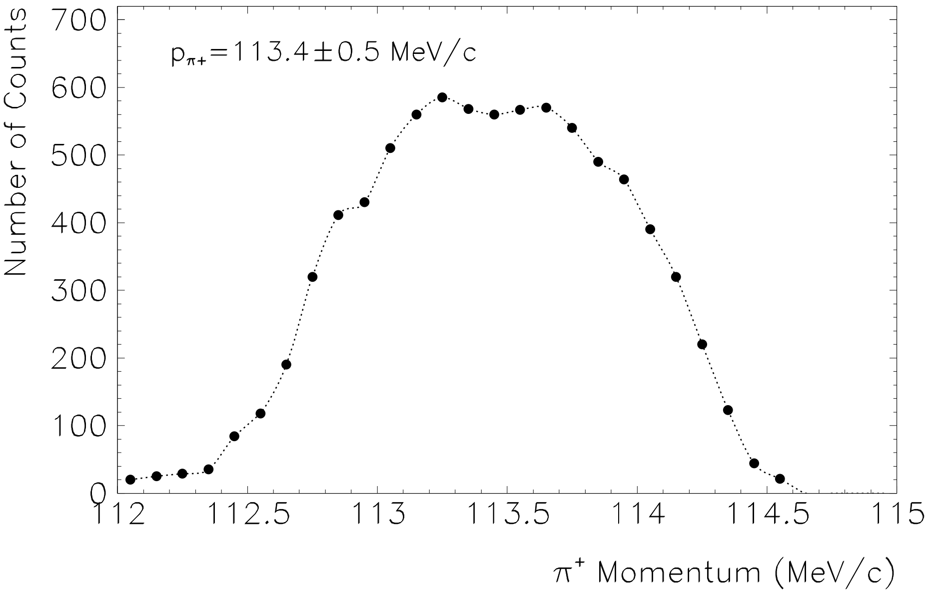

Figure 3.3: Momentum spread of π^+ beam in front of the degrader.

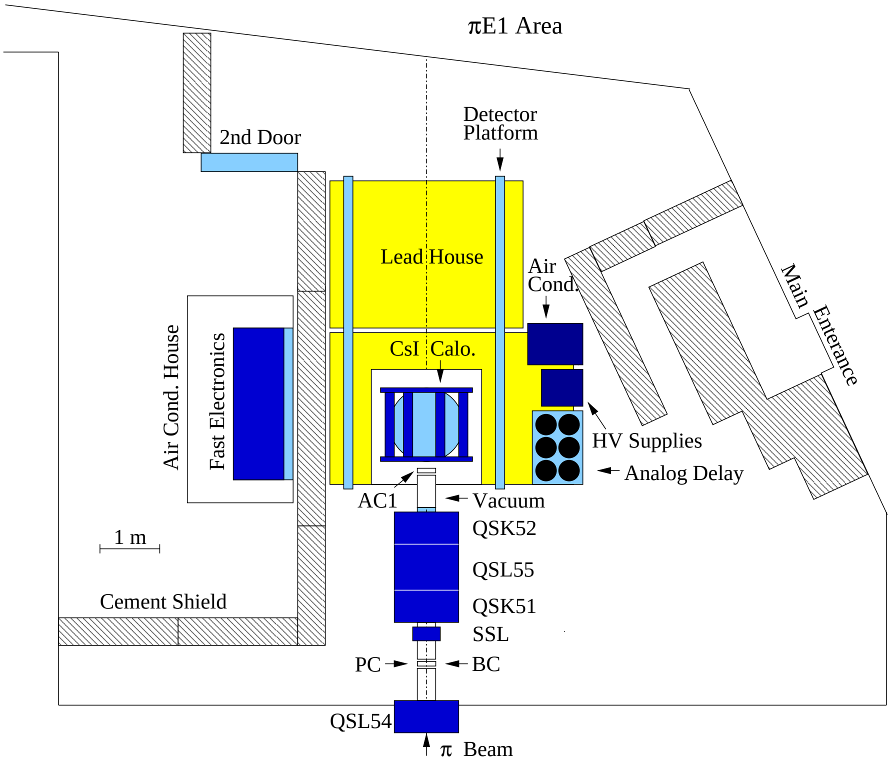

Figure 3.4: Layout of πE1 area.

registered in a 3 mm thick plastic scintillator (BC) placed immediately upstream of the collimator. QSK52, QSL55 and QSK51 are focusing magnets. The beam pions are slowed in a 40 mm long active plastic degrader (AD) and stopped in an active plastic target (AT) positioned at the center of the detector system. The TURTLE calculation yields a FWHM momentum spread of 1.2 MeV/c/113.4 MeV/c$\simeq$1.1 % [24].

We used the OPTIMA [23] control program to adjust the currents in the dipole and quadrupole beam line magnets that steer and focus the π^+ beam into the target. The goal was to achieve the smallest, most symmetric beam spot consistent with the high π^+ beam intensity. The OPTIMA program allows a user to maximize an

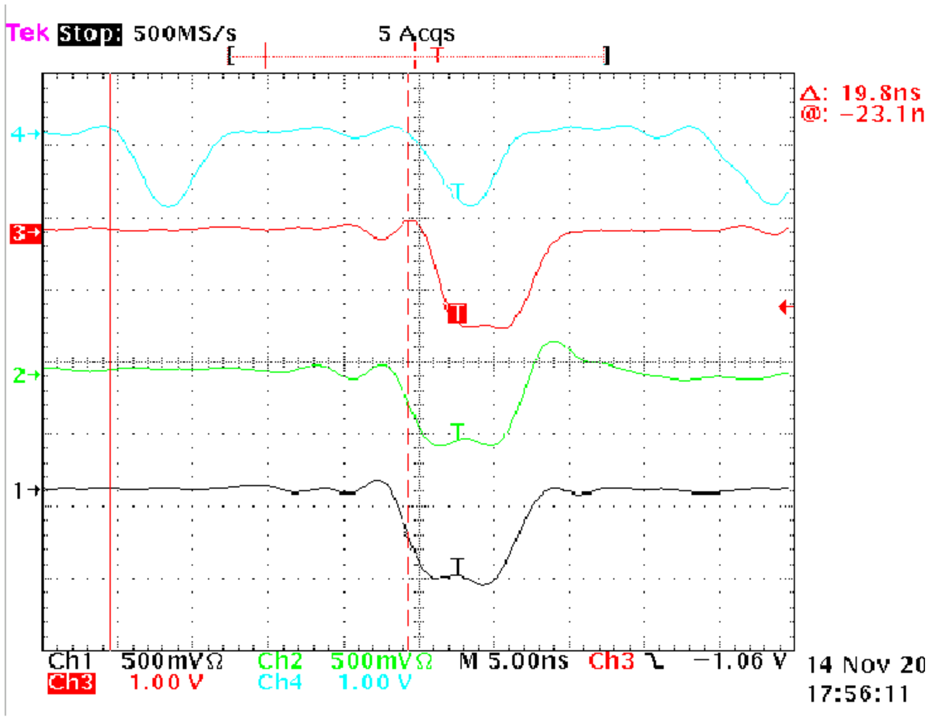

Figure 3.5: Relative timing of signals from the beam counter (BC, top), the target (AT, 2nd from top), the degrader (AD, 3rd from top) and the accelerator (rf, bottom), which defines the π^+-stop signal.

arbitrary experimental rate normalized to the primary cyclotron current by iteratively changing the settings of the magnetic elements. We chose to maximize the rate of four-fold coincidences between the forward beam counter (BC), the degrader counter (AD), the active target (AT) and the accelerator rf signal. These four signals are combined in a coincidence unit in such a way that their overlap signals correspond to a π^+particle stopping in the active target. Fig. 3.5 is a snapshot of the relative timing of the signals forming a π^+-stop trigger signal.

3.2 PIBETA detector

The PIBETA detector (see Fig. 3.6) consists of several components. The major part is a 240-CsI calorimeter covering $\sim 3\pi$ solid angle. Inside the calorimeter, there is a charged particle hodoscope consisting of 20 plastic staves (PV) and two cylindrical Multi-Wire Proportional Chambers (MWPC). The active target (AT) made of plastic scintillator is at the center of the detector. An active degrader (AD) also made of plastic scintillator is located right in front of the target. Two sets of active collimator (AC) rings, each with four segments, are in front of the degrader. The detector system also has a beam counter (BC) located $\sim 3.8\,\mathrm{m}$ in front of the target. The entire detector (except BC) is enclosed in a 300 mm thick lead house, which is covered by active cosmic muon veto consisting of five extensive scintillator planes on four sides and the top.

3.2.1 Modular pure CsI calorimeter

The heart of the PIBETA detector is the shower calorimeter. Its active volume is made of pure Cesium Iodide [25, 26, 27]. The optical and nuclear properties of pure CsI are summarized in Appendix E. The calorimeter (see Fig. 3.7 and Fig. 3.8) consists of 240 CsI crystals in nine different module shapes: four irregular hexagonal truncated pyramids (HEX-A,B,C,D), one regular pentagon (PENT), two irregular half-hexagonal truncated pyramids (HEX-D1,D2) and two trapezohedrons (V1,V2).

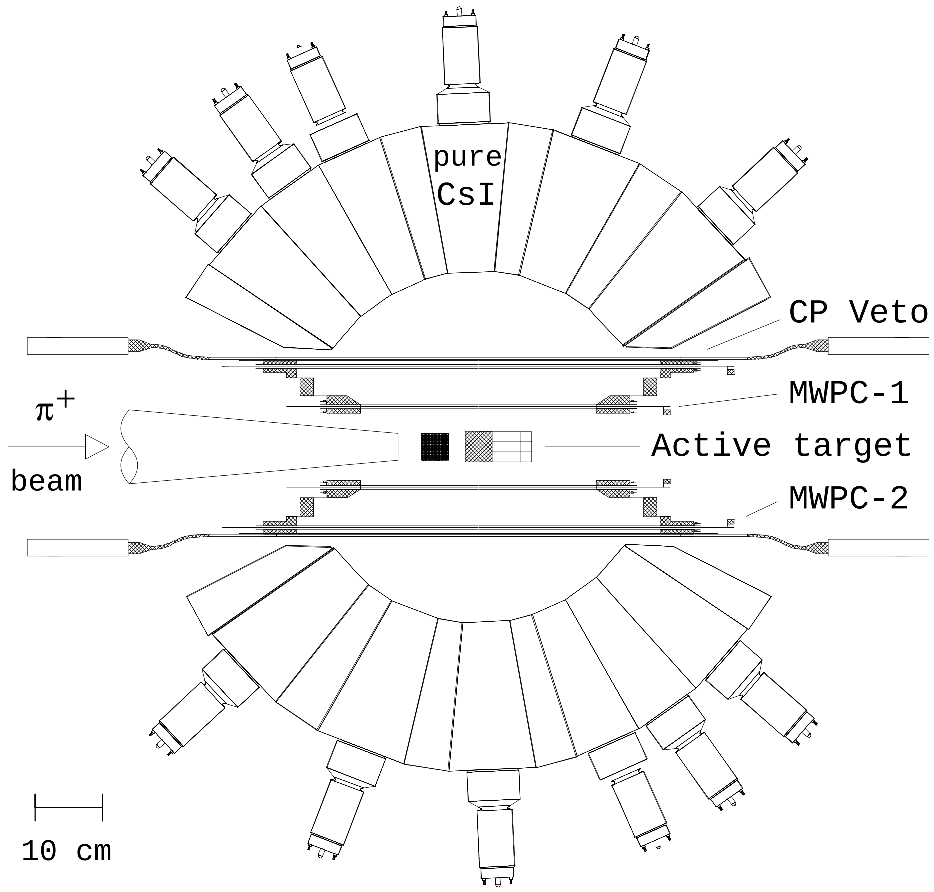

Figure 3.6: Sketch of the cross section of the PIBETA detector system

220 HEX's and PENT's cover a total solid angle of $0.77 \times 4\pi$ sr. 20 V's cover two detector openings for the beam entry and exit and act as electromagnetic shower leakage vetoes. The inscribed radius of the calorimeter is 26 cm and the module axial length is 22 cm, corresponding to 12 CsI radiation lengths ($X_0 = 1.85$ cm) (see appendix E).

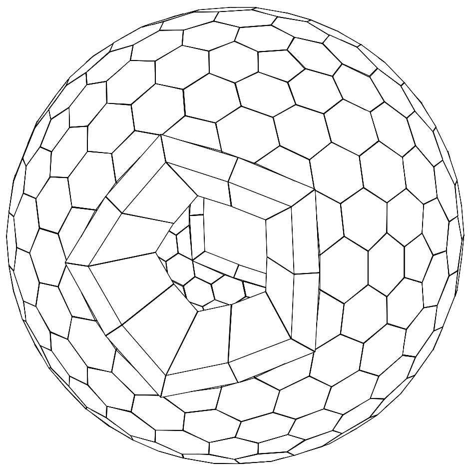

Figure 3.7: CsI crystals in 3D.

3.2.2 Energy calibration of the PIBETA calorimeter

Energy calibration of the PIBETA calorimeter involved two correlated processes: equalizing discriminator thresholds for 220 CsI detector signals that define the calorimeter trigger (see next section) and calibrating signal gains of 240 CsI detectors at the ADC branch by adjusting software gains. The threshold adjustment is achieved by varying the high voltage applied to the PMT so that the positron peak from Michel decay and $\pi 2e$ decay has a ratio of 3 to 1. Since voltage change also affects the gain, the software gain is modified accordingly to offset this effect. If the voltage changes from HV_1 to HV_2 in our 10-stage PMT, and g_1 and g_2 are software gains before and after the voltage adjustment, then

$$g_2 = g_1 \left(\frac{HV_1}{HV_2} \right)^{10} . \tag{3.1}$$

This procedure matches the threshold at the trigger branch so that all crystals behave the same way in generating triggers. This procedure was applied regularly

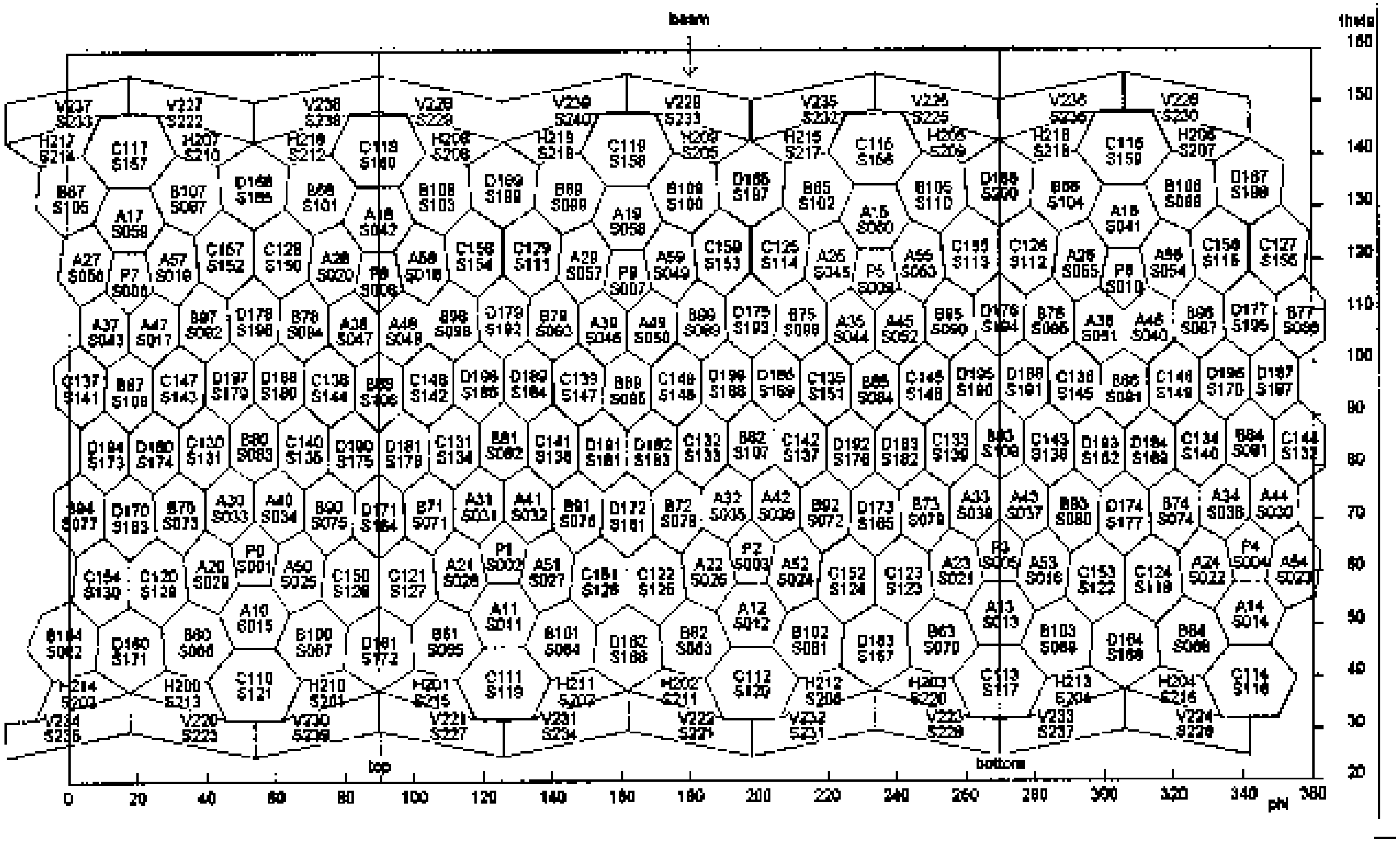

Figure 3.8: Mercator projection of CsI's. In trigger generating scheme, these crystals were grouped into clusters and superclusters (see section 3.3). For example, cluster 0 contains crystal 60, 200, 160, 120, 20, 10, 110, 0, 100. Supercluster 0 includes cluster 0, 10, 20, 30, 40, 50.

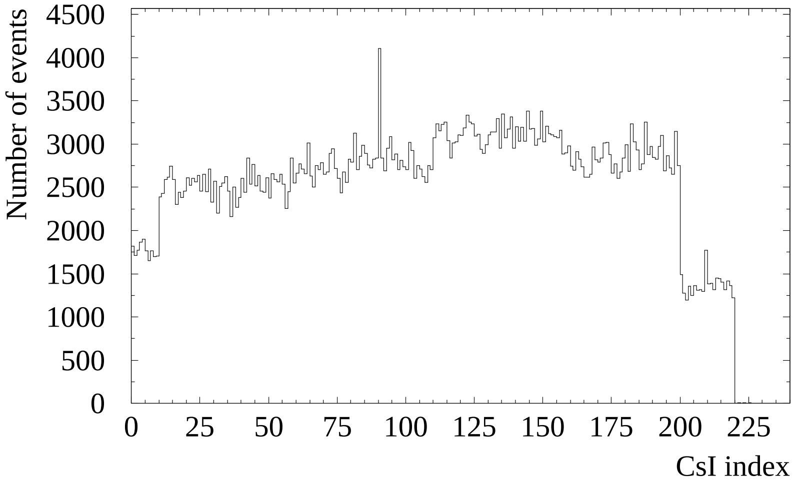

Figure 3.9: Snapshot of online threshold adjustment. A Michel event was filled into the crystal which registered the maximum energy. Ten pentagons (0—9), twenty half hexagons (200—219) and the rest hexagons are shown clearly. The pike in the middle indicates a crystal with higher Voltage that needs to be adjusted lower.

during the experiment. Fig. 3.9 illustrates the effects after this procedure. After the thresholds of all crystals were balanced, the lineshape in Fig. 3.9 reflects the solid angle (or the shape) each crystal extends.

A software gain adjustment adjusts software gains in each channel so that the 69.8 MeV positrons from $\pi^+ \to e^+\nu$ decay all match. A good gain match ensures good energy resolution.

3.2.3 Clump definition, angular resolution and timing response of calorimeter

Each incident particle causes an electromagnetic shower in the calorimeter. To reconstruct the energy of the particle, the energies deposited in all these crystals should be summed up. However, summing up over too many crystals increases the effects of noise. After careful study of shower structure in a MC simulation, we define a 'clump' as our basic calorimeter unit. A clump is defined as a crystal and its nearest neighbors. The energy resolution thus obtained has a FWHM of $\Delta E/E = 12.8 \pm 0.1\%$ at E equal to $\sim 62.5\,MeV$ which corresponds to the $\pi 2e$ positron energy deposited in the calorimeter. The positron peak position is determined by considering energy losses in the active target, plastic veto scintillator, and the insensitive layers in front of the CsI crystals, positron annihilation losses, photoelectron statistics of individual CsI modules, and axial and transverse coefficients parameterizing the nonuniformities of CsI light collection.

Angular Resolution of the CsI Calorimeter

To identify a $\pi^+ \to \pi^0 e^+ \nu$ decay event, we use the two back-to-back photons from the subsequent $\pi^0 \to \gamma\gamma$ decay as a signature. Therefore, reconstructing the right impact point of these two γ's is essential. The angular resolution then depends on the algorithm used in the reconstruction method.

Algorithms Used in Analyzer

Considering the granularity of the CsI crystals, there are three algorithms to be considered to reconstruct the impact point initiating an electromagnetic shower on the surface of the CsI crystal detector sphere. Each uses a weighted mean:

$$X_c = \frac{\sum_i^N w_i(E_i)x_i}{\sum_i^N w_i(E_i)}, \tag{3.2}$$

in which x can be x, y, z, ϕ, θ — the coordinates describing the impact point. E_i is the energy deposited in the ith CsI crystal. N is the number of crystals involved. The sum is carried out over the group of crystals consisting of the one that registers the largest energy and its nearest neighbors. This group is defined as a clump. The weight, $w_i(E_i)$, is a function of the energy in each crystal involved.

Motivated by the work of others [8], we considered three weighting functions

$$w_i^{(1)}(E_i) = E_i, \tag{3.3}$$

$$w_i^{(2)}(E_i) = E_i^r, \tag{3.4}$$

$$w_i^{(3)}(E_i) = \max(0, a_0) + \ln(E_i) - \ln(E_{tot}), \tag{3.5}$$

where r and a_0 are constants and E_{tot} is the total energy in the N crystals in a clump. We refer to $w_i^{(1)}$, $w_i^{(2)}$ and $w_i^{(2)}$ as linear, power, and logarithmic weighting, respectively.

Monte Carlo Studies

By running GEANT [34] simulations, we picked the best weighting algorithm as well as the optimal parameters. From previous work [36], the linear algorithm is the worst of all and the best power weighting parameter is $r = 0.7$. This work focuses on determining the best parameters for logarithmic weighting which is motivated by the exponential fall-off of the transverse energy profile.

In the GEANT simulation, 70 MeV photons were generated in the center of the detector and detected in the calorimeter. By comparing the reconstructed impact point with the real one, the best parameters can be found. Since the detector is spherical, spherical coordinates are used and the best figure of merit is angular resolution. For each identified track, the angular difference between the reconstructed track and the actual track is calculated and filled into histogram with a weight equal to the inverse of the corresponding solid angle (excluding constants, like radius of the sphere). Namely,

$$weight = 1/(\tan^2(\theta_2) - \tan^2(\theta_1)), \tag{3.6}$$

in which θ_1 and θ_2 are the lower edge and upper edge of the bin that θ — the angular difference between the reconstructed track and the actual track — falls in.

A typical histogram is shown in Figure 3.10. The best parameters should make the plot have the minimal rms from 0.

The rms deviation from $\theta = 0°$ with respect to the variation of a_0 is presented

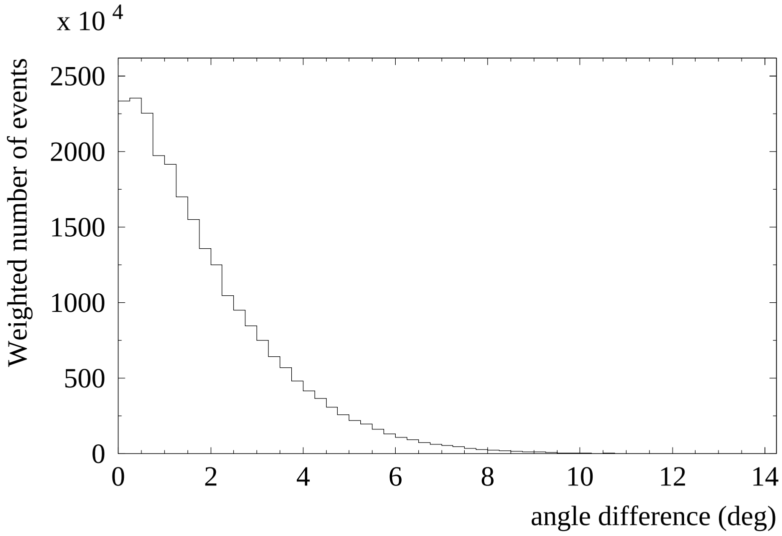

Figure 3.10: Monte Carlo study of the angular resolution: Angular difference between the reconstructed impact point and the actual point.

in Figure 3.11. The best a_0 is 5.4. For comparison, the rms deviation of the power weighting method with the optimized r ($r = 0.7$) is also plotted with an asterisk marker. The logarithmic weighting method is clearly superior and was, therefore, used in our data analysis.

Timing response of PIBETA calorimeter

The calorimeter time resolution depends on the intrinsic time resolution of the individual CsI modules, the spread in the arrival of analog PMT signals at the trigger point where the analog CsI summing is done, and the uncertainties of the software time offsets. Before assembling the calorimeter we measured the intrinsic time res-

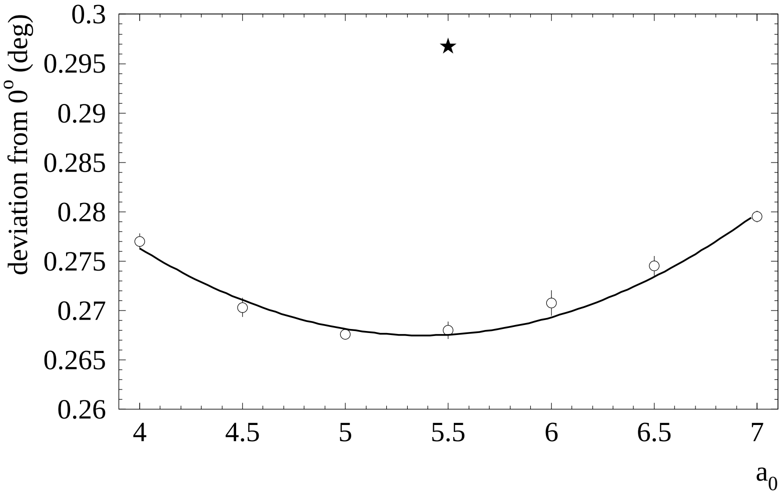

Figure 3.11: Variation of rms deviation from $\theta = 0^\circ$ as a function of parameter a_0 of logarithmic weighting for Monte Carlo data. The asterisk marker is the rms deviation when using power weighting as a comparison.

olutions of all component CsI modules using cosmic muons as a probe. CsI times are determined relative to a small plastic scintillator counter. The average CsI detector rms TDC resolution specified in such a way is 0.68 ns. The details of these measurements are provided in Ref. [28].

CsI timing in trigger branch

The cable connecting each crystal and the trigger-generating unit was checked periodically to minimize the timing spread of triggers. The timing spread was checked in timing calibration runs with the prompt trigger (signaling a hadronic interaction). The idea is to find the time difference between a single reference detector, in our case the active degrader, and each CsI counter. This type of timing histogram, associated with a given CsI detector, is incremented only if a charged particle track is identified as a fast proton ($E_p \geq 60\,\mathrm{MeV}$) in the plastic veto hodoscope and 80% of the shower energy is contained in that module. The total energy contained by the calorimeter is used to calculate the time-of-flight correction, a term that is as large as 1.0 ns for 100 MeV protons. We used the proton events because ~1% uncertainty in statistics in the TDC spectra is acquired within one hour of data taking. The peaks of the timing histograms are fitted at the end of the run and the peak positions are ordered relative to the slowest CsI detector. The resulting information is used to add trigger cable delays, available in 0.5 ns increments, to the faster CsI lines. Three iterations of this procedure resulted in a 0.86 ns relative trigger rms timing spread (Fig. 3.12)

TDC calibration: zero offsets and slewing

TDC calibration is accomplished via two independent corrections, both applied in software. The primary TDC offset correction compensates for the different cable delays of the digitizing branch. The zero time is defined as the center of gravity of the self timing peak for each detector channel. These offsets will be evaluated at the end of the runs and can be applied to the software timing offsets which will align self-timing peaks of all channels at zero. Timing of beam counters, active degrader and target is also adjusted same way. The decays suited for this purpose are prompt events (SCX).

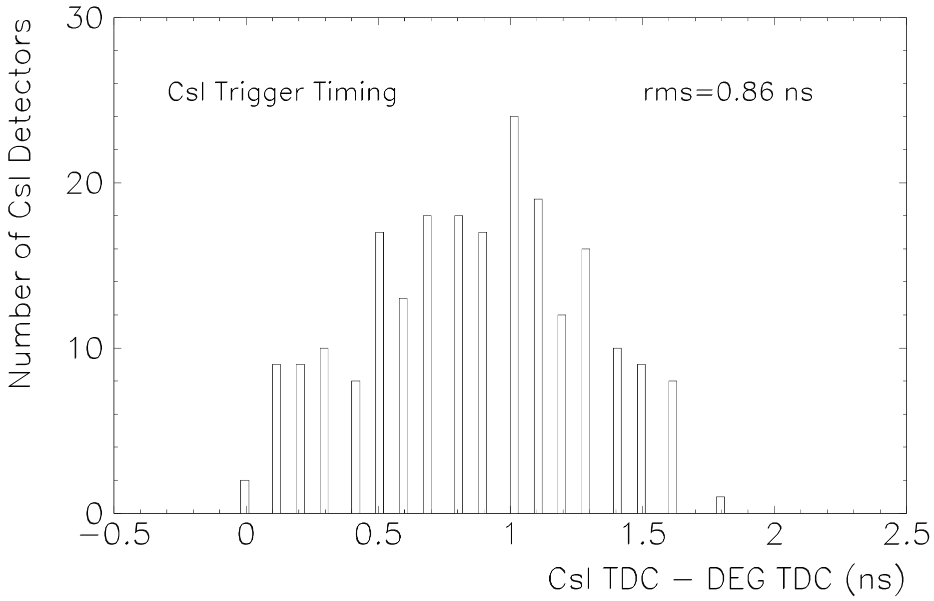

Figure 3.12: CsI crystal timing spread in trigger branch. The data were taken during runs dedicated to the timing adjustment in which hadronic events were specifically selected.

The secondary TDC correction linearizes the slewing of TDC time caused by the differing amplitudes of ADC signals. A smaller amplitude signal takes more time to rise to the fixed discriminator threshold than a larger signal. The result is an artificial energy dependence of TDC values with lower energy signals registering later times. The secondary TDC correction is implemented in offline analysis by subtracting an energy-dependent term from each TDC reading. This correction term has the form

$$CTDC = TDC_0 + a \cdot (ADC - b)^c, \tag{3.7}$$

where TDC_0, a, b, and c are free parameters of the fit. ADC is the calibrated ADC value proportional to the deposited energy. The correction term was obtained by fitting the TDC *vs.* ADC plot for each channel. Fig. 3.13 shows the energy dependence of one representative CsI TDC and the reduction in the time slewing after applying the correction.

3.2.4 Multi-wire proportional chamber

The MWPC was designed and manufactured by collaborators from the Joint Institute for Nuclear Research (JINR), Dubna, Russia. Two concentric cylindrical chambers were installed, each having one anode wire plane along the z direction, and two cathode strip planes in stereoscopic geometry. Specifically designed for our experiment, they have features of:

- low mass, in order to minimize the γ's converting into e^+e^- pairs;
- high intrinsic efficiency, better than 99.9%;
- high rate capability, up to 10^7 minimum-ionizing particles (MIP) per second;
- stable operation and good radiation hardness.

Ref. [29, 30] provides a detailed description of the PIBETA wire chambers.

3.2.5 Resolution of the Multiwire Proportional Chambers

To fully simulate the detector, the resolution of the MWPC needs to be determined. Cosmic events are used to extract alignment parameters as well as resolutions. For each cosmic event, exactly two hits in each chamber were required. From one pair of

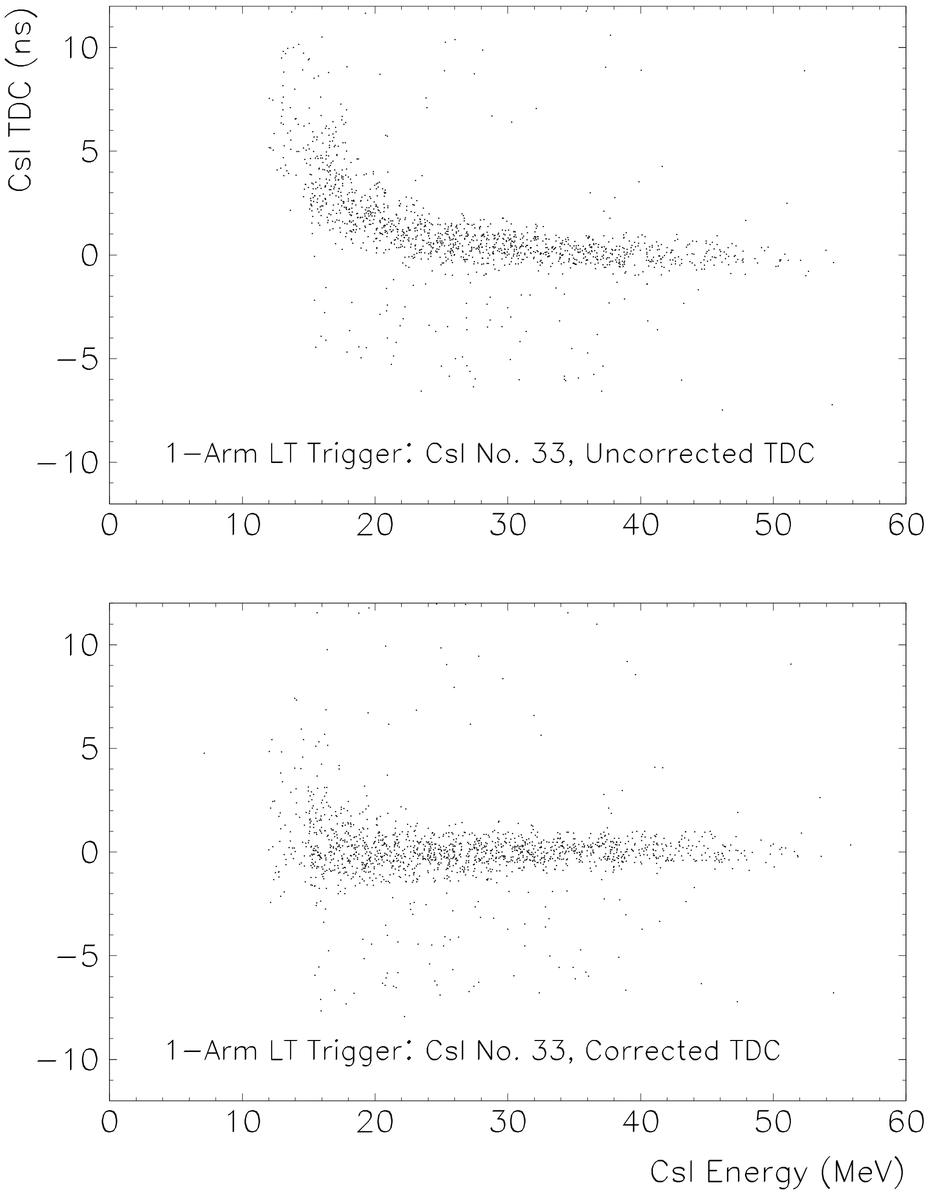

Figure 3.13: TDC's dependence on ADC (time slewing, top panel) and corrected TDC (bottom panel). The plot shown here is from CsI 33, others similar features. Data are collected in ten runs.

points in one chamber, a straight line is obtained and the intersection points of this line with the other chamber are calculated. The difference between the registered points and the calculated points is stored into histograms and viewed as chamber resolution in each direction in Cartesian coordinates. Since the chambers are cylindrical, the resolution in polar angle is also investigated.

In processing chamber data, there are several parameters that can be adjusted to accommodate the misalignment between two chambers and thus get the best resolution.

Corrections of polar angle

After chamber data were processed, two parameters, $\phi_{\text{corr}}^{\text{inner}}$ and $\phi_{\text{corr}}^{\text{outer}}$, were added to the polar angle (ϕ) obtained, to chamber one (inner chamber) and chamber two (outer chamber) respectively. Since ϕ was calculated from $-180°$ to $180°$, this parameter can move ϕ's below zero and above zero in opposite direction. A mis-determined ϕ_{corr} gives double peaks in the resolution histogram, as illustrated in Figure 3.14.

The more tell-tale variable is ϕ resolution. For the outer chamber ϕ resolution, the difference between ϕ_{exp} registered in the outer chamber and ϕ_{the} calculated from the track determined by the inner chamber is calculated and plotted against ϕ_{the} as in Figure 3.15. By adjusting the parameter $\phi_{\text{corr}}^{\text{outer}}$, the group of points which are less than $180°$ in ϕ_{the} and the group of points which are greater than $180°$ move in the opposite direction and, with an optimal $\phi_{\text{corr}}^{\text{outer}}$, center at 0, which yields the best resolution as shown in Figure 3.16. The parameter for the inner chamber, $\phi_{\rm corr}^{\rm inner}$, is determined to be equal to 0.0°. The resolution for the inner chamber is shown in Figure 3.17.

The resolution plots are fitted with a sum of Gaussians due to the nature of these plots. In simulation, the sum of Gaussians obtained above is used to smear the chamber data.

Alignment of Chambers in z Direction

From resolution plots, Figure 3.16 and figure 3.17, one can see the z plots are offset, which means the z coordinates are not aligned for these two chambers. An additional parameter is introduced for each chamber, $\mathrm{z}_{1\mathrm{off}}$ and $\mathrm{z}_{2\mathrm{off}}$, to get the two chambers aligned in z as shown in figure 3.18.

Alignment of Chamber Wires and Cathode Strips

ϕ data are obtained both from wires and cathode strips, and the data are discarded if they are not consistent. One parameter is introduced for each chamber to align the chamber wires and cathode strips. Results are shown in Figure 3.19.

3.2.6 Target Position

In the coordinate system defined by two wire chambers described above, the position of the 9-piece target was also determined using cosmic events.

Since the inner chamber and the outer chamber have already been aligned as described above, the position of the target was determined relative to the inner chamber. For each cosmic muon event which left two hits in inner chamber, we calculate the path length of this track through the target, which was centered at

$$
\begin{aligned}
x &= \mathrm{x_{offset}} \\
y &= \mathrm{y_{offset}} \\
z &= \mathrm{z_{offset}}
\end{aligned}
$$

Combining calculated path-length in the target and signals registered in the target, there are four possibilities for each cosmic event:

- no intersection, no signal in the target.
- intersection found, positive path-length, no signal above the threshold in the target.
- no intersection, signal above the threshold registered in the target. These events were counted in $\mathrm{N_{miss}}$.
- pathlength is found, signal above the threshold registered in the target. These events were counted in $\mathrm{N_{hit}}$.

By varying target offsets, the dependence of ratio $\mathrm{R = N_{hit}/(N_{hit} + N_{miss})}$ on target position offsets was obtained. The best offsets of the target were determined when R had its maximum value.

Results

Three 2-dimensional histograms were obtained. The ratio R was plotted against x and y (Fig. 3.20), against x and z (Fig. 3.21) and against y and z (Fig. 3.22).

From the plot in Figure 3.21, one can get $x_{\text{offset}} = -0.51\,\text{mm}$ and $z_{\text{offset}} = 6.3\,\text{mm}$. From the plot in Figure 3.20, one can get $x_{\text{offset}} = -0.9\,\text{mm}$ and $y_{\text{offset}} = -4.3\,\text{mm}$. From the plot in Figure 3.22, one can get $y_{\text{offset}} = -4.0\,\text{mm}$ and $z_{\text{offset}} = 6.3\,\text{mm}$. The center position of the target is then taken as the average of these results.

$$
\begin{aligned}
x &= -0.7 \pm 0.2\,\text{mm}, \\
y &= -4.2 \pm 0.1\,\text{mm}, \\
z &= 6.3 \pm 0.5\,\text{mm}.
\end{aligned}
\tag{3.8}
$$

The maximization of the ratio R is an iterative process with three parameters involved. The best way is to use the MINUIT package [35]. Currently, we accept the average of these offsets. Since our data sample is dominated by the cosmic rays which have small zenithal angles, the offset in the vertical direction was the most difficult to get.

3.2.7 Plastic veto detector

The plastic veto (PV) detectors are located in the interior of the calorimeter surrounding the two concentric wire chambers. The detector consists of 20 independent plastic scintillator staves arranged to form a complete cylinder 598 mm long with a 132 mm inner radius. Each plastic stave is 3.175 mm thick. The PV's cover the entire geometrical solid angle subtended by the CsI calorimeter as seen from the target center. The rise and decay times of the fast scintillator pulses are 0.9 ns and 2.4 ns, respectively. Ref. [31] contains details about the specifications of the plastic scintillator used.

The two readouts from either end of each PV stave were recorded. The energy from each stave was calculated as the geometric mean of these two signals to eliminate the length effect. Suppose the charged particle passing through a plastic veto stave generates initial light intensity L_0 at a distance x from one end, then the two readouts from either end are:

$$\begin{aligned} E_1 &= L_0 \exp\left(\frac{-x}{l}\right), \\ E_2 &= L_0 \exp\left(\frac{-(L-x)}{l}\right), \end{aligned} \tag{3.9}$$

where l is the attenuation length which averages to 396 ± 13 mm [32] for our plastic scintillators, and L is the length of the plastic veto stave. Then the geometric mean of these two readouts is

$$E_{mean} = \sqrt{E_1 E_2} = L_0 \exp\left(\frac{-L}{l}\right), \tag{3.10}$$

which is independent of the impact position where the initial light was generated. The energy calculated in this way for positrons and protons is illustrated in Fig. 3.23. The energy resolution measured for minimum ionizing particles is $\sigma_E/E = 33.2\%$.

3.3 PIBETA trigger generating scheme

Selective, bias-free triggers capable of handling high event rates are an essential requirement of the detector system. Relevant trigger schemes are explained here. A detailed description of all triggers implemented in PIBETA experiment can be found in Ref. [32].

3.3.1 Signals used to generate triggers

CsI HI and CsI Lo

The one-arm calorimeter energy signal is a basic element of the trigger logic. A preliminary simulation study [33] of the calorimeter response to photons from $\pi\beta$ decay at rest and 70 MeV positrons from $\pi 2e$ decays indicated that:

- electromagnetic shower profiles of the mean deposited energies are similar for photons and positrons, in particular for $\theta_c \leq 12^\circ$, with θ_c being the half angle of a conical bin concentric with the direction of an incident particle;

- the average deposited energy and the corresponding energy resolution of the calorimeter both reach saturation within a cone of 12° half-angle;

- a centrally hit CsI module receives on average 90% of the deposited energy; at most three modules contain a significent part of the shower energy; and a group of 9 detectors (a CsI "cluster") constitutes an excellent summed energy trigger as it registers on average $\geq 98\%$ of the incident particle energy.

Therefore, the building blocks of physics triggers are clusters (see Fig 3.8). Excluding the CsI shower vetoes from the scheme we define 60 such clusters [32]. Every CsI cluster has a symmetric partner in the antipodal calorimeter hemisphere. In addition, each CsI module belongs to no more than three clusters. This limitation helps to minimize the degradation of analog pulses due to excessive signal splittings. In trigger design studies that looked at the energy captured by a single cluster as a figure of merit, it was found that this clustering scheme, in conjunction with a 50 MeV discrimination threshold, gives 99.3% and 98.6% triggering efficiency for 70 MeV photons and positrons, respectively.

Six adjacent CsI clusters are grouped into a CsI "supercluster": there are ten such superclusters in the calorimeter each containing 10 individual CsI clusters. A supercluster fires if at least one of its constituent clusters fires. A cluster fires if the summed energy of its modules is greater than the preset discriminator threshold. If at least one supercluster fires due to energy above high (low) threshold ($\sim 50\,\mathrm{MeV}$) ($\sim 5\,\mathrm{MeV}$), then we have a $\mathrm{CsI_{HI}}$ ($\mathrm{CsI_{LO}}$) signal. If at least two superclusters in the opposite sphere fire, then we have $\mathrm{CsI^2_{HI}}$ (if above high threshold) or $\mathrm{CsI^2_{LO}}$ (if above low threshold) signal.

Beam particle signals

The BEAM signal is defined as the three-fold coincidence between the beam counter (BC), the degrader (AD) and the rf signal from the accelerator.

$$\mathrm{BEAM} = \mathrm{BC} \cdot \mathrm{AD} \cdot \mathrm{rf}. \tag{3.11}$$

The PISTOP signal is defined as the four-fold coincidence between BC, AD, (AT and the rf accelerator signal.

$$\mathrm{PISTOP} = \mathrm{BEAM} \cdot \mathrm{AT}. \tag{3.12}$$

Minimum-ionizing positrons in the BC, AD, and AT counters deposit 0.6 MeV, 7.2 MeV and 9.0 MeV energy respectively. The corresponding energy depositions for 114.0 MeV/c pions are 0.7 MeV, 12.7 MeV and 28.0 MeV. By appropriately adjusting the discriminator thresholds and the relative timing (see previous sections) of inputs into the quadruple coincidence 3.12, the PISTOP signal is set up.

Each PISTOP signal initiates a pion gate πG, a 180 ns window, whose delay is adjusted to start ~50 ns ahead of the pion stop time t_0. Several such πG's were generated which were properly prescaled to balance different triggers. We use πG_{ps} to denote such a gate.

3.3.2 Triggers in the PIBETA experiment

The following triggers are generated with the above signals.

PIBETA HI trigger:

$$\mathrm{PB_{HI}} = \pi\mathrm{G} \cdot \mathrm{CsI}^2_{\mathrm{HI}} \cdot \overline{\mathrm{BEAM}}. \tag{3.13}$$

PIBETA LOW trigger:

$$\mathrm{PB_{LO}} = \pi\mathrm{G_{ps}} \cdot \mathrm{CsI}^2_{\mathrm{LO}} \cdot \overline{\mathrm{BEAM}}. \tag{3.14}$$

PIENU HI trigger:

$$\mathrm{PIENU_{HI}} = \pi\mathrm{G_{ps}} \cdot \mathrm{CsI_{HI}} \cdot \overline{\mathrm{BEAM}}. \tag{3.15}$$

PIENU LOW trigger:

$$\mathrm{PIENU_{LO}} = \pi\mathrm{G_{ps}} \cdot \mathrm{CsI_{LO}} \cdot \overline{\mathrm{BEAM}}. \tag{3.16}$$

PROMPT trigger:

$$\mathrm{PROMPT} = \pi\mathrm{G_{ps}} \cdot \mathrm{CsI_{HI}}. \tag{3.17}$$

COSMIC trigger:

$$\mathrm{COSMIC} = \mathrm{CV_{ps}} \cdot \mathrm{CsI_{HI}} \cdot \overline{\mathrm{BEAM}}. \tag{3.18}$$

where $\mathrm{CV_{ps}}$ is a prescaled cosmic veto scintillator signal.

RANDOM trigger:

a small piece of plastic scintillator is placed outside of and away from the lead house, parallel to the πE1 beamline area floor. By virtue of its position, the counter is shielded from the experimental radiation. Operating with a high discriminator threshold, it counts only cosmic muons and random background events at about 1-2/s, and has a stable counting rate independent of the beam. The signal from this counter defines the RANDOM trigger.

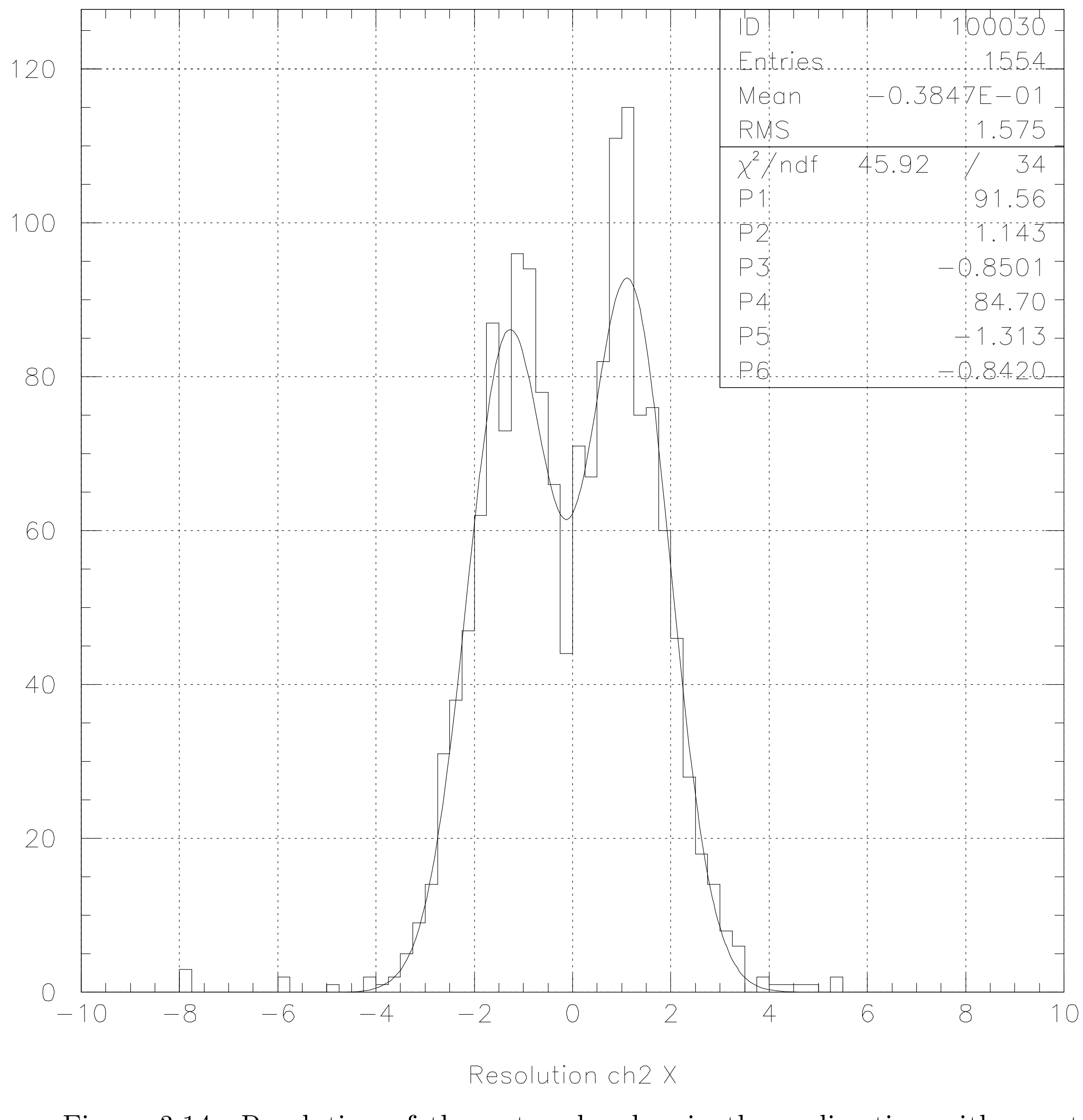

Figure 3.14: Resolution of the outer chamber in the x direction with a not-well-determined $\phi_{\mathrm{corr}}^{\mathrm{outer}}$. In the plot the difference in x between the registered points in the outer chamber and the calculated intersection points of the track and the outer chamber is plotted. The track is determined by the inner chamber.

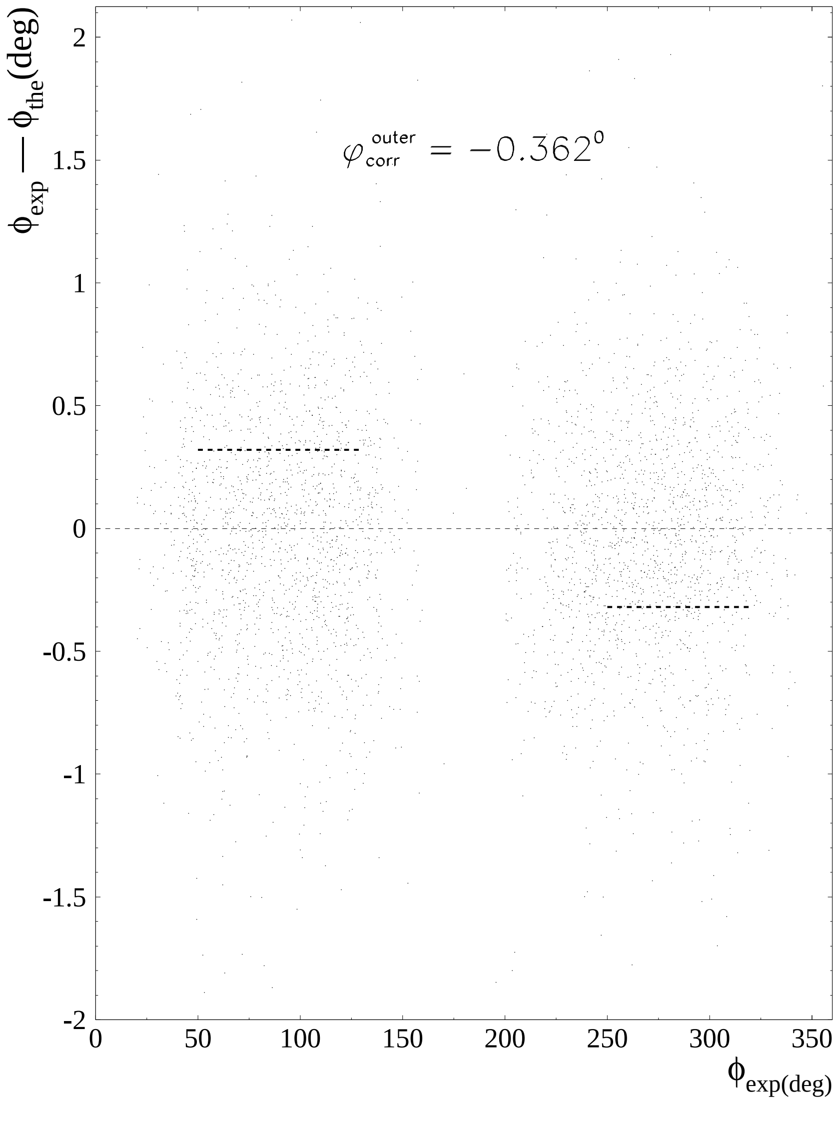

Figure 3.15: $\phi_{\text{exp}} - \phi_{\text{the}}$ *vs.* ϕ_{the} for the outer chamber. The two bold dashed lines indicate the mean values of points when ϕ_{the} is less than 180° and above 180° respectively, before the adjustment of $\phi_{\text{corr}}^{\text{outer}}$.

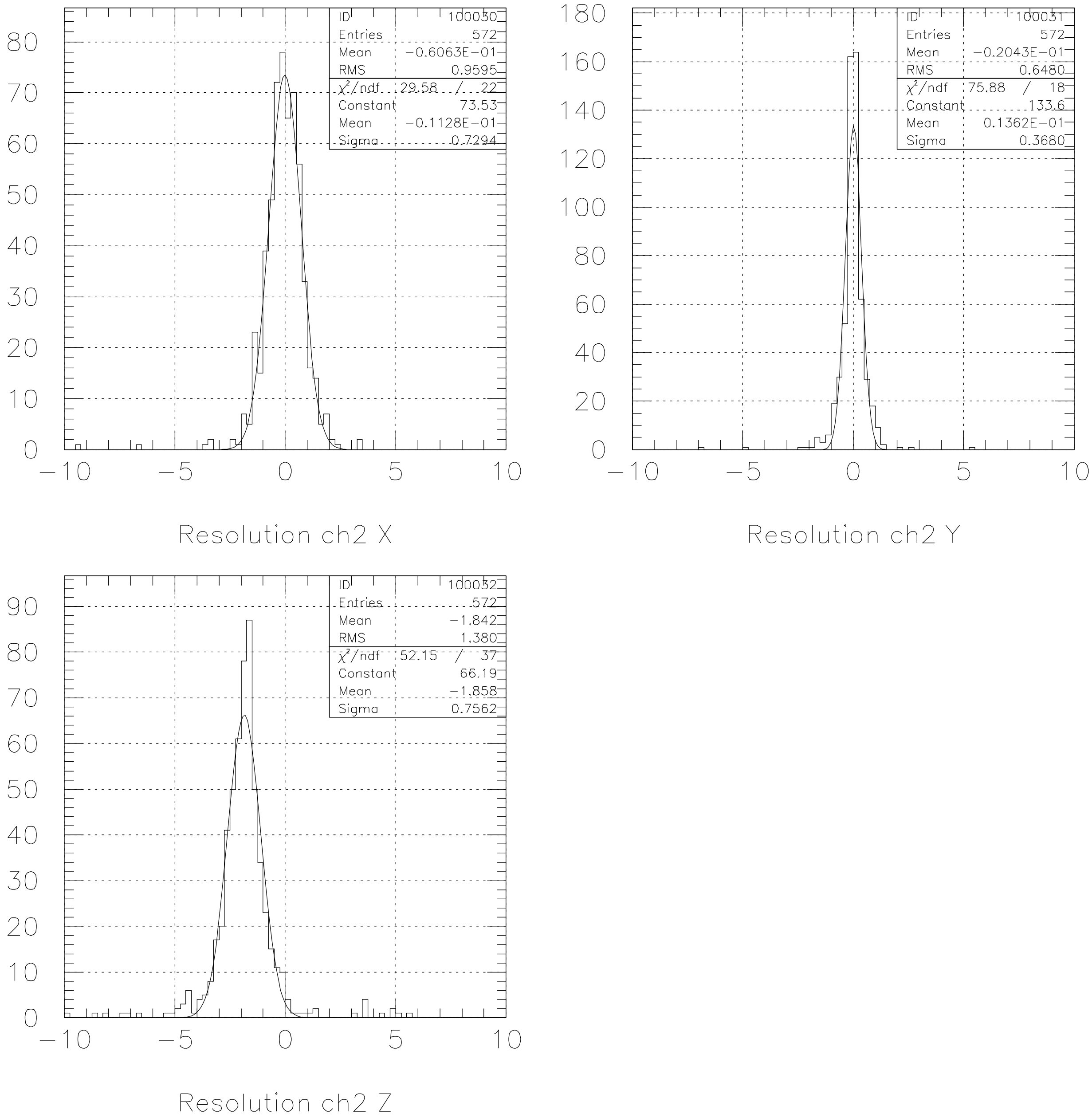

Figure 3.16: Directional resolutions of the outer chamber (in mm).

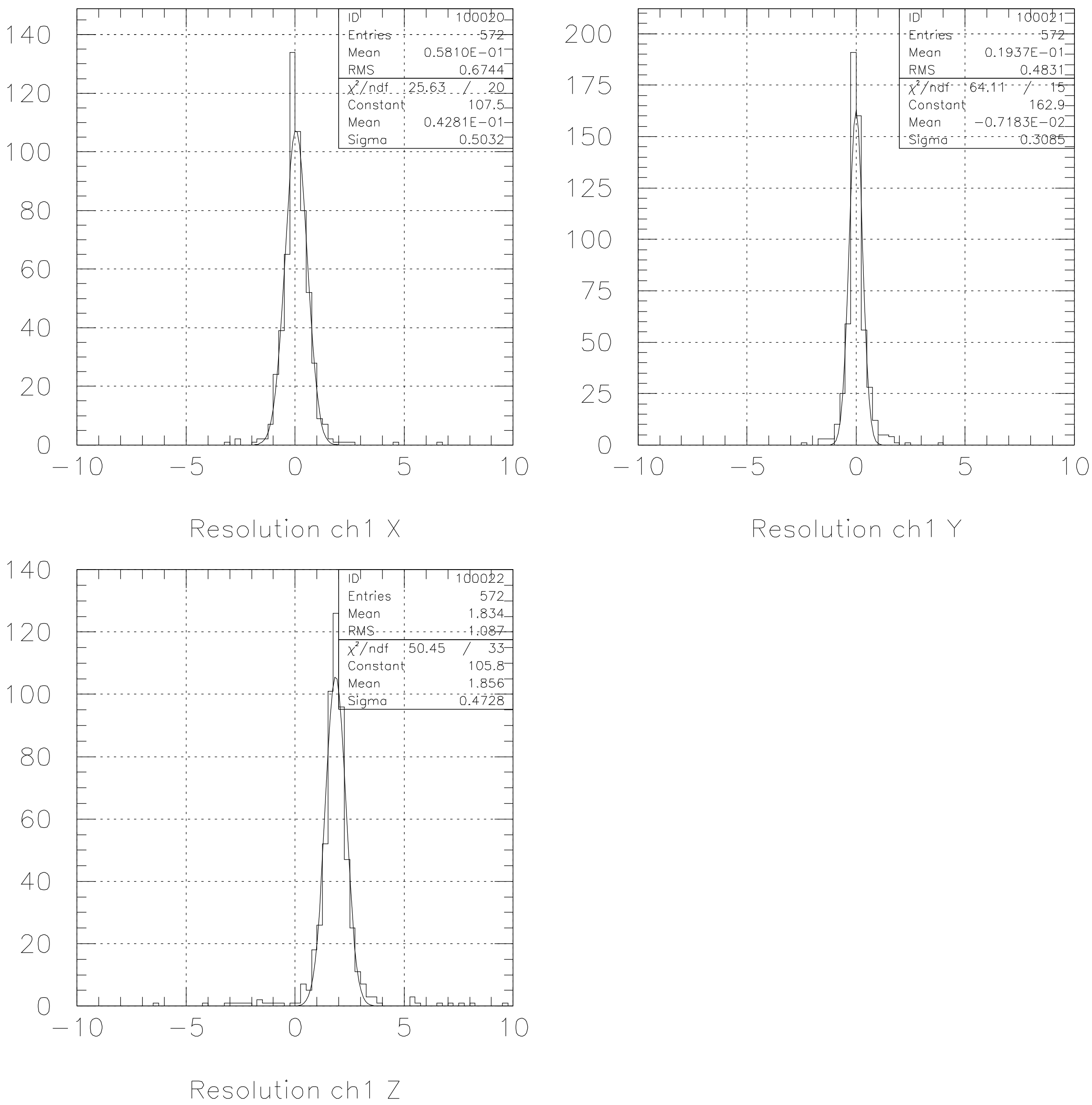

Figure 3.17: Directional resolutions of the inner chamber (in mm).

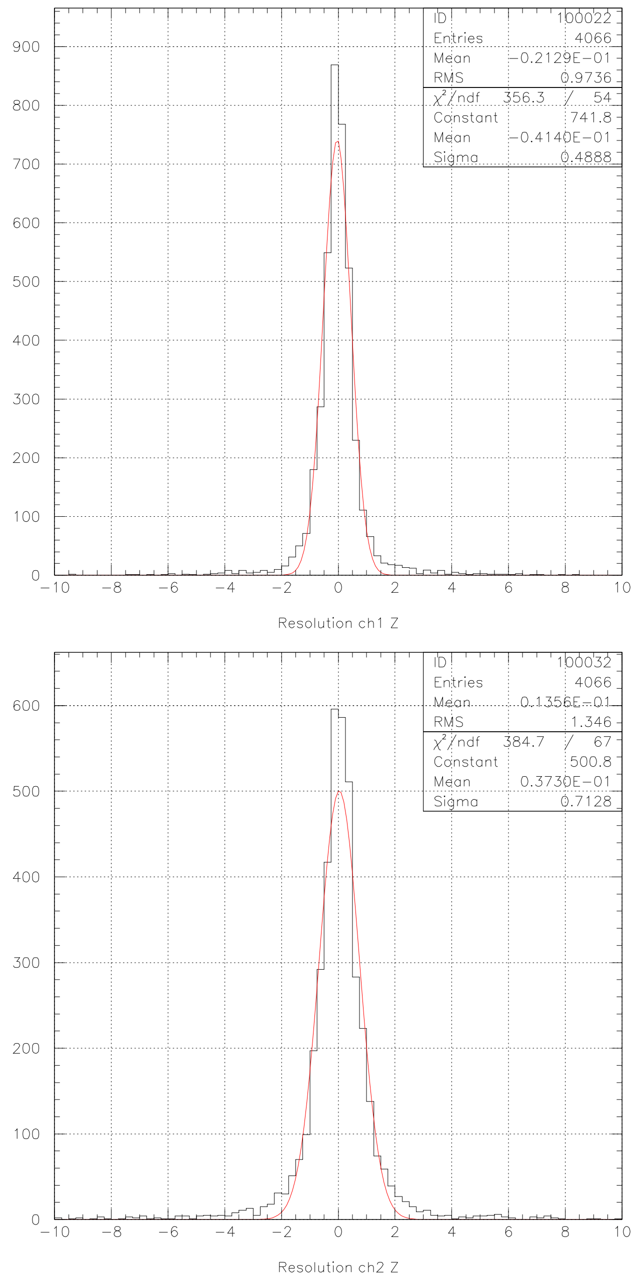

Figure 3.18: Axial resolution of two chambers after adjusting z alignment (in mm). Chamber 1 is inner chamber, chamber 2 is outer chamber.

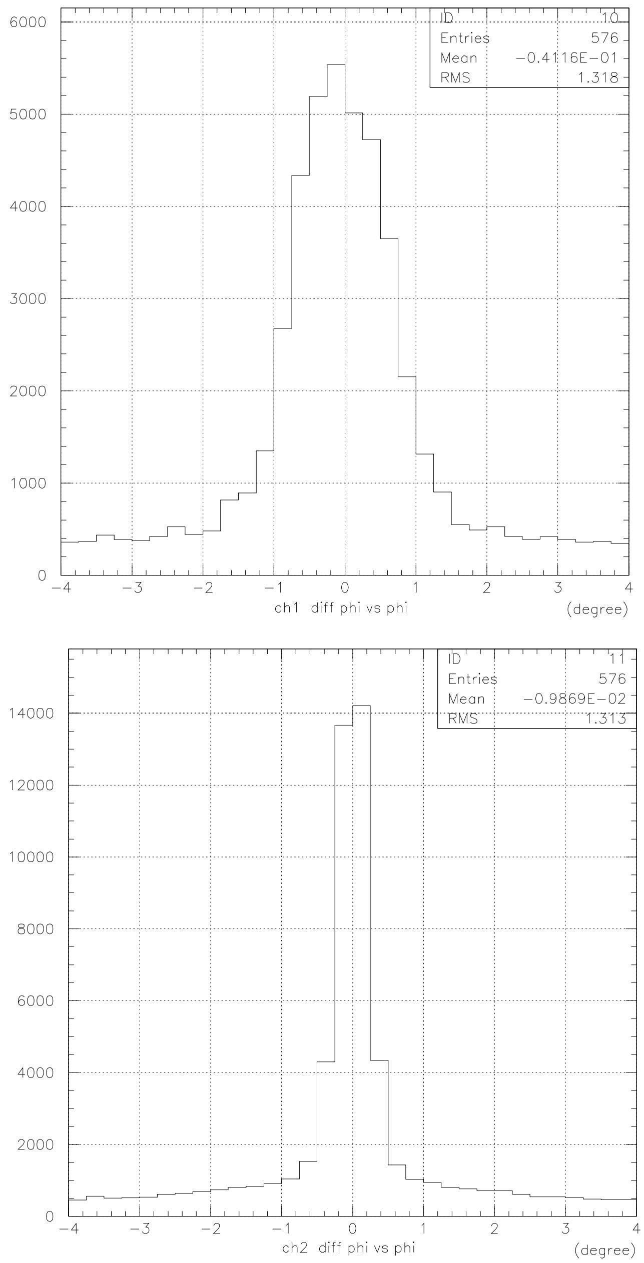

Figure 3.19: Differences between azimuthal angles determined from wires and cathode strips for the inner (chamber 1) and the outer (chamber 2) chambers.

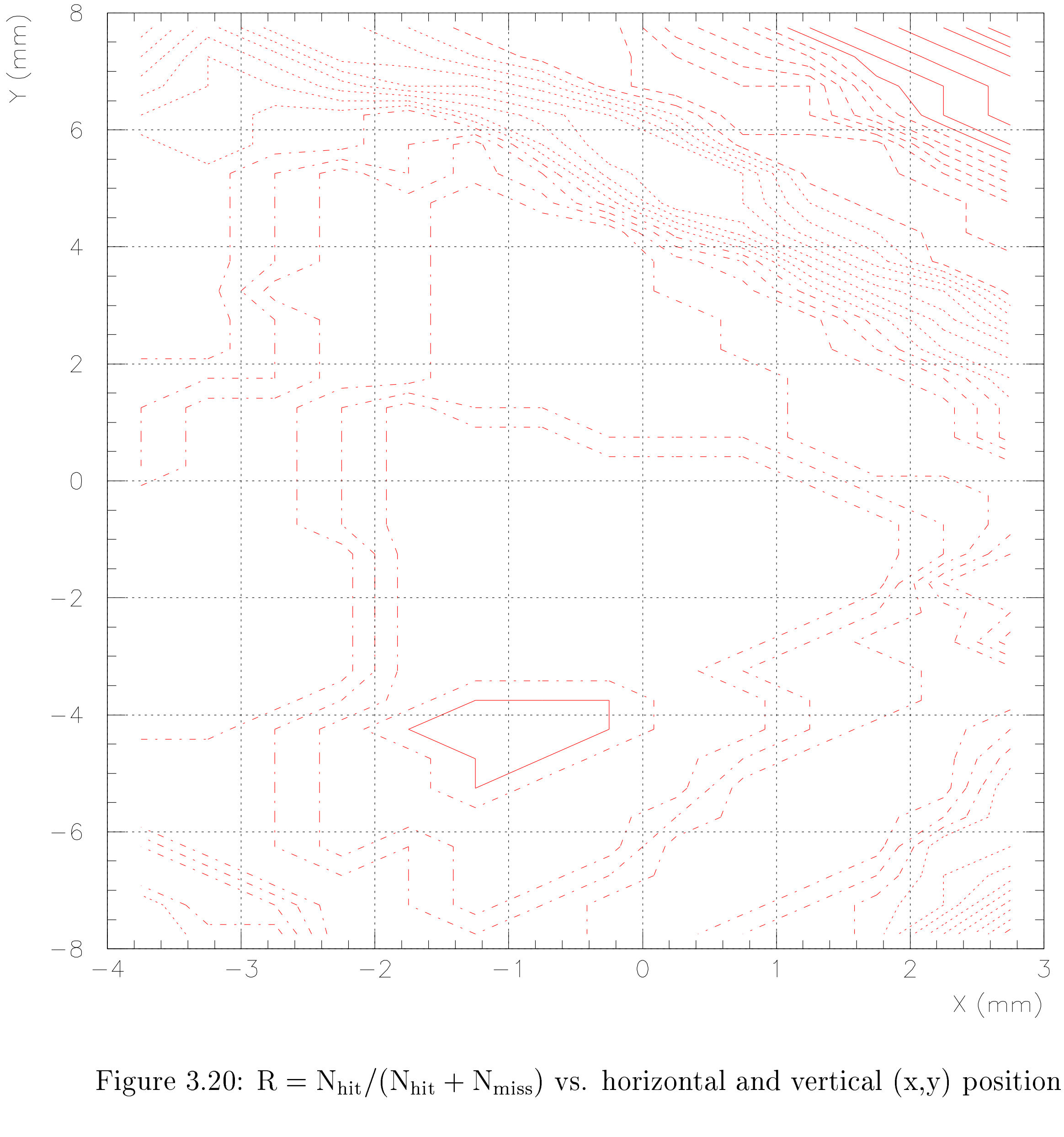

Figure 3.20: $R = N_{hit}/(N_{hit} + N_{miss})$ vs. horizontal and vertical (x,y) position.

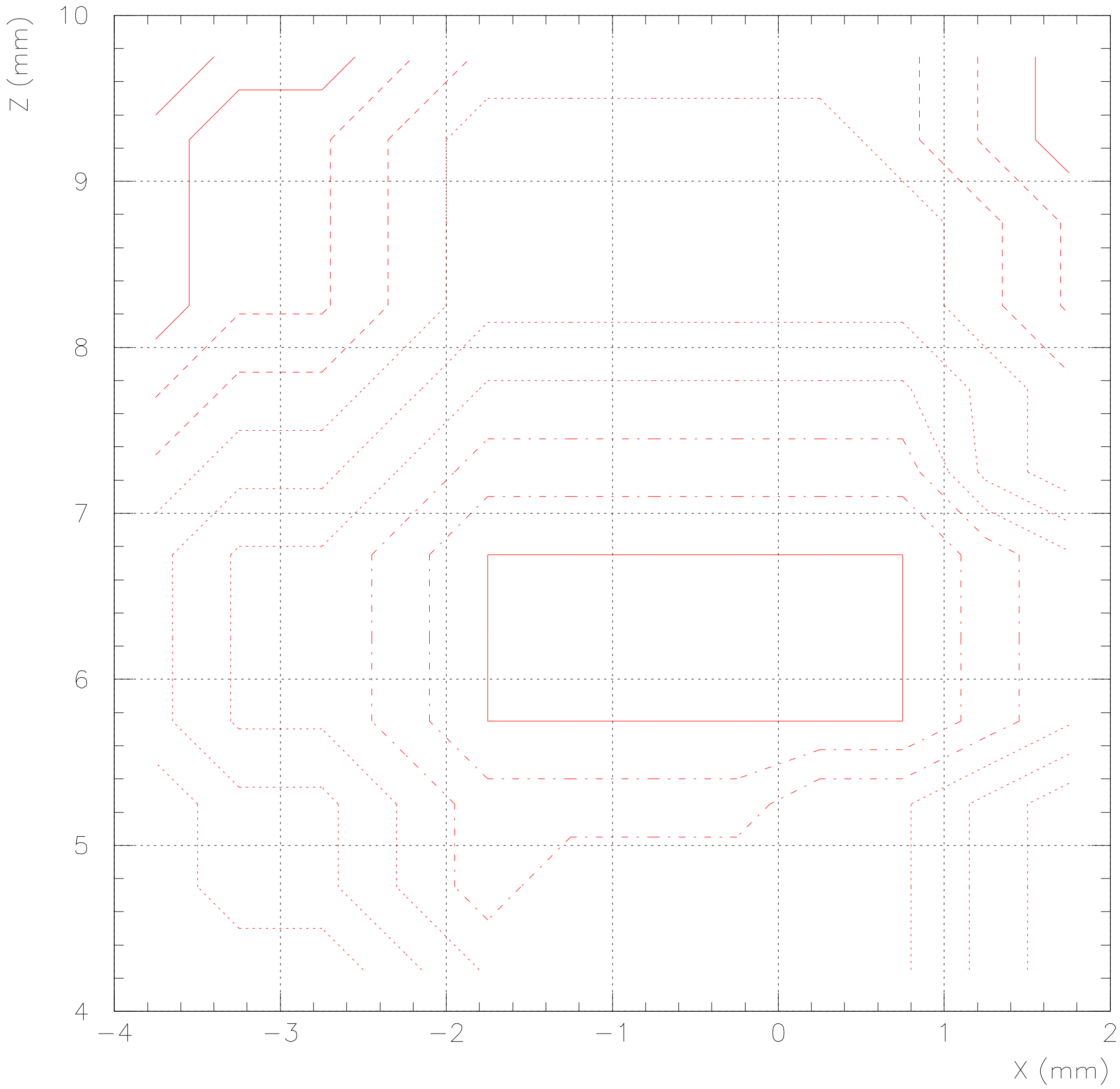

Figure 3.21: $R = N_{hit}/(N_{hit} + N_{miss})$ vs. horizontal and longitudinal (x,z) position.

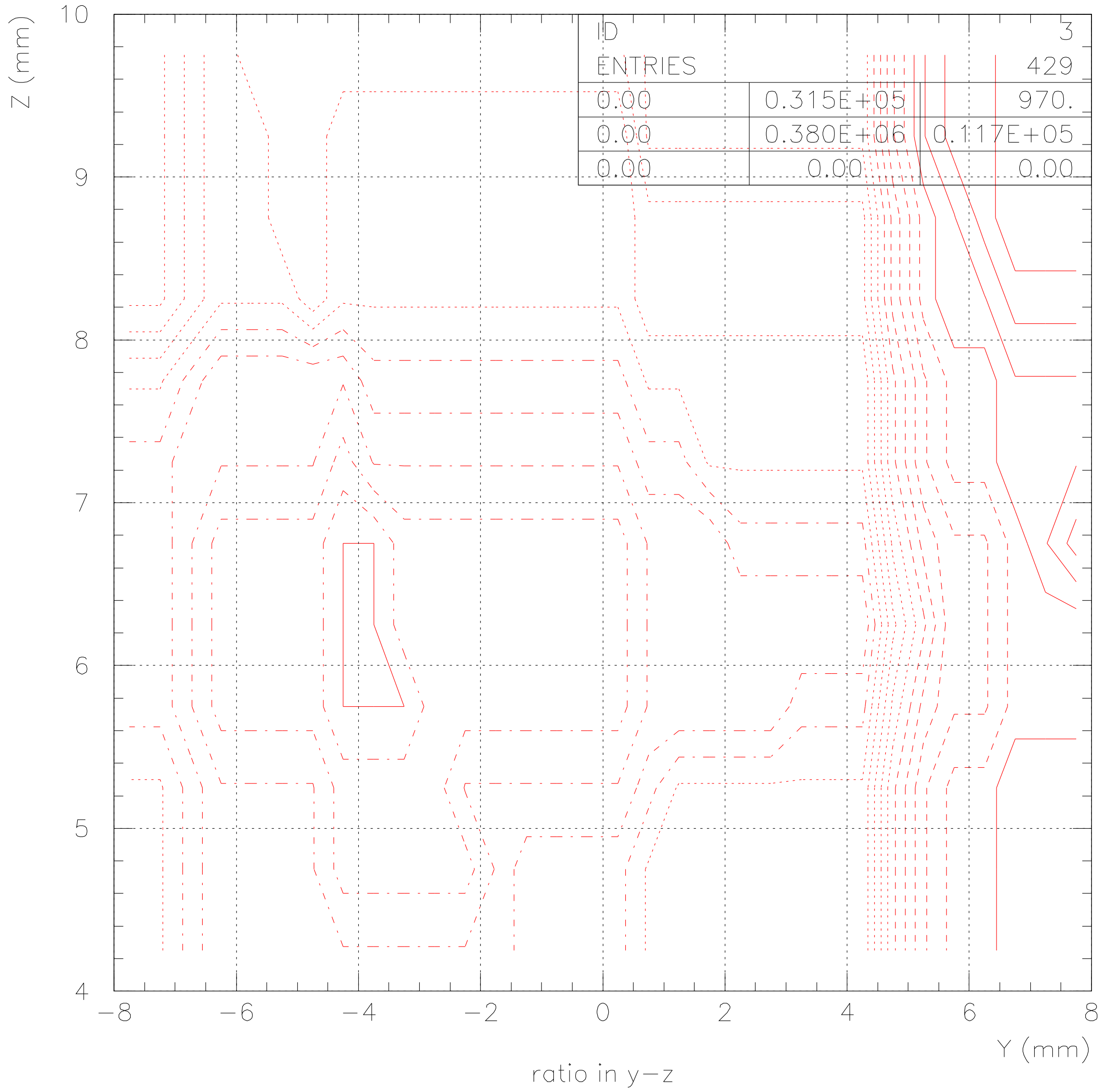

Figure 3.22: $R = N_{hit}/(N_{hit} + N_{miss})$ vs. vertical and longitudinal (y,z) position.

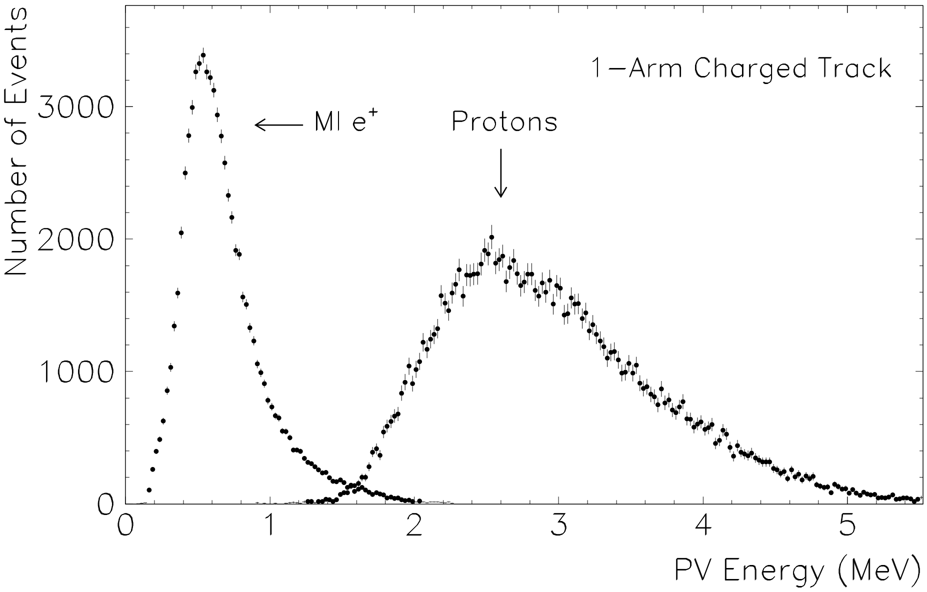

Figure 3.23: Energy response of PV detectors. Positrons and protons were selected separately and the energies deposited in the PV's were filled into histograms for each kind of particles.

Chapter 4

Extracting $\pi\beta$ events from experiment

4.1 Particle Identification

PMT signals from different detectors are combined to determine the energy of the shower in the calorimeter and then a particle ID is assigned to each shower. All information associated with each shower, deposited energy in colorimeter, deposited energy in plastic veto, track direction determined by MWPC (if charged particle), particle ID, are stored in a track data structure. Information from chambers, plastic vetoes and CsI's are used to determine the particle ID. From the nature of the experiment, the charged particles include positrons from $\mu^+ \rightarrow e^+\nu\overline{\nu}$ and $\pi^+ \rightarrow e^+\nu$ decay, protons from π^+ hadronic interaction, muons from cosmics, the neutral particles are γ's from π^0 decay in which π^0 can come from π^+ hadronic interactions or $\pi^+ \to \pi^0 e^+ \nu$ decay.

In order to identify charged particles, each MWPC chamber must register a signal and the two hit points should be fairly aligned (within a certain angle). In addition, the energy deposited into plastic vetoes and energy deposited in CsI's along the direction determined by the chambers should match. By studying the energy in PV's and the energy in CsI's, positrons are defined as satisfying the requirements:

$$\begin{aligned} \mathrm{E_{pv}} &< 0.2 \times \exp(-0.007(\mathrm{E_{pv}} + \mathrm{E_{CsI}})) \text{ and} \\ \mathrm{E_{pv}} &< 2.3 \times \exp(-0.007(\mathrm{E_{pv}} + \mathrm{E_{CsI}})). \end{aligned} \tag{4.1}$$

Protons are defined as satisfying the requirement:

$$\mathrm{E_{pv}} < 2.3 \times \exp(-0.007(\mathrm{E_{pv}} + \mathrm{E_{CsI}})). \tag{4.2}$$

If the total energy in CsI's is greater than 200 MeV, it is considered caused by cosmic muons.

Photons are defined as satisfying the requirement:

$$\mathrm{E_{pv}} < 0.2 \times \exp(-0.007(\mathrm{E_{pv}} + \mathrm{E_{CsI}})) \text{ if no chamber hits} \tag{4.3}$$

All other showers are not classified.

4.2 Extracting $\pi\beta$ events

The signature of $\pi^+ \to \pi^0 e^+ \nu$ decay is two nearly anti-collinear γ's from $\pi^0 \to \gamma\gamma$ detected in the calorimeter at least 3 ns after the π^+ stops in the target. To select such an event, candidates need to satisfy several conditions:

- two-arm high threshold trigger ($\mathrm{PB_{HI}}$),
- no cosmic events, which states that total energy in CsI's is less than 200 MeV and timing registered in cosmic veto detector is outside a 140 ns window (no in-time hits in cosmic veto detector),
- no in-time hits in two active collimators,
- no prompt π^+'s. This condition is fulfilled by requiring the timing difference between beam counters and CsI to be greater than a certain amount,
- no charged particles detected in the direction of candidate clumps,
- pibeta discriminator function f_D is required. The pibeta discrimination function sets a limit on the relation between the energies (E_{γ_1} and E_{γ_2}) of the two γ's and the angle ($\theta_{\gamma\gamma}$) between the two γ's. It requires that:

$$\theta_{\gamma\gamma} > 180^\circ - 19^\circ \sqrt{1 - \left(\frac{X_{\gamma\gamma} - 0.47}{0.14}\right)^2}, \; X_{\gamma\gamma} = \frac{E_{\gamma_1}}{(E_{\gamma_1} + E_{\gamma_2})} \tag{4.4}$$

  or

$$\theta_{\gamma\gamma} > 180^\circ - 15^\circ \sqrt{1 - \left(\frac{X_{\gamma\gamma} - 0.48}{0.08}\right)^2}, \; X_{\gamma\gamma} = \frac{E_{\gamma_1}}{(E_{\gamma_1} + E_{\gamma_2})} \tag{4.5}$$

This will eliminate photon pairs that come from π^0's which are produced from a hadronic reactions instead of $\pi\beta$ decays from stopped π^+'s. The efficiency of this cut is evaluated in a Monte Carlo simulation.

- If there are more than two calorimeter showers detected meeting the above criteria, the two clumps from which the reconstructed π^0 invariant mass is closest to the π^0 rest mass (134.98 MeV) are selected. The invariant mass associated with each pair of CsI clumps is calculated by summing two clump energies (E_{γ_1} and E_{γ_2}) and then subtract the kinematic energy of π^0 from $\pi^+ \to \pi^0 e^+ \nu$ decay, as in following equation:

$$\begin{aligned} m_{\pi^0}^2 &= (E_{\gamma_1} + E_{\gamma_2})^2 - (E_{\gamma_1} \cdot \cos\theta_{\gamma_1}^x + E_{\gamma_2} \cdot \cos\theta_{\gamma_2}^x)^2 \\ &\quad -(E_{\gamma_1} \cdot \cos\theta_{\gamma_1}^y + E_{\gamma_2} \cdot \cos\theta_{\gamma_2}^y)^2 - (E_{\gamma_1} \cdot \cos\theta_{\gamma_1}^z + E_{\gamma_2} \cdot \cos\theta_{\gamma_2}^z)^2 \end{aligned}$$

The effectiveness of the selection rules can be shown by comparing the experimental results of selected physical variables with those from GEANT simulation. Figure 4.1 shows the total energy of two γ's. The energy response of CsI was adjusted using the energy peak position of positrons from $\pi^+ \to e^+ \nu$ decay, and the agreement of $\pi^+ \to \pi^0 e^+ \nu$ energy spectra shows the goodness of the simulation. Fig. 4.2 shows the angle between two γ's from π^0 decay.

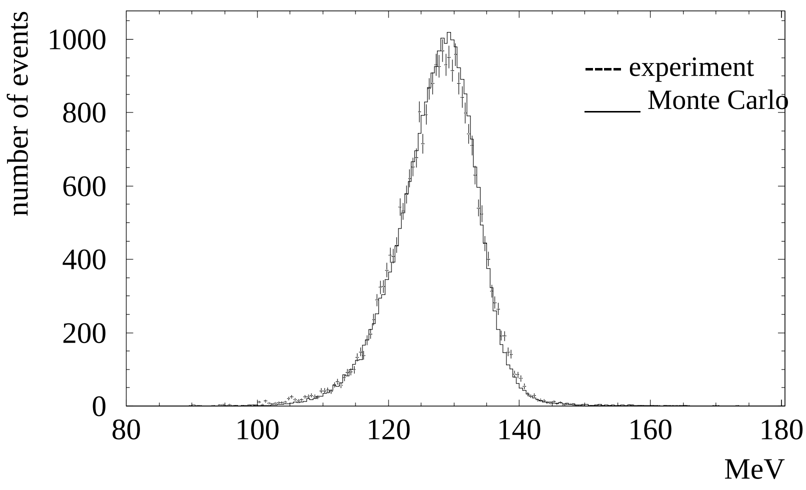

Figure 4.1: Energy sum of two γ's from π^0 decay.

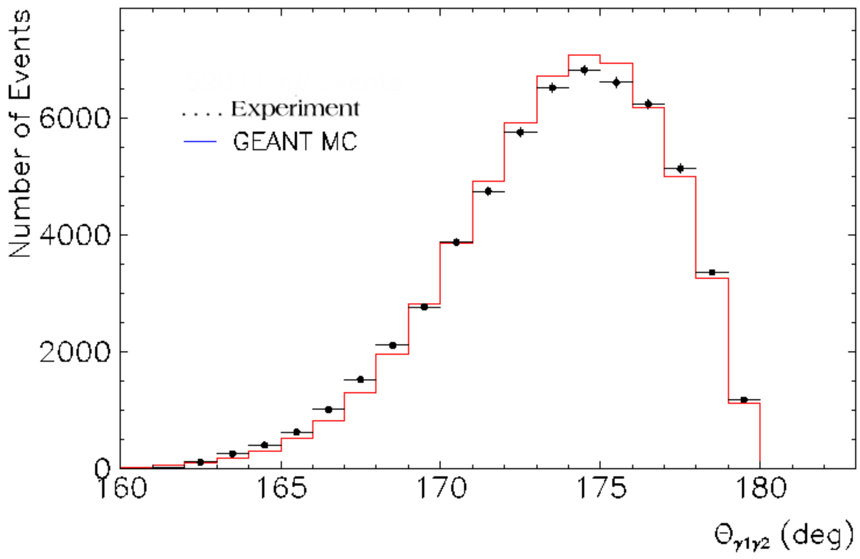

Figure 4.2: Angles between two γ's from π^0 decay.

Table 4.1: Number of $\pi^+ \rightarrow \pi^0 e^+ \nu$ events.

Year	Number of events	Uncertainty
1999	8467 ± 92	1.1%
2000	28130 ± 168	0.6%
2001	27450 ± 166	0.6%

The number of $\pi^+ \rightarrow \pi^0 e^+ \nu$ events from each year of runs is given in Table 4.1. The uncertainties are statistical uncertainties.

Chapter 5

Extracting $\pi 2e$ events from experiment

the Number of $\pi^+ \to e^+\nu$ decays can be obtained from both the positron energy spectrum and the decay timing line shape. The two methods yield consistent results. Since this decay channel is used for normalization in pion beta decay branching ratio calculation method, the conditions to get above numbers are not optimized for evaluating the absolute $\pi^+ \to e^+\nu$ decay branching ratio.

5.1 Energy spectrum

In the replay analysis the one-arm high-threshold trigger ($\mathrm{PIENU_{HI}}$) data were further prescaled in software by a factor of 20 to reduce the size of the data set to manageable level. $\pi^+ \to e^+\nu$ candidate events must meet the following additional requirements:

- No cosmics:
  1. the total energy deposited in CsI's is less than 200 MeV;
  2. No in-time hit from cosmic muon vetoes.
- No scattered particles: no in-time hits in either active collimator,
- At least one charged particle: at least one hit from each chamber and plastic vetoes,
- If two or more candidate e^+ tracks are found in a single event, a track with total energy (CsI+pv) closest to 68 MeV is selected.

The minimum ionizing charged particles were identified by cuts applied on the energy deposited in the PV's and CsI's, as shown in section 4.1 about particle identification. The efficiency of this application is evaluated in Monte Carlo and absorbed into the acceptance evaluation. This factor needs to be evaluated for each year's data set separately.

5.1.1 Determining Subtraction Factor $\mathrm{f_{sub}}$

A clean $\pi^+ \to e^+\nu$ energy spectrum was obtained by subtracting the energy spectrum projected from the late time bin $70 \leq t \leq 130\,\mathrm{ns}$ ($\pi\mathrm{G_L}$) ($\mathrm{N_L}$) from the spectrum cut on the early time bin $10 \leq t \leq 70\,\mathrm{ns}$ ($\pi\mathrm{G_E}$) ($\mathrm{N_E}$). Each event was weighted by the time-dependent hardware prescaling factor that was constant for a series of runs. The subtraction is used to eliminate the background events coming mainly from $\mu^+ \rightarrow e^+\nu\overline{\nu}$ decays. The number of events between 10 ns and 70 ns is calculated as $\mathrm{N}' = \mathrm{N_E} - \mathrm{f_{sub}} \times \mathrm{N_L}$. The subtraction factor $\mathrm{f_{sub}}$ is determined by comparing the experimental energy spectrum with that from Monte Carlo simulations. Since this factor is used to estimate the low energy tails of the positron line-shape that is cut by the high energy threshold (around 50 MeV), the lower energy edge plays a more important role. By changing the fitting energy range, one can estimate the uncertainties of this method. Since this factor also affects extracting $\pi^+ \rightarrow e^+\nu$ decay events from the timing spectrum (see next Section), one can check consistency by comparing the number of events from the energy spectrum and the timing spectrum. The lower energy fitting limit corresponds to the software energy threshold cut, the upper energy fitting limit determines which segment of the energy spectrum is used for fitting and thus should not change the goodness of the fit if the simulation is adequate. Indeed, the variance induced by varying the upper limit is negligible (compared with the difference between the numbers of $\pi^+ \rightarrow e^+\nu$ decay events extracted from the energy spectrum and the timing spectrum). Figure 5.1 shows the percentage difference of the number of events extracted from the timing spectrum and the energy spectrum.

There are two parameters in our GEANT simulation that need to be adjusted in getting a subtraction factor. One factor is to adjust the energy resolution of CsI's, the other is to adjust gains of CsI's. Combined with the subtraction factor, the best matched results (least χ^2) between GEANT simulation and experiment can be obtained. Figure 5.2 illustrates the dependence of χ^2 on the gain factor with a fixed energy resolution factor. It also illustrates a way to evaluate the uncertainties on $\mathrm{f_{sub}}$.

5.1.2 Over-subtraction correction factor f_{ADC_corr} for ADC subtraction

The goal of ADC subtraction is to subtract the background events (dominated by Michel decay events) from $\pi^+ \to e^+\nu$ decays in the 10 ns to 70 ns time window. Denote the number of $\pi^+ \to e^+\nu$ decay events in the 10—70 ns time window with $\mathrm{N_{\pi 2e_{10-70}}}$, events in the 70—130 ns time window with $\mathrm{N_{\pi 2e_{70-130}}}$, the background events in the 10—70 ns time window with $\mathrm{N_{bg_{10-70}}}$, the background events in the 70—130 ns window with $\mathrm{N_{bg_{70-130}}}$. The experimental data are still denoted by $\mathrm{N_E}$ for events in the 10—70 ns time window and $\mathrm{N_L}$ for events in the 70—130 ns time window as used above. The following derivations are aimed to get $\mathrm{N_{\pi 2e_{10-70}}}$.

With the above notations, we have

$$\mathrm{N_E} = \mathrm{N_{\pi 2e_{10-70}}} + \mathrm{N_{bg_{10-70}}}, \tag{5.1}$$

$$\mathrm{N_L} = \mathrm{N_{\pi 2e_{70-130}}} + \mathrm{N_{bg_{70-130}}}. \tag{5.2}$$

After the afore-mentioned subtraction, the best fit is obtained essentially by finding the $\mathrm{f_{sub}}$ such that $\mathrm{N_{bg_{10-70}}} - \mathrm{f_{sub}} \times \mathrm{N_{bg_{70-130}}} = 0$.

Then

$$\mathrm{N_E - f_{sub}N_L = N_{\pi 2e_{10-70}} - f_{sub}N_{\pi 2e_{70-130}}}. \tag{5.3}$$

and from the exponential $\pi^+ \to e^+\nu$ decay curve, we have

$$\mathrm{N_{\pi 2e_{10-70}} = C(e^{-10/\tau_\pi} - e^{-70/\tau_\pi})}, \tag{5.4}$$

$$\mathrm{N_{\pi 2e_{70-130}} = C(e^{-70/\tau_\pi} - e^{-130/\tau_\pi})}, \tag{5.5}$$

which gives

$$\mathrm{ratio} = \frac{\mathrm{N_{\pi 2e_{10-70}}}}{\mathrm{N_{\pi 2e_{70-130}}}} = 0.0998, \tag{5.6}$$

in which $\tau_\pi = 26.03$ ns and C is a constant.

From the above equations, we get

$$\mathrm{N_E - f_{sub}N_L} = \mathrm{N_{\pi 2e_{10-70}} - f_{sub} \cdot ratio \cdot N_{\pi 2e_{10-70}}}, \tag{5.7}$$

$$\mathrm{N_{\pi 2e_{10-70}}} = \mathrm{(N_E - f_{sub}N_L)} \times \frac{1}{1 - \mathrm{ratio} \times \mathrm{f_{sub}}}. \tag{5.8}$$

The uncertainty in $\mathrm{f_{sub}}$ is propagated to get the uncertainty in the number of events.

The Numbers of $\pi^+ \to e^+\nu$ decay events extracted using the described methods are summarized in Table 5.1.

5.2 e$^+$ timing spectrum method

The number of $\pi^+ \to e^+\nu$ events can also be obtained independently from the e^+ timing spectrum. After applying all the cuts mentioned in the previous section, the

e^+ timing spectrum is shown in Figure 5.3. The spectrum apparently depends on the high threshold energy cut. This timing spectrum can be described with

$$
\begin{aligned}
\mathrm{f_{HT}(t)} &= \theta(\mathrm{t})\alpha_1\lambda_\pi \mathrm{e}^{-\lambda_\pi \mathrm{t}} + \theta(\mathrm{t})\alpha_2\phi(\mathrm{t}) + \alpha_3 \sum_{\substack{\mathrm{n}=-\infty \\ \mathrm{n}\neq 0}}^{\mathrm{n}=\infty} \theta(\mathrm{t}-\mathrm{t_{rf}n})\lambda_\pi \mathrm{e}^{-\lambda_\pi(\mathrm{t}-\mathrm{t_{rf}n})} + \\
&\quad \alpha_4 \sum_{\substack{\mathrm{n}=-\infty \\ \mathrm{n}\neq 0}}^{\mathrm{n}=\infty} \theta(\mathrm{t}-\mathrm{t_{rf}n})\lambda_\pi \phi(\mathrm{t}-\mathrm{t_{rf}n}), \qquad (5.9)
\end{aligned}
$$

in which $\theta(t)$ is the step function, that is

$$
\theta(t) = \begin{cases} 1 & \text{if } t \geq 0 \\ 0 & \text{if } t > 0. \end{cases}
$$

α_1,α_2,α_3, α_4 are four parameters describing the ratio of each decay component in the registered e^+ timing spectrum. λ_π and λ_μ are π^+ and μ decay rates respectively. $\phi(t)$ describes the sequential $\pi^+ \to \mu \to e^+$ decay chain:

$$
\phi(\mathrm{t}) = \frac{\lambda_\pi \lambda_\mu}{\lambda_\mu - \lambda_\pi}(\mathrm{e}^{-\lambda_\pi \mathrm{t}} - \mathrm{e}^{-\lambda_\mu \mathrm{t}}), \qquad (5.10)
$$

The first term in Eq 5.9 is due to genuine $\pi^+ \to e^+\nu$ decays, the second term gives the fraction of the $\pi^+ \to \mu^+ \to e^+$ positrons above the high energy threshold. The third and fourth terms represent the positron pile-ups from the decays of π^+'s stopped before the one that started the pion gate and μ's accumulated in the target. The pion and muon decay rates are $\lambda_\pi = 1/26.03\,\mathrm{ns}$ and $\lambda_\mu = 1/2197.03\,\mathrm{ns}$ respectively [1]. t_{rf} is the 19.750 ns time period between the cyclotron pulses. The fractions of α_{1-4} depend on the π^+ beam stopping rate and explicitly include the pile-up effects.

The above equation takes into account the accidental event pileups but not the time shuffling in experimental data. The time shuffling concerns the way the degrader timing is registered—how decay products are assigned to the original π^+'s when there are pileup events. In the experimental data, the original π^+ is picked out as the one that is closest to the trigger timing. The Monte Carlo program (Appendix D) simulates $\pi^+ \to e^+\nu$ and $\mu^+ \to e^+\nu\overline{\nu}$ decays at a certain beam rate, then the MINUIT program finds the portion of each decay — α_1 for $\pi^+ \to e^+\nu$ and α_2 for $\mu^+ \to e^+\nu\overline{\nu}$ — that fits the experimental data best. By varying the rate and repeating the above process, the best fit was obtained. The number of $\pi^+ \to e^+\nu$ events is the integration of $\pi^+ \to e^+\nu$ portion within the 10—70 ns gate. The fit is shown in Figure 5.3. The fitting parameters, along with the corresponding number of $\pi^+ \to e^+\nu$ events, are in Table 5.1. The simulated beam rate was varied in a 50 k step. The uncertainty in the number of $\pi^+ \to e^+\nu$ events is taken as the difference of numbers of events with minimum χ^2 and when the beam rate is 50k higher (or lower) than the beam rate where the minimum χ^2 was obtained.

Table 5.1: Number of the $\pi^+ \to e^+\nu$ events

Year	The Number of events from ADC spectra	Number of events from TDC
1999	$0.4365\,(7) \times 10^7$	$0.4300\,(4) \times 10^7$
2000	$0.1379\,(2) \times 10^8$	$0.1376\,(2) \times 10^8$
2001	$0.1238\,(2) \times 10^8$	$0.1238\,(3) \times 10^8$

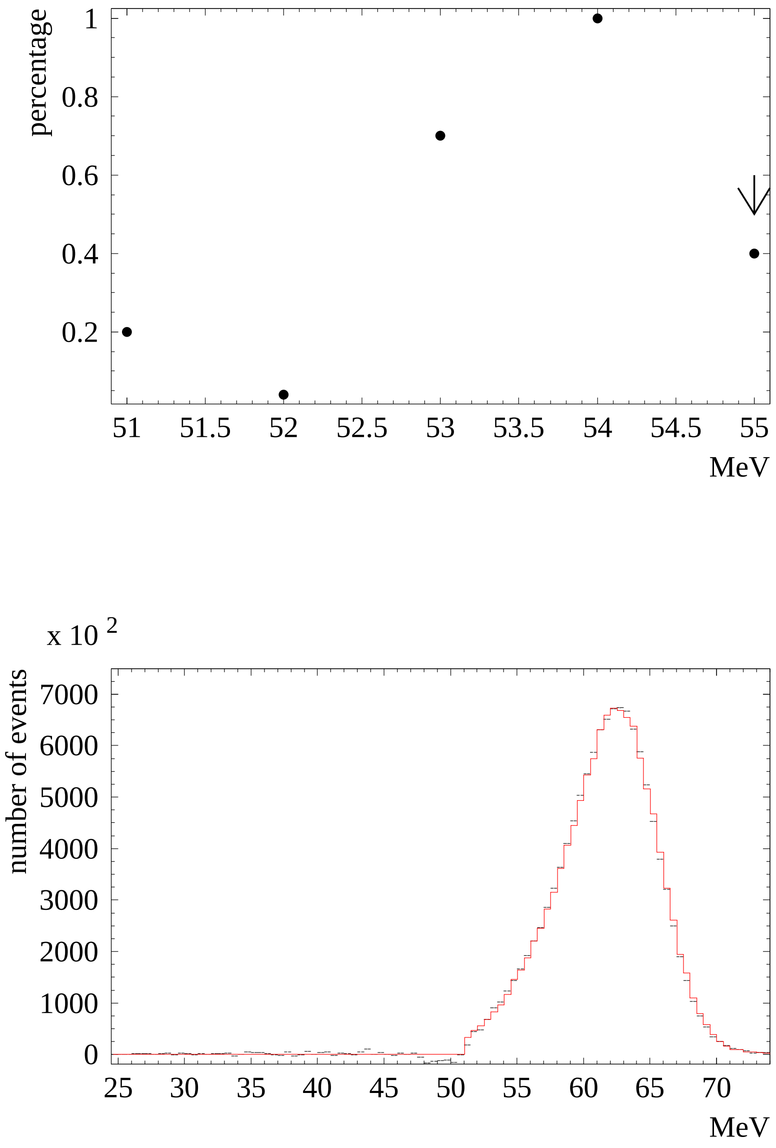

Figure 5.1: Top panel: Difference of the number of events extracted from the energy spectrum and the timing spectrum as a function of the energy threshold. The last point (at 55 MeV) corresponds to a fitting range from 55 MeV to 74 MeV to illustrate the goodness of the detector simulation in Monte Carlo. Bottom panel: the energy spectrum thus obtained compared with that from the MC simulation.

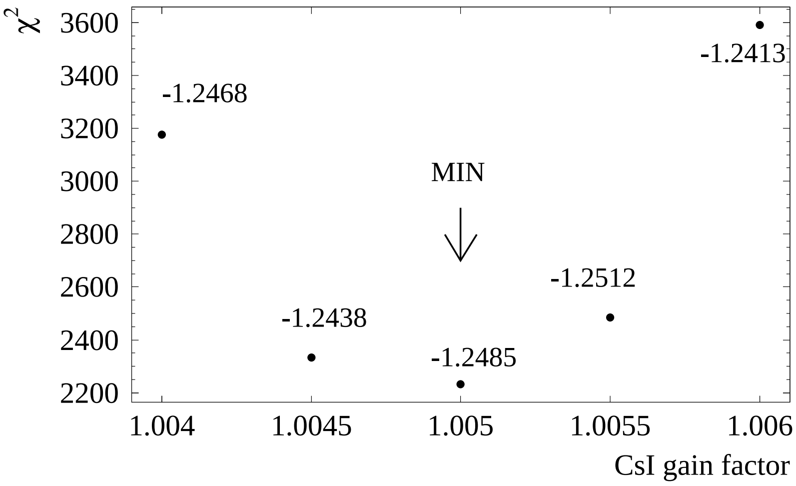

Figure 5.2: χ^2 vs. CsI gain factor. Subtraction factors (f_{sub}) are also shown. For each gain factor there is a best subtraction factor, the one that has the smallest χ^2 is selected, and the difference of subtraction factor between the selected one and its neighbors can be treated as uncertainty if this difference is greater than the uncertainty associated with the selected one.

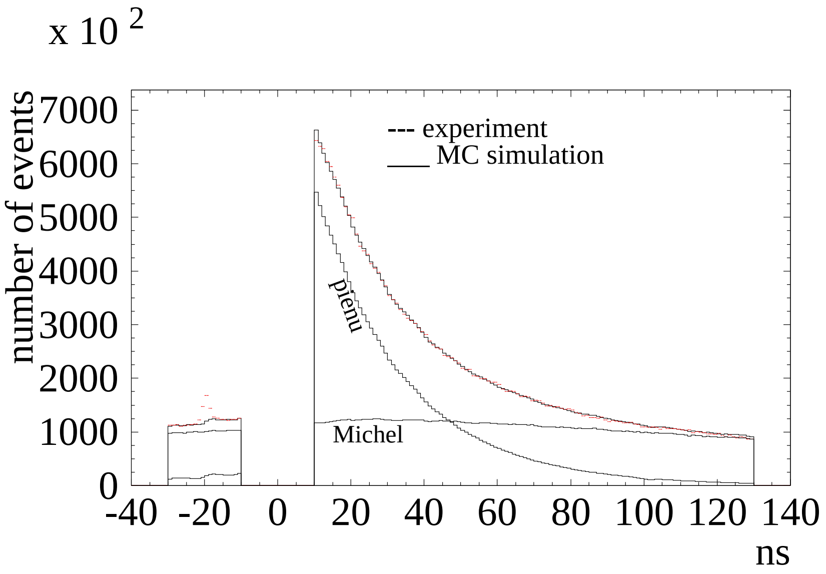

Figure 5.3: Timing spectra of e^+ from $\pi 2e$ decays. The resulting timing spectrum is the summation of the spectra of e^+'s from $\pi 2e$ and Michel decays. The pike at $-20\,\mathrm{ns}$ is due to hadronic interactions and was excluded in the fitting.

Chapter 6

π^+ Stopping Distributions and detector acceptance

Obtaining the precise pion stopping distribution in the target is essential in calculating the detector acceptance, which plays an important part in over-all systematic uncertainty. Backtracking tomography uses track information obtained from the multi-wire proportional chambers to reconstruct the pion stopping distribution in the target.

When combining the full data set spanning several years, one has to realize that although in each run the π^+ distribution is the same for different π^+ decay channels, each run's distribution weights differently for different decay channels in the full data set, since prescaling factors are different from run to run.

6.1 Backtracking Tomography

Knowing the π^+ stopping vertex of each event in the target is not our concern (and not possible). We need to know the π^+ vertex distribution for the full sample of recorded events in terms of x, y, z, in which x and y define the horizontal plane and z

the direction the beam is going. Inspired by an algebraic reconstruction technique [37] which has been widely used as an imaging method in medical physics, we developed the backtracking tomography method to determine the π^+ stopping distribution.

The space containing the target is divided into small cubic cells. The position (x, y, z) in this space can be denoted by the indices of a cube described by (nx, ny, nz) enclosing this point. In the above example, $nx = int(x/size\_of\_cell)$, etc., see Fig 6.1.

The track of a charged particle can be reconstructed from MWPC data. We extend this track to intersect the fiducial volume enclosing the target, calculate the 'path-length' in each cube, and sum the path-length values for each cube. The path-length is the length of a segment of the track in a cell. After processing large numbers of tracks, the accumulated path-lengths in each cube will reflect the probability of pions stopping in that cube.

The Monte Carlo method is used to study the correspondence between output path-length distributions and input pion stopping distributions in the target. All the details which affect the track definition are considered in Monte Carlo including the MWPC resolution and the target size.

There are three stages in this method. First, one has to optimize the cell size. At this stage, for each cell size, different Gaussian distributions with different spreads in the target were simulated and the correspondence between stopping distributions and path-length distributions was studied. The optimized cell size should give good results

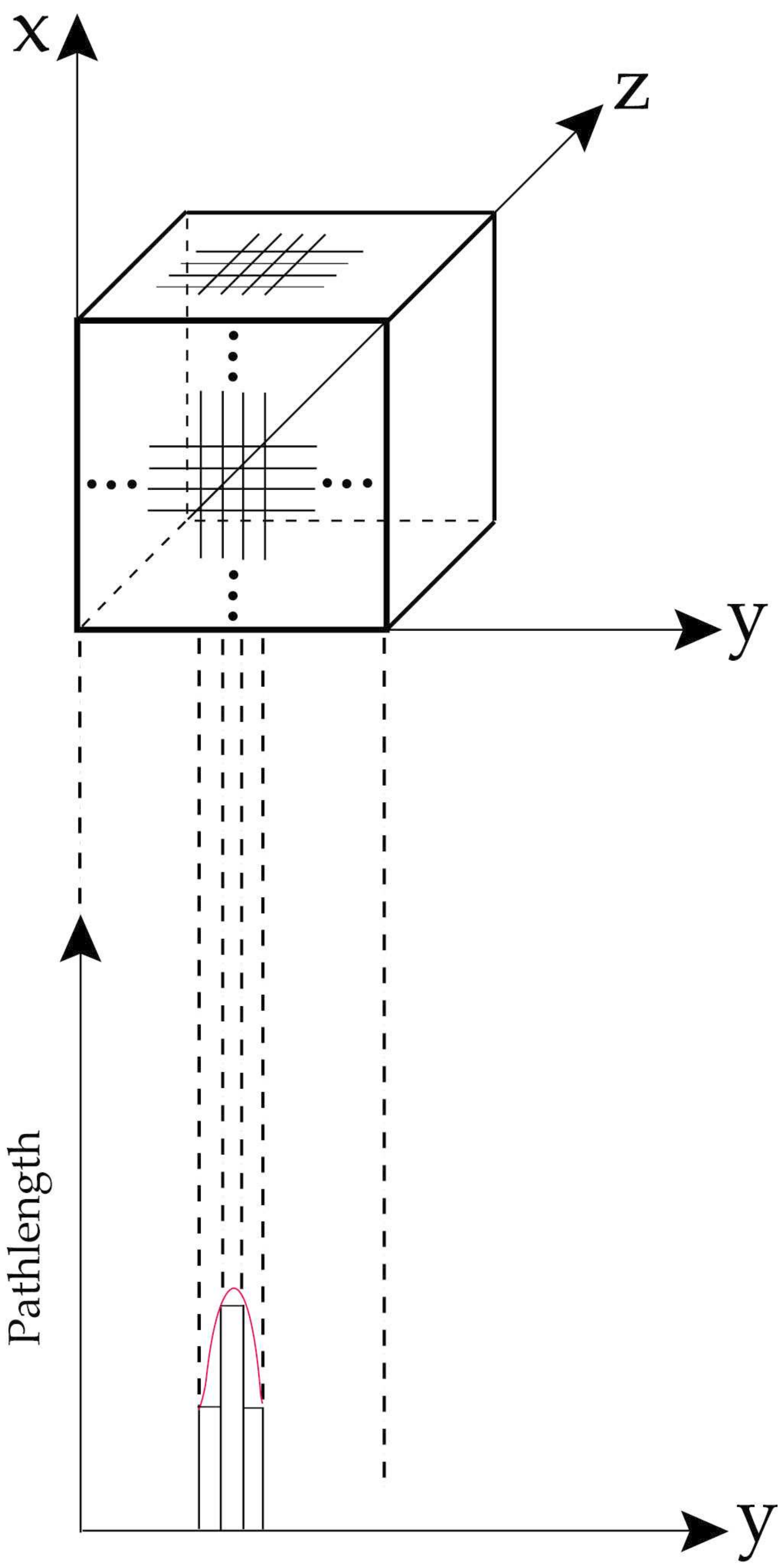

Figure 6.1: Tomography algorithm: divide space into small cubes and calculate pathlength in each cube for tracks.

in reasonable computation time. Second, we assume a reasonable π^+ distribution in the target and compare the MC results with the experimental data. Third, we modify the assumed distribution to get the best agreement between MC and experiment. The best distribution function would consist of numerical functions which can take into account all details. However, in the second stage, the analytical functions we used to describe the distributions reflected the major structures of the distribution line shape, which helps us in understanding the features of the beam distribution.

6.1.1 Track selection

To limit the accumulation of path-lengths that do not contain information for extracting the stopping distribution, tracks selected should be as perpendicular as possible to the axis in whose direction the distribution is calculated. Only tracks falling within a minimum angle to that axis were selected. Since the smaller the angle range, the cleaner the signal, and the lower the statistics, one has to balance these factors so that both statistics and cleanness are reasonable.

We take x as an example, tracks whose angle with x is small contribute similar path-lengths to a series of cells along the x coordinate, which adds nearly equal path-lengths to each of these cells, thus increasing the total background of the path-length distribution in x . However, if only tracks that are nearly perpendicular to the x axis are selected, these tracks will contribute path-lengths only to adjacent cells in terms of x position. The more perpendicular the angles between the tracks and the x axis, the more precisely the path-length distribution represents a real particle distribution, and the lower the statistics that can be collected, which means larger statistical error. By experimenting with different angle cuts, the optimum angle is found to be 10°.

6.1.2 The Best Cell Size

From beam-line simulation [22] the pion stopping profile in the target can be obtained. Because there is a thin carbon plate in the beam line to screen out the e^+'s and μ^+'s , the distribution of π^+'s in the horizontal plane also becomes asymmetric, which can be approximated with an asymmetric Gaussian:

$$p(x) = \begin{cases} e^{-\frac{(x-x_0)^2}{2\sigma^2_{x_{left}}}} & \text{if } x < x_0 \\ e^{-\frac{(x-x_0)^2}{2\sigma^2_{x_{right}}}} & \text{if } x > x_0 \end{cases} \tag{6.1}$$

The distribution in the vertical plane is Gaussian:

$$p(y) = e^{-\frac{(y-y_0)^2}{2\sigma_y^2}} \tag{6.2}$$

The distribution in z is a Gaussian riding on a 2% uniform background:

$$p(z) = 0.98 \times \frac{1}{\sigma_z\sqrt{2\pi}} e^{-\frac{(z-z_0)^2}{2\sigma_z^2}} + 0.02 \times \frac{1}{z_l - z_r} \tag{6.3}$$

in which z_l and z_r are end points between which the distribution is considered.

In MC, particles in Gaussian distribution with known distribution parameters are generated and the path-length distribution corresponding to this set of particles are also obtained. The path-length distribution is then fitted with a Gaussian to the Full-Width-Half-Maximum. The obtained σ of the Gaussian is used as a feature variable to describe the path-length distribution, namely, each path-length distribution is described with a corresponding σ_p. For each cell size, Gaussian distributions with different σ's are simulated and the corresponding σ_p's of path-length distributions are obtained. A one-to-one correspondence between σ of the particle distribution in the target and σ_p of the corresponding path-length distribution is then established.

The above one-to-one correspondence is apparently a function of cell size. To test the consistency of the method and find the best cell size, four sets of synthetic data of Gaussian distribution with the same σ's are used as an input particle distribution, the center of each distribution is at the origin. The extracted σ using different cell sizes are then compared with the known σ to get the systematic correction.

6.1.3 Distribution in the vertical plane (y) and the longitudinal plane (z)

Since distributions in Y and Z are Gaussian, the one-one correspondence is very straightforward.

For the y distribution, the synthetic data are Gaussian with σ equal to 10.003 ± 0.0015 mm and centered at $y = 0$ mm. Those parameters are also representative of our experimental distributions. Four sets of data are generated in the simulation and the calculated σ's are showed in Figure 6.2.

At cell size equal to 0.3 mm, the difference between σ of the particle distribution in the target and σ calculated with the path-length one-to-one relation is $y_{corr} =$

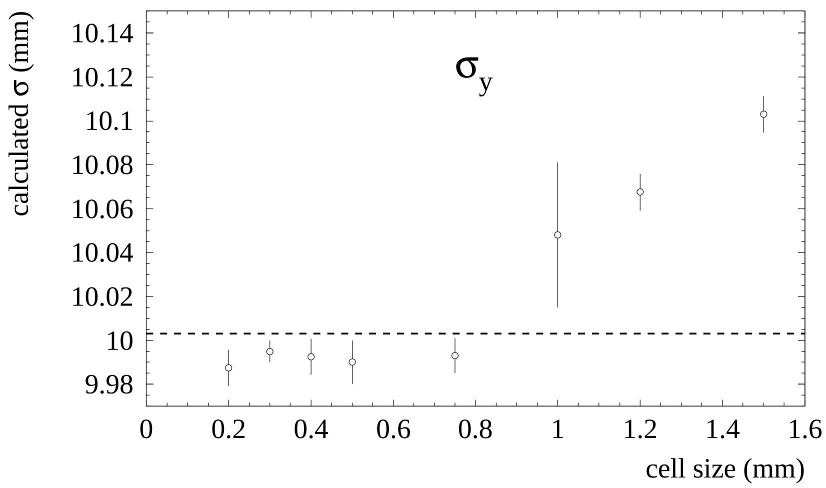

Figure 6.2: The relationship between calculated σ from path-length using one-to-one relation in y and cell size (s_c). The dashed line is the σ of Gaussian describing the particle distribution generated in the target.

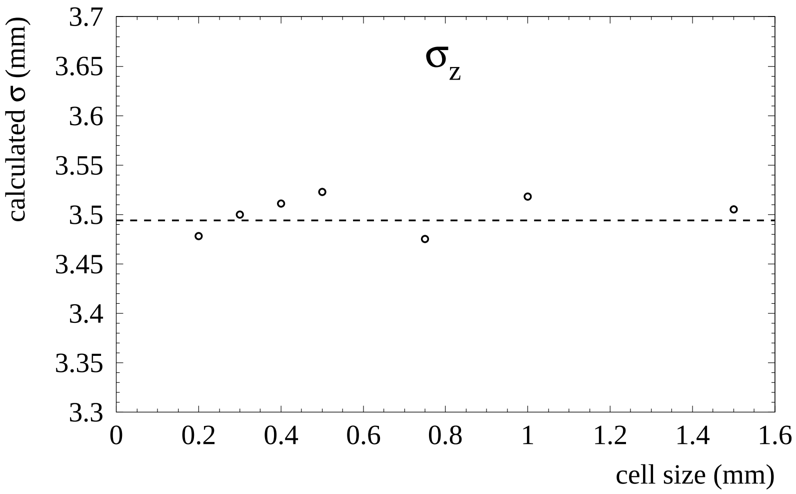

Figure 6.3: The relationship between calculated σ from path-length using one-to-one relation in z and cell size (s_c). The dashed line is the σ of Gaussian describing the particle distribution generated in the target.

0.008 ± 0.005 mm. This is the systematic correction that needs to be applied when using this method.

For the z distribution, the synthetic data are Gaussian with σ equal to 3.4940 ± 0.00085 mm centered at 8.5 mm and superimposed on a 2% constant distribution which is representitive of our experimental distribution. Again four sets of data are generated in the simulation and the calculated σ's are showed in Figure 6.3. At cell size equal to 0.3 mm, the correction that needs to be applied is $z_{corr} = 0.005 \pm 0.0018$ mm.

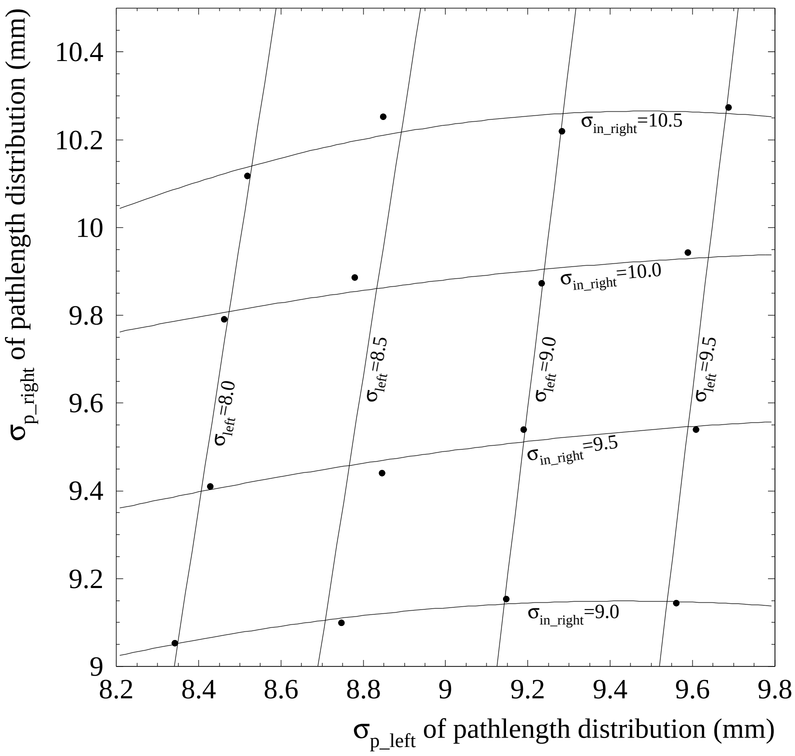

Figure 6.4: Lookup table to determine σ_{left} and σ_{right} in x. σ_{left} and σ_{right} are same as those in Eq. 6.1 respectively.

6.1.4 Distribution in the horizontal plane (x)

The distribution in x as described by Eq. 6.1 is more complicated to determine since there are two free parameters— σ_{left} and σ_{right}. Variation in one variable affects the other.

To determine σ_{left} and σ_{right}, one needs to make a lookup table combining these two variables. A table for a cell size equal to 0.3 mm is presented in Figure 6.4.

As one can see from Figure 6.4, the lookup table is two-dimensional, and monotonic in each direction, which was achieved only after applying angular restrictions on charged particle tracks. To find the corresponding real vertex distribution described by σ_{left} and σ_{right} from path-length distributions, one needs to plot the position described by σ_{p_left} and σ_{p_right} of the path-length distribution in the lookup table, and then find the same position but relative to lines of σ_{left} and σ_{right} of the real particle distribution.

Four data sets with distributions in accordance with Eq. 6.1 with the same distribution characteristics (same σ_{left} and σ_{right}) are generated in the simulation, in which $\sigma_{left} = 8.8995 \pm 0.0005\,\mathrm{mm}$ and $\sigma_{right} = 10.001 \pm 0.0015\,\mathrm{mm}$. Results from the above scheme are presented in Figure 6.5

At cell size equal to 0.3 mm, the correction for σ_{left} is $0.0045 \pm 0.0087\,\mathrm{mm}$, the correction for σ_{right} is 0.0125 ± 0.046. Since the mean corrections are smaller than the statistical error, one can combine the mean correction and statistical error and simply states that the uncertainty for σ_{left} is 0.0098 mm and for σ_{right} is 0.048 mm.

The above calculations have been done with different cell sizes and the cell size equal to 0.3 mm is found to be the optimal choice after balancing the computation time and the systematic corrections.

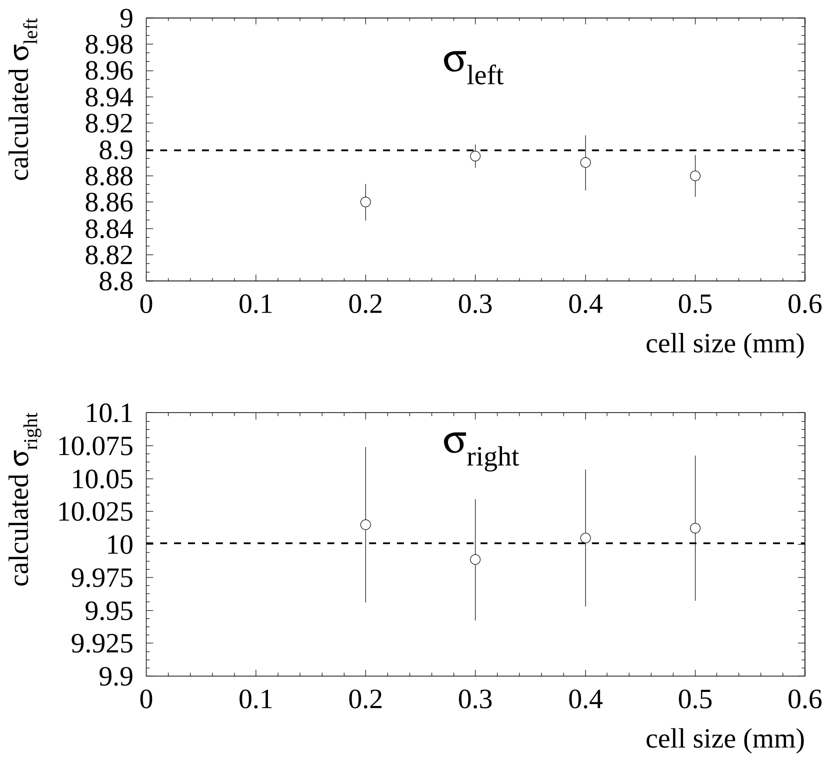

Figure 6.5: Calculated σ_{left} and σ_{right} of particle distribution in x $vs.$ cell size (s_c), compared with known $\sigma_{gen_{left}}$ and $\sigma_{gen_{right}}$ of distributions of particles generated in the target (dashed lines)

6.1.5 Refinement of the Distribution Functions

After applying the above method to the experimental data, slight discrepancies are found between the simulation and the experimental data, especially in the tails. The slight discrepancies indicate that the functions we used to describe beam distribution have reflected the main structures but do not include all subtleties. The easiest way to fix this is to use numerical functions. Based on the analytical distribution obtained above, iterations are used to find the best numerical function which has the smallest χ^2. By varying the widths and the range of the bins, the uncertainties associated with the algorithm can be obtained.

6.1.6 π^+ Distribution for Different Years and Different Decay Channels

Beam profile of $\pi^+ \to \pi^0 e^+ \nu$ decay for year 1999 runs

Horizontal(X) distribution

The numerical function f_x for x is found to be as shown in Figure 6.6, by varying the width of bins and offsets, the minimum χ^2 can be found as shown in Figure 6.7. From figure 6.7, the best numerical function with uncertainty is obtained: with 201 bins spanning from $x = -61.2 \times (1 + 0.000 \pm 0.00012)/2\,\mathrm{mm}$ to $x = 61.2 \times (1 + 0.000 \pm 0.00012)/2\,\mathrm{mm}$ and an offset $x_{off} = -0.0026 \pm 0.00071\,\mathrm{mm}$.

Y distribution

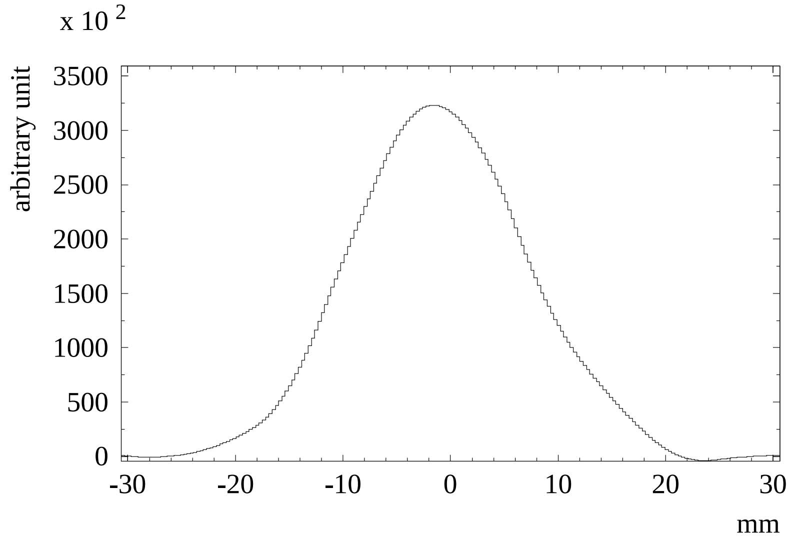

Figure 6.6: Numerical function f_x used for describing π^+ the horizontal (x) distribution for $\pi^+ \rightarrow \pi^0 e^+ \nu$ decay data of year 1999 runs.

The numerical function for y is found to be as shown in Figure 6.8, by varying the width of bins and offsets, the minimum χ^2 can be found as shown in Figure 6.9. From Figure 6.9, the best numerical function with uncertainty is obtained: with 201 bins spanning from $y = -61.2 \times (1 - 0.0026 \pm 0.00046)/2\,\mathrm{mm}$ to $y = 61.2 \times (1 - 0.0026 \pm 0.00046)/2\,\mathrm{mm}$ and an offset $y_{off} = 0.0087 \pm 0.00076\,\mathrm{mm}$.

Data from different years are processed following the above procedures. The π^+ distribution for $\pi^+ \rightarrow e^+ \nu$ decay is also obtained similarly.

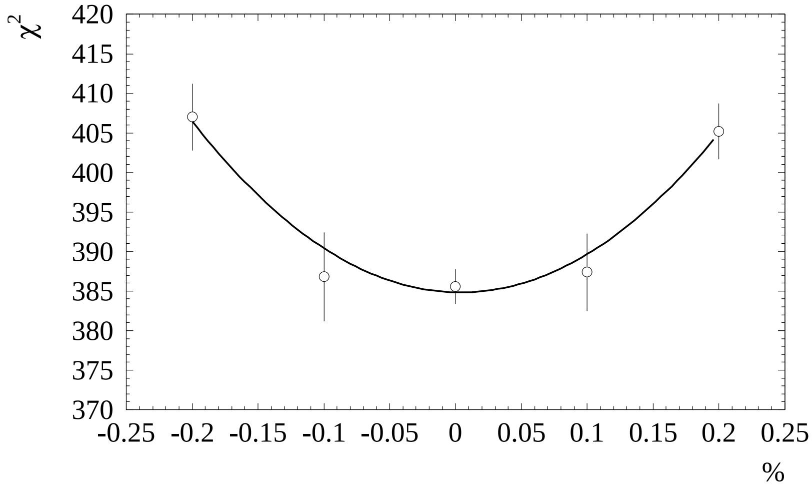

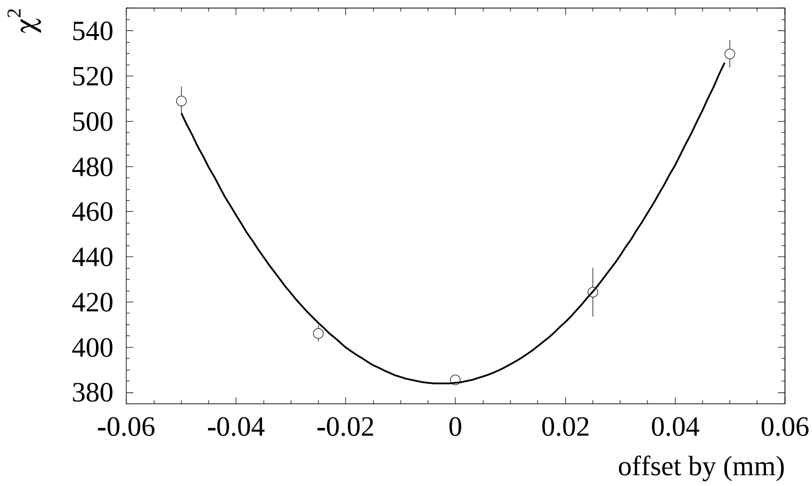

Figure 6.7: χ^2 dependence on the binning width (top) and on the offset of centroid (bottom) for function f_x.

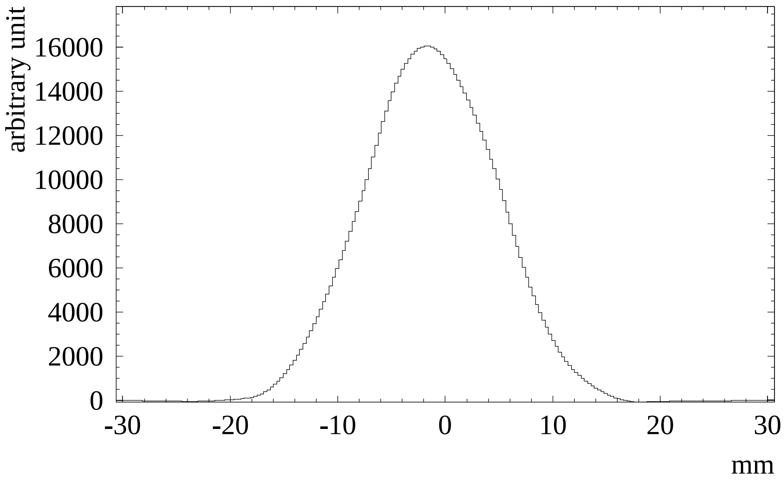

Figure 6.8: Numerical function f_y used for describing π^+ the vertical (y) distribution for $\pi^+ \to \pi^0 e^+ \nu$ decay data of year 1999 runs.

6.1.7 Summary of the above results

To get the best description of the beam profile in horizontal and vertical planes with the numerical functions f_x and f_y, one needs to modify the original numerical functions as in Figure 6.6 for the horizontal (X) π^+ distribution of runs in year 1999 , and as in Figure 6.8 for the vertical (Y) π^+ distribution of runs in year 1999, by expanding the range by x_0 fraction and adding an offset of x_{off}. The same applies to y. The modifications are summarized in Table 6.1 for $\pi^+ \to \pi^0 e^+ \nu$ decay and in Table 6.2 for $\pi^+ \to e^+ \nu$ decay.

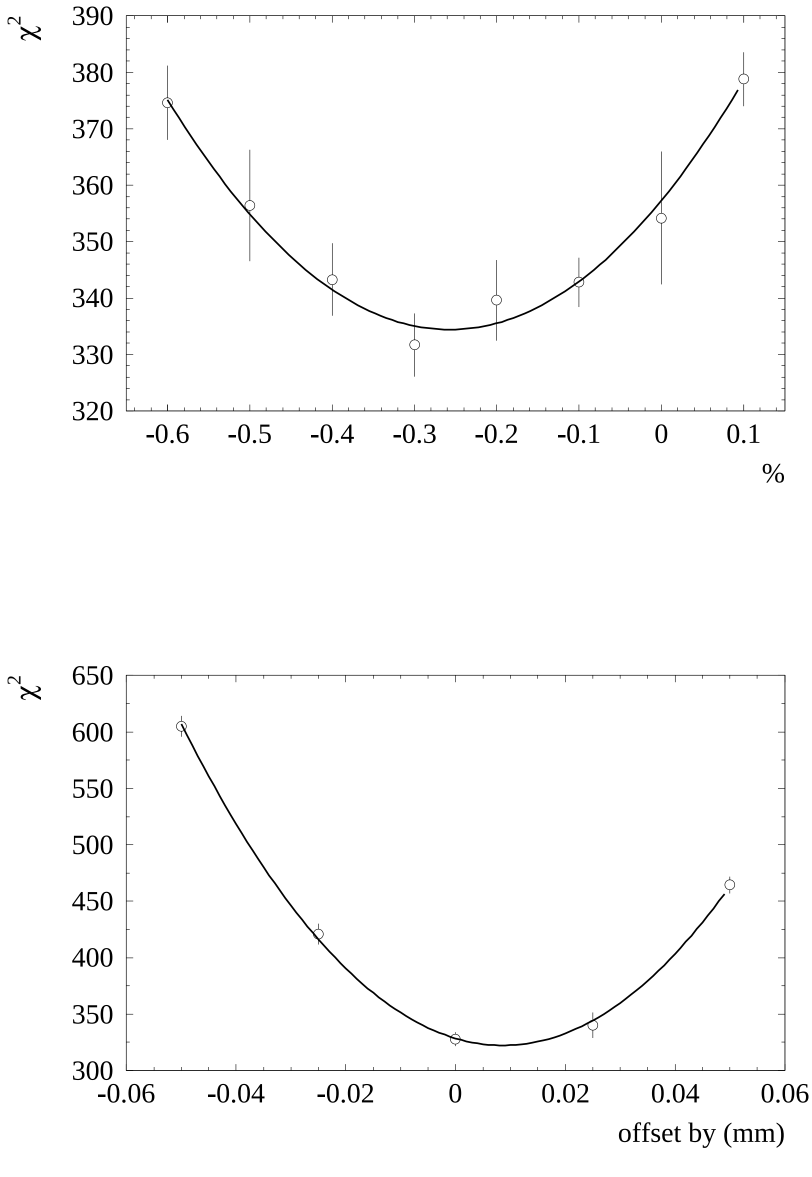

Figure 6.9: χ^2 dependence on binning width (top) and on offset of centroid (bottom) for function f_y.

Table 6.1: Summary of the parameters for modifying the numerical functions f_x and f_y describing $\pi^+ \to \pi^0 e^+ \nu$ decay beam profile.

	x_0	δx_0	x_{off}	δx_{off}	y_0	δy_0	y_{off}	δy_{off}
1999	0.00	0.012	0.0026	0.00071	−0.26	0.046	0.0087	0.00076
2000	0.105	0.037	0.0028	0.0012	0.22	0.04	0.0045	0.0007
2001	−0.13	0.079	−0.0022	0.0011	−0.095	0.015	−0.0034	0.00036

Table 6.2: Summary of the parameters for modifying the numerical functions f_x and f_y describing $\pi^+ \to e^+ \nu$ decay beam profile.

	x_0	δx_0	x_{off}	δx_{off}	y_0	δy_0	y_{off}	δy_{off}
1999	0.068	0.013	−0.0047	0.0011	−0.15	0.07	0.0066	0.0008
2000	−0.080	0.018	−0.0021	0.00071	0.20	0.07	0.0023	0.00074
2001	−0.041	0.016	−0.0079	0.00078	−0.100	0.018	0.000	0.0012

6.2 Longitudinal π^+ stopping distribution

The above results do not include the z distribution for several reasons. First, the acceptance is not sensitive to the z distribution. In fact, MC simulations show that 10 mm variation of z distribution results in $\sim 1\%$ uncertainty in the acceptance. Second, since the z distribution has a very small σ_z in terms of the Gaussian distribution, the above method may break down due to the intrisic nature of the method, namely, a δ-fuction distribution yields a path-length distribution with significent σ. Third, the MC simulation describes the longitudinal distribution fairly well.

The thicknesses of the beam-defining detectors, namely the forward beam counter, the active degrader and the active target are chosen to make the 40.6 MeV incident π^+ beam particles stop exactly in the center of the target. Our Geant3 Monte Carlo sim-

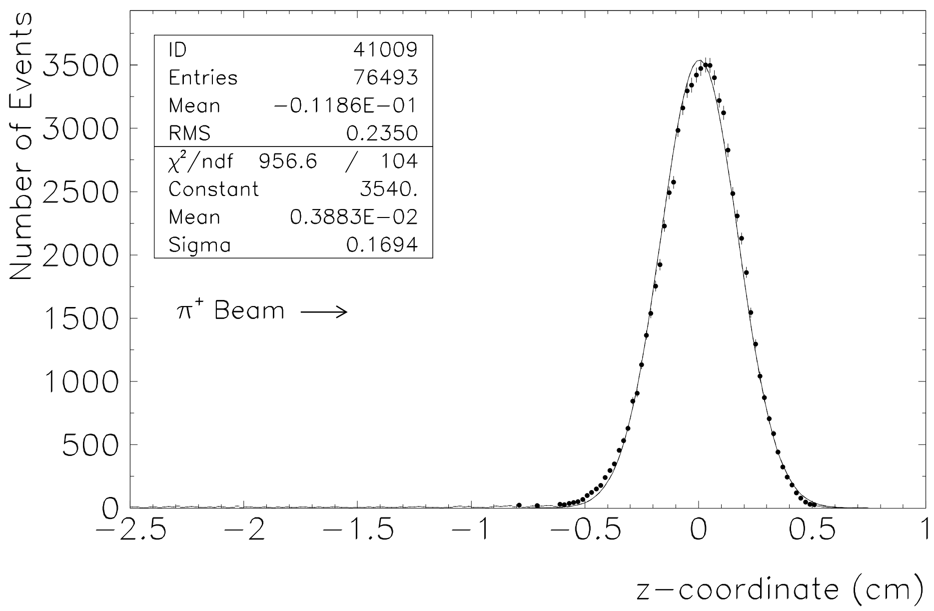

Figure 6.10: Beam distribution in longitudinal (z) direction.

ulation of the longitudinal vertex distribution of decaying π^+ is presented in Fig. 6.10. The input to the Monte Carlo is the π^+ momentum spectrum in Fig. 3.3. A histogram of the Monte Carlo z coordinates of π^+ decay vertices is a Gaussian function with a width of $\sigma_z = 1.69 \pm 0.01$ mm and a flat upstream tail integrating to $0.86 \pm 0.05\%$ events. The z position spread originates mainly from the energy straggling of stopping pions: the momentum spread of the incident beam contributes just 0.2 mm (or 12%) to the overall axial distribution spread. The upstream tail represents the π^+'s decay-in-flight events.

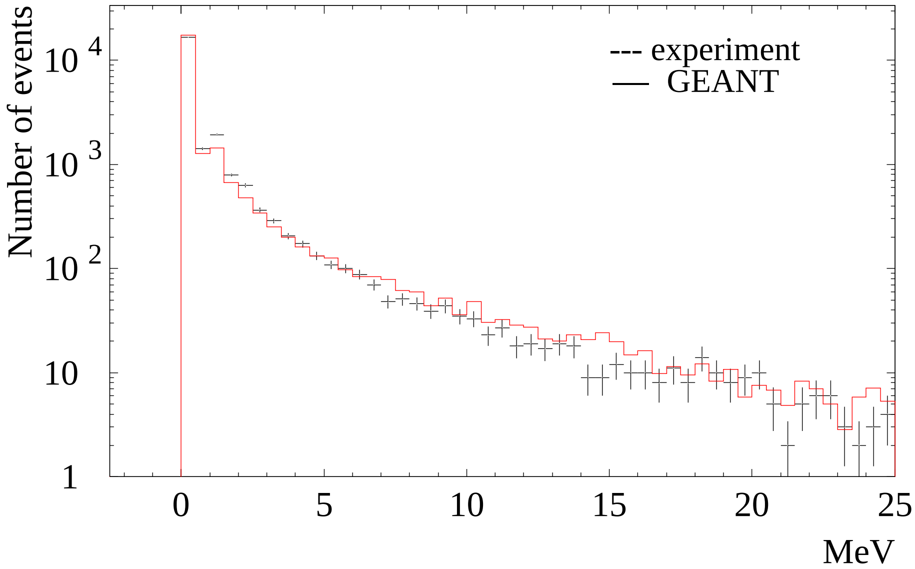

Figure 6.11: Energy deposited in CsI veto crystals for $\pi^+ \to \pi^0 e^+ \nu$ decay

6.3 Acceptance for $\pi\beta$ and $\pi 2e$ decays

The detector acceptance is determined by its geometrical parameters, such as the solid angles it covered and the stopping pion profiles. In addition, other factors that have to be determined by Monte Carlo are also absorbed into the acceptance. The GEANT simulation code is used to do the simulation after being finely adjusted to reflect the real detector response.

6.3.1 CsI veto crystals and plastic veto staves (PV)

All of the 40 CsI veto detectors have been adjusted in GEANT to reflect the CsI veto response in the real detector, as shown in Figure 6.11

Plastic veto gains and resolutions are adjusted in the GEANT so that the e^+

energy line-shape matches that from the experiment, as shown in the top panel in Figure 6.12. One can see from the bottom panel that the response of plastic vetoes to $\pi^+ \to \pi^0 e^+ \nu$ decay also shows good agreement with the data.

6.3.2 Other factors in calculating acceptance

Aside from the pion stopping distributions, other factors that affect the acceptance were also taken into account in MC simulations.

PIBETA discriminator function The effect of the pibeta discriminator function (see Eq. 4.4 and Eq. 4.5) is also absorbed into acceptance.

Photonuclear absorption. This concerns the probability that a photon converts into an electron-positron pair and thus decay products registered as charged particles.

All conditions applied in analyzing the experimental data for both $\pi^+ \to \pi^0 e^+ \nu$ and $\pi^+ \to e^+ \nu$ decay are implemented in calculating acceptances, including trigger cut, plastic veto hardware threshold, clump number cut, particle ID cut, π^+invariant mass cut, and track finding process (see appendix A and appendix B).

Radiative correction $\pi^+ \to e^+ \nu$ decay is always accompanied by $\pi^+ \to e^+ \nu \gamma$ decay. The e^+ from radiative pion decay has a low energy tail due to energy carried away by γ. This will affect the acceptance due to the low energy cut applied when calculating acceptance.

Acceptances of $\pi^+ \to e^+ \nu$ and $\pi^+ \to \pi^0 e^+ \nu$ for each year's settings are

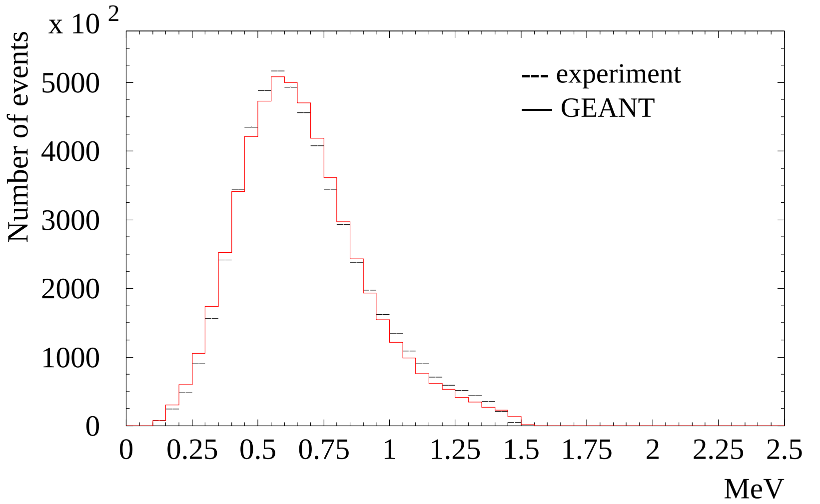

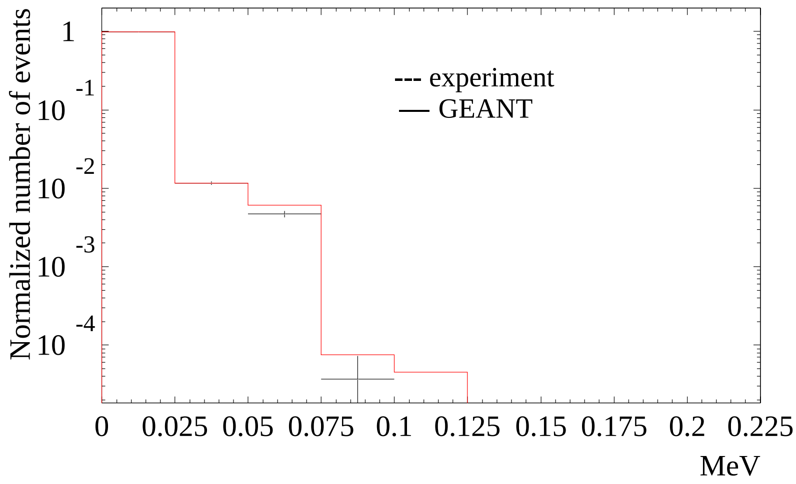

Figure 6.12: e^+ energy line-shape in PV (top) and photon energy line-shape in PV (bottom) for $\pi^+ \rightarrow \pi^0 e^+ \nu$ decay.

Table 6.3: Detector acceptances

year	$\pi^+ \to e^+\nu$	$\pi^+ \to \pi^0 e^+\nu$
1999	0.7040 (5)	0.6657 (6)
2000	0.7031 (6)	0.6594 (7)
2001	0.7039 (2)	0.6623 (7)

summarized in Table 6.3

Chapter 7

Other parameters in extracting $\pi\beta$ and $\pi 2e$ events

7.1 $\pi^+ \rightarrow \pi^0 e^+ \nu$ gate fraction $g_{\pi\beta}$

Since we can only detect events within a certain time period, the gate, following a π^+ stop, we need to calculate the probability that a decay occurs inside the gate. Equation 7.1 is used to calculate the $\pi\beta$ gate fraction:

$$g_{\pi\beta} = \frac{1}{s_t\sqrt{2\pi}} \int_{-\infty}^{+\infty} e^{-t'^2/\left(2s_t^2\right)} \left[\int_{t'+t_s}^{t'+t_f} e^{-t/\tau_{\pi^+}} dt\right] dt' \left[\int_0^{+\infty} e^{-t/\tau_{\pi^+}} dt\right]^{-1}, \tag{7.1}$$

where τ_{π^+} is the π^+ lifetime, t_s and t_f are the opening and closing times of the π^+ gate, both measured relative to the pion stopping time. s_t is the measured standard deviation of t_s and t_f, essentially the timing resolution.

Due to the exponential nature of the decay, the determination of t_s is important.

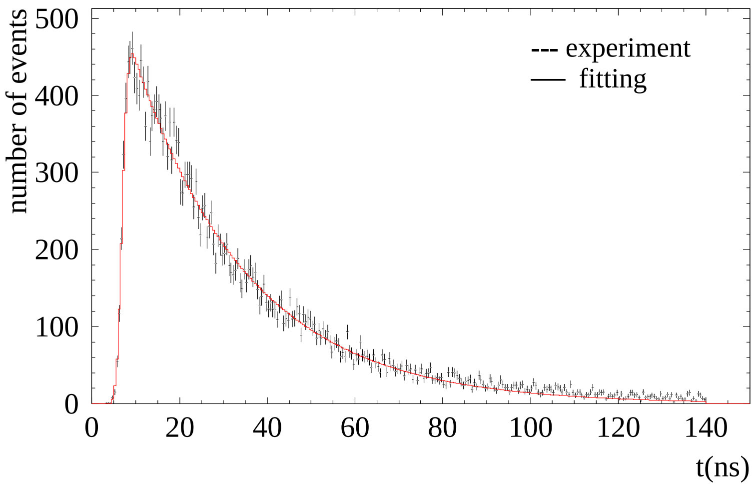

Figure 7.1: CsI timing of γ's (as defined in Eq. 7.2) in $\pi^+ \to \pi^0 e^+ \nu$ decay. Eq. 7.3 plus the pileup correction is used as fitting function. The experimental data are from year 2000 runs.

The t_f is applied as software cut at 140 ns. Because of the $\sim$ 10 ns hardware veto blocking, t_s starts when the hardware veto ends, which has to be determined from experimental data.

For $\pi^+ \to \pi^0 e^+ \nu$ events, decay timing spectra are obtained (Fig. 7.1), where decay timing is defined by the variable

$$t = [(t_{\gamma_1} + t_{\gamma_2})/2] - t_{dg}, \tag{7.2}$$

where t_{γ_1} and t_{γ_2} are the TDC values of two neutral CsI calorimeter showers that are reconstructed from π^0 decay and t_{dg} is the time of the degrader signal.

The timing spectrum in Figure 7.1 can be described by the following equations:

$$N(t) = \int_{t_s}^{\infty} f(t')e^{-\frac{(t'-t)^2}{2s_t^2}}dt', \tag{7.3}$$

and

$$f(t') = \begin{cases} 0 & \text{if } t' < t_s, \\ e^{(a_0 - t'/\tau_\pi^+)} & \text{if } t' > t_s, \end{cases}$$

which takes into account the hardware veto and timing resolution. a_0 is a fitting parameter which is not our concern here.

7.1.1 pileup correction $\mathbf{f_p}$

The other factor that plays a role in shaping the experimental timing spectra is pileup events. Since the timing of a particle is registered with respect to the closet degrader event, the timing registered in the CsI may be assigned to a π^+ which is not the decaying π^+. This will modify the theoretical decay time. This pile-up effect depends on the rate of the π^+ beam and can be calculated, as shown in Figure 7.2

The center exponential line denotes the decay of the π^+ that starts the π^+ gate, which is also at the time zero, the left and the right lines are pile-up π^+'s that stopped before and after time zero. The experimental timing spectrum is the sum of all these contributions.

If the π^+ beam rate is r, then the probability that there is a π^+ at any beam packet is $\eta = r \times 19.750\,\text{ns}$. The contributions to the timing spectrum from π^+ at

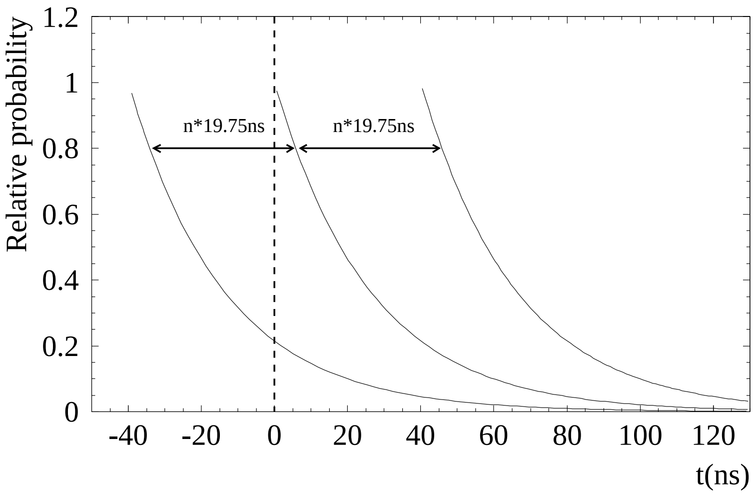

Figure 7.2: Illustration of pile-up events.

time zero and a pile-up π^+ coming at $n \times 19.750\,$ns after time zero are:

$$f(t) = \begin{cases} \left(\frac{1}{\tau}e^{-t/\tau} + \eta\frac{1}{\tau}e^{-t/\tau}e^{-(t+19.750n)/\tau} + \eta\frac{1}{\tau}e^{-(t+19.750n)/\tau}e^{-t/\tau}\right) \times & \\ \times\theta(19.750n - t) & t < 19.750n \\ \left((1-\eta)\,\frac{1}{\tau}e^{-t/\tau} + \eta\frac{1}{\tau}e^{-t/\tau}e^{-(t+19.750n)/\tau} + \eta\frac{1}{\tau}e^{-(t+19.750n)/\tau}e^{-t/\tau}\right) \times & \\ \theta(t - 19.750n) & t > 19.750n \end{cases} \tag{7.4}$$

where $\theta(t)$ is the step function.

In each of the above equations, the first term is the contribution from π^+'s stopping at time zero, the second term originates from π^+'s that stopped at zero, decayed at time $t + n \times 19.750\,$ns and registered with respect to the degrader signal from pile-up

π^+'s, the third term is caused by the pileup π^+'s.

We consider only the first order correction in which only one pile-up π^+ occurs. By summing over the index n, one can get:

$$f(t) = \frac{1}{\tau} e^{-t/\tau} \left(1 - \sum_{n=1}^{\infty} \eta\theta\,(t - 19.750n) + 2\eta \sum_{n=1}^{\infty} \eta e^{-(t+19.750n)/\tau}\right). \tag{7.5}$$

With a similar analysis, the contribution of pileup π^+'s before time zero is

$$f(t) = \frac{1}{\tau} e^{-t/\tau} \left(1 + 2\eta \sum_{n=1}^{\infty} \eta e^{-(t+19.750n)/\tau} - \eta \sum_{n=1}^{\infty} e^{-19.750n/\tau}\right). \tag{7.6}$$

The summation without the step function can be calculated right away. The final result of effects of pileup to first order, if written in the form:

$$f(t) = \frac{1}{\tau} e^{-t/\tau} \times (1 + f_p), \tag{7.7}$$

then is

$$f_p = -\eta \sum_{n=1}^{\infty} \theta\,(t - 19.750n) + \left(4\eta e^{-t/\tau} - \eta\right) \frac{e^{-19.750}/\tau}{1 - \frac{-19.750}{\tau}}. \tag{7.8}$$

A least-square MINUIT fit of the $\pi^+ \to \pi^0 e^+ \nu$ decay timing with Equation 7.3 modified by Equation 7.8 at a rate equal to 10^6/s, leaving 4 free parameters—t_s, τ_{π^+}, s_t, a_0, gives:

$$\tau_{\pi^+} = 26.02 \pm 0.21\,\mathrm{ns}, \tag{7.9}$$

$$t_s = 7.892 \pm 0.041\,\mathrm{ns}, \tag{7.10}$$

$$s_t = 0.956 \pm 0.042\,\mathrm{ns}. \tag{7.11}$$

The uncertainty on τ_{π^+} translates to $\pm 200\,\mathrm{k/s}$ in beam rate.

Substituting t_s, s_t and pion life time $\tau_{\pi^+} = 26.03\,\mathrm{ns}$ into Equation 7.1, one gets the gate fraction equal to 0.7343 ± 0.0011 for year 2000 data. The alternative way to determine the uncertainty on t_s is to fix the rate obtained by the method described in chapter 5, and compare the t_s's obtained by fixing τ_{π^+} and by releasing τ_{π^+}. The uncertainty on t_s thus obtained is 0.08 ns for year 2000 which translates to 0.002 uncertainty on acceptance. Results are summarized in Table 7.1.

Table 7.1: $\pi\beta$ gate fraction

year	t_s(ns)	$g_{\pi\beta}$
2000	7.892 ± 0.08	0.7343 ± 0.0022
2001	6.15 ± 0.10	0.7856 ± 0.0030

Due to a relatively small number of $\pi\beta$ events from year 1999 data, this method was not applied to data from 1999. Instead, a software cut on timing was used to register events after 10 ns—essentially putting the t_s at 10 ns.

7.2 $\pi^+ \to \mathbf{e}^+\nu$ gate fraction $\mathbf{g_{\pi 2e}}$

To determine the gate fraction for $\pi^+ \to e^+\nu$, we need first to determine t_0, or the π^+ stop time recorded by $\pi 2e$ trigger[1]. We use prompt events and the known cyclotron frequency t_{rf} to achieve this. From the same data set used to extract $\pi 2e$ events (see chapter 5), we applied the cuts to get as many prompt events as we can

[1]Same thing had been done for $\pi\beta$ trigger too. In fact, the offline timing offset was determined with $\pi\beta$ trigger.

and plot $(t_e - t_{dg})$ — CsI timing minus degrader timing — as shown in Figure 7.3. We fit timing line-shapes due to prompt events with a Gaussian function and extract timing peak positions. A least-square MINUIT fit of the extracted timings of the 7 beam bursts with t_{rf} left as a free parameter gives (Figure 7.3):

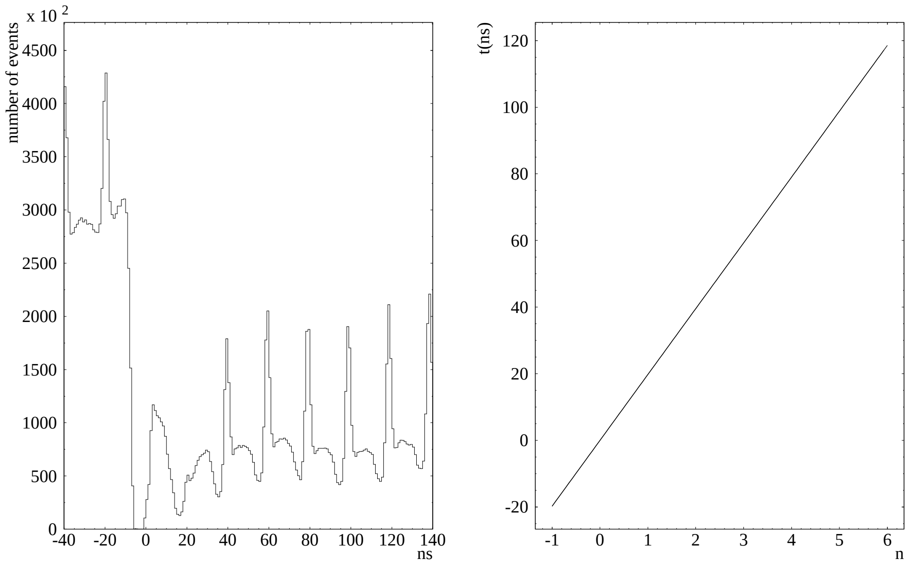

Figure 7.3: Prompt events registered through $\pi 2e$ (one arm) trigger (left panel) and prompt events timing *vs.* beam packets number (right panel). The right panel is fitted with function $t = 19.750\, n + t_0$. The fitting function has values only at n = integer. The solid line illustrates the interpolation of n = 0.

$$t_0 = 0.0025 \pm 0.0012\,\text{ns}, \quad \text{and} \quad t_{rf} = 19.760 \pm 0.0003\,\text{ns}. \tag{7.12}$$

The PSI accelerator frequency is 50.63280(4) MHz, and the phase stability of the primary quartz oscillator is better than 0.01°. This stability translates to the time interval between pulses of 19.750 ns with $\Delta t_{rf} = 0.0028\,\%$. The beam bunch width is $\simeq 1$ ns.

Using the same input data and fixing the t_{rf} at 19.750 ns gives:

$$t_0 = 0.0425 \pm 0.00077\,\mathrm{ns}. \tag{7.13}$$

The difference of t_0 from the previous results is 0.040 ns. The difference can be attributed to (i) the nonlinearity of the FASTBUS TDC scale, or (ii) statistical error.

If we take the difference of $\delta t_0 = 0.040\,\mathrm{ns}$ as our accuracy in setting the timing scale, the major pion gate contribution to the systematic uncertainty is equal to $\delta t_0/\tau_\pi$ and is:

$$\Delta g_{\pi 2e}/g_{\pi 2e} \simeq 0.15\,\%$$

The gate fraction is then equal to 0.6131 ± 0.0009.

Results are summarized in Table 7.2

Table 7.2: $\pi 2e$ gate fraction (10–70 ns)

Year	t_0(ns)	$g_{\pi 2e}$
1999	0.065 ± 0.012	0.6146 (3)
2000	0.003 ± 0.040	0.6131 (9)
2001	0.006 ± 0.010	0.6131 (3)

7.3 Plastic veto, MWPC1 and MWPC2 efficiencies

Since our cuts used in analyzing data utilized signals from MWPCs and plastic vetoes, the efficiencies of these detectors in response to positrons need to be measured. The efficiency of one detector is determined by the other two. Efficiencies of these counters for detecting positrons are determined by counting positrons that are missed by one detector while two others register them. The requirement of only one track is applied to limit the accidental coincidences. The efficiency calculation for inner chamber (chamber 1) (similar for chamber 2 and PV) is formulated as

$$\mathrm{e}_{\mathrm{MWPC}_1} = \frac{\mathrm{N}\left(\mathrm{LT} \cdot \mathrm{MWPC}_1 \cdot \mathrm{MWPC}_2 \cdot \mathrm{PV} \cdot \mathrm{CsI}\right)}{\mathrm{N}\left(\mathrm{LT} \cdot \mathrm{MWPC}_2 \cdot \mathrm{PV} \cdot \mathrm{CsI}\right)}, \tag{7.14}$$

where the N's represent the number of Michel events for which all the detectors in the parentheses register coincident hits above the discriminator threshold. The CsI calorimeter signal is discriminated with the Low Threshold (LT) level, while the window cut on the PV pulse-height spectrum selects the MIP events. This calculation is done for each run and then mean efficiencies weighted by the numbers of $\pi^+ \to e^+\nu$ decays are calculated.

7.4 Other factors that canceled out when normalizing to $\pi^+ \to \mathrm{e}^+\nu$

Number of π^+gates. Since we record only decays from a single pion gate while the scaler counts any pion gate continuously, if there is more than one pion gate during one event cycle, only one should be counted. By inspecting the number of pion gates for each event, the probability that more than one gate occurred is obtained. This probability is equal to the percentage of total counted gates that should be excluded when calculating the branching ratio.

π^+ **decay probability.** Probability of π^+'s to register pistop signal and decay instead of undergoing hadronic interaction. The percentage can be obtained from GEANT simulation and data.

π^+ **fraction in beam stop** Percentage of π^+'s in pistops after excluding beam contamination by μ's and e^+'s. This value is obtained by observing the timing difference between degrader and beam counters, as illustrated in Figure 7.4. μ's and e^+'s come earlier than π^+'s.

Detector live fraction Computer 'live' time, Measured by ratio of accepted (processed) triggers and generated (raw) triggers.

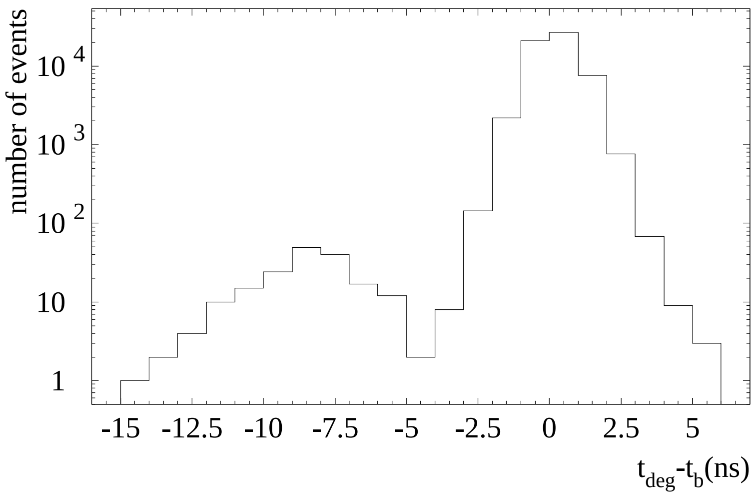

Figure 7.4: Degrader timing and beam counter timing difference. The degrader timing and the beam counter timing are aligned according to the π^+ signal, thus μ's and e^+'s come ahead of π^+'s.

Chapter 8

$\pi^+ \to \pi^0 e^+ \nu$ branching ratio and conclusions

The results from all preceding sections are summarized in Table 8.1.

The $\pi^+ \to \pi^0 e^+ \nu$ branching ratio is calculated using:

$$\begin{aligned} \Gamma_{\pi\beta} &= \frac{\mathrm{N}_{\pi\beta}\Gamma_{\pi 2\mathrm{e}}}{\mathrm{N}_{\pi 2\mathrm{e}}} \\ &= \frac{1}{\Gamma_{\pi 2\mathrm{e}}} \cdot \frac{\mathrm{N}_{\pi\beta}}{\mathrm{g}_{\pi\beta}\mathrm{A}_{\pi\beta}\Gamma_{\pi^0}} \cdot \frac{\mathrm{g}_{\pi 2\mathrm{e}}\mathrm{A}_{\pi 2\mathrm{e}}\mathrm{e}_{\mathrm{pv}}\mathrm{e}_{\mathrm{ch1}}\mathrm{e}_{\mathrm{ch2}}\Gamma_{\pi 2\mathrm{e}}}{20\mathrm{N}_{\pi 2\mathrm{e}}} \end{aligned} \tag{8.1}$$

in which 20 is a software prescaling factor to cut the dataset to a manageable size.

The $\pi^+ \to \pi^0 e^+ \nu$ branching ratio thus obtained with weighted mean is:

$$\Gamma_{\pi\beta} = (1.032 \pm 0.004\,(\mathrm{stat.}) \pm 0.005\,(\mathrm{sys.})) \times 10^{-8} \tag{8.2}$$

which represents a sixfold improvement in accuracy over the most precise previous measurement [6]. Alternatively, the normalization can be tied to the most precise

Table 8.1: Variables for $\pi^+ \to \pi^0 e^+ \nu$ branching ratio calculation

	1999[1]	2000	2001	weighted mean	Remarks
$N_{\pi\beta}$	8467 ± 92	28130 ± 168	27450 ± 166	64047 ± 253	Number of $\pi^+ \to \pi^0 e^+ \nu$ events, table 4.1
$g_{\pi\beta}$	0.674 (2)	0.734 (2)	0.786 (3)	0.748 (2)	$\pi^+ \to \pi^0 e^+ \nu$ gate fraction, table 7.1
$A_{\pi\beta}$	0.6657 (6)	0.6594 (7)	0.6623 (7)	0.6615 (7)	$\pi^+ \to \pi^0 e^+ \nu$ acceptance,table 6.3
Γ_{π^0}		0.9880 (3)			$\pi^0 \to \gamma\gamma$ branching ratio
$N_{\pi e\nu} (\times 10^7)$	0.4365 (3)	1.377 (2)	1.247 (2)	3.065 (4)	$\pi^+ \to e^+ \nu$ events, table 5.1
$g_{\pi e\nu}$	0.6146 (3)	0.6131 (9)	0.6131 (3)	0.6133 (6)	$\pi^+ \to e^+ \nu$ gate fraction, table 7.2
$A_{\pi e\nu}$	0.7040 (5)	0.7031 (6)	0.7039 (2)	0.7035 (4)	$\pi^+ \to e^+ \nu$ acceptance,table 6.3
e_{pv}	0.9948 (1)	0.9890 (1)	0.9839 (1)	0.9876 (1)	Plastic veto efficiency
e_{ch1}	0.9049 (1)	0.9454 (1)	0.9379 (1)	0.9372 (1)	Chamber 1 efficiency
e_{ch2}	0.9865 (1)	0.9792 (1)	0.9745 (1)	0.9781 (1)	Chamber 2 efficiency
$\Gamma_{\pi e\nu}$		$1.230\,(4) \times 10^{-4}$			$\pi^+ \to e^+ \nu$ branching ratio
$\Gamma_{\pi\beta} (\times 10^{-8})$	1.034 ± 0.012	1.036 ± 0.008	1.029 ± 0.008	1.032 ± 0.006	$\pi^+ \to \pi^0 e^+ \nu$ branching ratio

[1] Number of events and $g_{\pi\beta}$ for 1999 data was from 10 ns to 150 ns.

theoretical calculation $\Gamma_{\pi 2e} = (1.2352 \pm 0.0005) \times 10^{-4}$ [38] which would increase the extracted $\Gamma_{\pi\beta}$ by 0.4% to 1.036×10^{-8}.

The resulting $\pi\beta$ decay branching ratio is in good agreement with the theoretical predictions of the electroweak SM and CVC using the current PDG recommended value of V_{ud}:

$$\Gamma_{\pi\beta}^{SM} = (1.038 - 1.041) \times 10^{-8} \text{ 90\% C.L.}$$

and represents the most accurate test of CVC and Cabibbo universality in a meson to date. Our result confirms the validity of the radiative corrections for the process at the level of 5σ quoted above. since, excluding loop corrections, the SM would predict

$$\Gamma_{\pi\beta}^{excl.rad.corr.} = (1.005 - 1.008) \times 10^{-8} \text{ 90\% C.L.}$$

Using our result, Eq. 8.2, we can calculate a new value of V_{ud} from pion beta decay.

From Eq. 2.10 and Eq. 2.18,

$$V_{ud} = 0.9715 \pm 0.0029, \tag{8.3}$$

and the unitarity equation becomes

$$|V_{ud}|^2 + |V_{us}|^2 + |V_{ub}|^2 = 0.9920 \pm 0.0060, \tag{8.4}$$

which is in excellent agreement with Standard Model predictions.

Plans for improved accuracy

In addition to ADC and TDC signals, signals from the beam counters (AT, BC, AD) were all digitized using the digitizer system specifically designed for our experiment [39]. In addition, since 2000, signals from all channels were digitized. The analysis of these data are underway and the precision of $\pi\beta$ branching ratio will be further improved once this analysis is done. The second phase of this experiment is to measure the $\pi 2e$ branching ratio to a higher precision. This is also under planning.

Appendix A

Selection Function for π2e decay

Following kumac codes were used as the selection functon to calculate the $\pi^+ \to e^+\nu$ acceptance. The simulation was done in GEANT Monte Carlo with proper π^+ distribution for each year. The PV energy and CsI energy calibrations were also adjusted acoordingly. Simulation results were written into a .rz file. This code utilizes that .rz file.

```
C pienu
      REAL FUNCTION discri()
      REAL
     +IR       ,TB       ,IP1      ,IP2      ,IP3      ,X0       ,
     +Y0       ,Z0       ,PX1      ,PY1      ,PZ1      ,T1       ,
     +PX2      ,PY2      ,PZ2      ,T2       ,PX3      ,PY3      ,
     +PZ3      ,T3       ,ETAR     ,EDGD     ,PV01     ,PV02     ,
     +PV03     ,PV04     ,PV05     ,PV06     ,PV07     ,PV08     ,
     +PV09     ,PV10     ,PV11     ,PV12     ,PV13     ,PV14     ,
     +PV15     ,PV16     ,PV17     ,PV18     ,PV19     ,PV20     ,
     +DEPV     ,MWX1     ,MWX2     ,MWY1     ,MWY2     ,MWZ1     ,
     +MWZ2     ,EC1      ,EC2      ,EC3      ,T12      ,T13      ,
     +T23      ,S12      ,S13      ,S23      ,PSQ      ,PC1      ,
     +PC2      ,PC3      ,LAM      ,IB       ,SDP      ,SDM      ,
```

```
+TE1     ,TE2     ,A10     ,A11     ,A12     ,A13     ,
+A14     ,A15     ,A16     ,A17     ,A18     ,A19     ,
+A20     ,A21     ,A22     ,A23     ,A24     ,A25     ,
+A26     ,A27     ,A28     ,A9     ,A30     ,A31     ,
+A32     ,A33     ,A34     ,A35     ,A36     ,A37     ,
+A38     ,A39     ,A40     ,A41     ,A42     ,A43     ,
+A44     ,A45     ,A46     ,A47     ,A48     ,A49     ,
+A50     ,TH1     ,PH1     ,TH2     ,PH2     ,TH3     ,
+PH3     ,B07     ,B08     ,B09     ,B10     ,B11     ,
+B12     ,B13     ,B14     ,B15     ,B16     ,B17     ,
+B18     ,B19     ,B20     ,B21     ,B22     ,B23     ,
+B24     ,B25     ,B26     ,B27     ,B28     ,B29     ,
+B30     ,B31     ,B32     ,B33     ,B34     ,B35     ,
+B36     ,B37     ,B38     ,B39     ,B40     ,B41     ,
+B42     ,B43     ,B44     ,B45     ,B46     ,B47     ,
+B48     ,B49     ,B50     ,C01     ,C02     ,C03     ,
+C04     ,C05     ,C06     ,C07     ,C08     ,C09     ,
+C10     ,C11     ,C12     ,C13     ,C14     ,C15     ,
+C16     ,C17     ,C18     ,C19     ,C20     ,C21     ,
+C22     ,C23     ,C24     ,C25     ,C26     ,C27     ,
+C28     ,C29     ,C30     ,C31     ,C32     ,C33     ,
+C34     ,C35     ,C36     ,C37     ,C38     ,C39     ,
+C40     ,C41     ,C42     ,C43     ,C44     ,C45     ,
+C46     ,C47     ,C48     ,C49     ,C50     ,D01     ,
+D02     ,D03     ,D04     ,D05     ,D06     ,D07     ,
+D08     ,D09     ,D10     ,D11     ,D12     ,D13     ,
+D14     ,D15     ,D16     ,D17     ,D18     ,D19     ,
+D20     ,D21     ,D22     ,D23     ,D24     ,D25     ,
+D26     ,D27     ,D28     ,D29     ,D30     ,D31     ,
+D32     ,D33     ,D34     ,D35     ,D36     ,D37     ,
+D38     ,D39     ,D40     ,H01     ,H02     ,H03     ,
+H04     ,H05     ,H06     ,H07     ,H08     ,H09     ,
+H10     ,H11     ,H12     ,H13     ,H14     ,H15     ,
+H16     ,H17     ,H18     ,H19     ,H20     ,V01     ,
+V02     ,V03     ,V04     ,V05     ,V06     ,V07     ,
+V08     ,V09     ,V10     ,V11     ,V12     ,V13     ,
+V14     ,V15     ,V16     ,V17     ,V18     ,V19     ,
+V20     ,ECAL    ,ECAV    ,CVFR    ,CVBA    ,CVTO    ,
+CVSL    ,CVSR    ,ECVE    ,TTAR    ,TDGD    ,TMPV    ,
+TMMW    ,TCALO   ,TCALOVET,TCOSMV  ,WT      ,SQME    ,
+RA      ,NCL     ,NSCL    ,NCLH    ,NSCH    ,THT12   ,
```

```
     +HT7     ,HT8     ,HT11    ,WC      ,NH1     ,NH2     ,
     +DH1     ,DH2     ,TR      ,PI0     ,NEU     ,GAM     ,
     +DEG1    ,DEG2    ,REG1    ,REG2    ,SQM1    ,SQM2    ,
     +SQM3    ,THTC    ,LT7     ,LT8     ,LT11    ,TDC1    ,
     +TDC2    ,SEED1   ,SEED2   ,CMAX    ,ENAI    ,ENAV    ,
     +TNAI    ,TNAV    ,NPV
*
      LOGICAL         CHAIN
      CHARACTER*128   CFILE
*
      COMMON /PAWCHN/ CHAIN, NCHEVT, ICHEVT
      COMMON /PAWCHC/ CFILE
*
      COMMON/PAWIDN/IDNEVT,OBS(13),
     +IR      ,TB      ,IP1     ,IP2     ,IP3     ,X0      ,
     +Y0      ,Z0      ,PX1     ,PY1     ,PZ1     ,T1      ,
     +PX2     ,PY2     ,PZ2     ,T2      ,PX3     ,PY3     ,
     +PZ3     ,T3      ,ETAR    ,EDGD    ,PV01    ,PV02    ,
     +PV03    ,PV04    ,PV05    ,PV06    ,PV07    ,PV08    ,
     +PV09    ,PV10    ,PV11    ,PV12    ,PV13    ,PV14    ,
     +PV15    ,PV16    ,PV17    ,PV18    ,PV19    ,PV20    ,
     +DEPV    ,MWX1    ,MWX2    ,MWY1    ,MWY2    ,MWZ1    ,
     +MWZ2    ,EC1     ,EC2     ,EC3     ,T12     ,T13     ,
     +T23     ,S12     ,S13     ,S23     ,PSQ     ,PC1     ,
     +PC2     ,PC3     ,LAM     ,IB      ,SDP     ,SDM     ,
     +TE1     ,TE2     ,A10     ,A11     ,A12     ,A13     ,
     +A14     ,A15     ,A16     ,A17     ,A18     ,A19     ,
     +A20     ,A21     ,A22     ,A23     ,A24     ,A25     ,
     +A26     ,A27     ,A28     ,A29     ,A30     ,A31     ,
     +A32     ,A33     ,A34     ,A35     ,A36     ,A37     ,
     +A38     ,A39     ,A40     ,A41     ,A42     ,A43     ,
     +A44     ,A45     ,A46     ,A47     ,A48     ,A49     ,
     +A50     ,TH1     ,PH1     ,TH2     ,PH2     ,TH3     ,
     +PH3     ,B07     ,B08     ,B09     ,B10     ,B11     ,
     +B12     ,B13     ,B14     ,B15     ,B16     ,B17     ,
     +B18     ,B19     ,B20     ,B21     ,B22     ,B23     ,
     +B24     ,B25     ,B26     ,B27     ,B28     ,B29     ,
     +B30     ,B31     ,B32     ,B33     ,B34     ,B35     ,
     +B36     ,B37     ,B38     ,B39     ,B40     ,B41     ,
     +B42     ,B43     ,B44     ,B45     ,B46     ,B47     ,
     +B48     ,B49     ,B50     ,C01     ,C02     ,C03     ,
```

```
     +C04     ,C05     ,C06     ,C07     ,C08     ,C09     ,
     +C10     ,C11     ,C12     ,C13     ,C14     ,C15     ,
     +C16     ,C17     ,C18     ,C19     ,C20     ,C21     ,
     +C22     ,C23     ,C24     ,C25     ,C26     ,C27     ,
     +C28     ,C29     ,C30     ,C31     ,C32     ,C33     ,
     +C34     ,C35     ,C36     ,C37     ,C38     ,C39     ,
     +C40     ,C41     ,C42     ,C43     ,C44     ,C45     ,
     +C46     ,C47     ,C48     ,C49     ,C50     ,D01     ,
     +D02     ,D03     ,D04     ,D05     ,D06     ,D07     ,
     +D08     ,D09     ,D10     ,D11     ,D12     ,D13     ,
     +D14     ,D15     ,D16     ,D17     ,D18     ,D19     ,
     +D20     ,D21     ,D22     ,D23     ,D24     ,D25     ,
     +D26     ,D27     ,D28     ,D29     ,D30     ,D31     ,
     +D32     ,D33     ,D34     ,D35     ,D36     ,D37     ,
     +D38     ,D39     ,D40     ,H01     ,H02     ,H03     ,
     +H04     ,H05     ,H06     ,H07     ,H08     ,H09     ,
     +H10     ,H11     ,H12     ,H13     ,H14     ,H15     ,
     +H16     ,H17     ,H18     ,H19     ,H20     ,V01     ,
     +V02     ,V03     ,V04     ,V05     ,V06     ,V07     ,
     +V08     ,V09     ,V10     ,V11     ,V12     ,V13     ,
     +V14     ,V15     ,V16     ,V17     ,V18     ,V19     ,
     +V20     ,ECAL    ,ECAV    ,CVFR    ,CVBA    ,CVTO    ,
     +CVSL    ,CVSR    ,ECVE    ,TTAR    ,TDGD    ,TMPV    ,
     +TMMW    ,TCALO   ,TCALOVET,TCOSMV  ,WT      ,SQME    ,
     +RA      ,NCL     ,NSCL    ,NCLH    ,NSCH    ,THT12   ,
     +HT7     ,HT8     ,HT11    ,WC      ,NH1     ,NH2     ,
     +DH1     ,DH2     ,TR      ,PI0     ,NEU     ,GAM     ,
     +DEG1    ,DEG2    ,REG1    ,REG2    ,SQM1    ,SQM2    ,
     +SQM3    ,THTC    ,LT7     ,LT8     ,LT11    ,TDC1    ,
     +TDC2    ,SEED1   ,SEED2   ,CMAX    ,ENAI    ,ENAV    ,
     +TNAI    ,TNAV    ,NPV
*

      vector t(1)
      vector a(1)
      vector acc(1)
      vector pv(20)
      vector ec(3)
      vector index(3)
      vector phi(3)
      vector trak_epv(3)
```

```
      vector id(3)
C 2000 pv e adjustment
      fac = 1.0
C 2000 csi gain adj
      fac_csi=1.005

      id(1)=-1
      id(2)=-1
      id(3)=-1
      trak_epv(1)=-1000.
      trak_epv(2)=-1000.
      trak_epv(3)=-1000.
      index(1)=-1
      index(2)=-1
      index(3)=-1
      ec(1)=ec1*fac_csi
      ec(2)=ec2*fac_csi
      ec(3)=ec3*fac_csi
      phi(1)=ph1
      phi(2)=ph2
      phi(3)=ph3

      pv(1)=pv01*fac
      pv(2)=pv02*fac
      pv(3)=pv03*fac
      pv(4)=pv04*fac
      pv(5)=pv05*fac
      pv(6)=pv06*fac
      pv(7)=pv07*fac
      pv(8)=pv08*fac
      pv(9)=pv09*fac
      pv(10)=pv10*fac
      pv(11)=pv11*fac
      pv(12)=pv12*fac
      pv(13)=pv13*fac
      pv(14)=pv14*fac
      pv(15)=pv15*fac
      pv(16)=pv16*fac
      pv(17)=pv17*fac
      pv(18)=pv18*fac
      pv(19)=pv19*fac
```

```
      pv(20)=pv20*fac

C find pv which registers largest energy
      pc1_index=-1
      do i=1,20
       if(pv(i) .eq. pc1) ipc1_index=i
      enddo

C find PV for each clump
      min_angle=180.
      do i=1,3
       do j=1,20
        tmp=abs(phi(i)-(j*360./20.-9.))
         if (tmp.gt.180.)tmp=360.-tmp
         if (tmp<min_angle) then
            min_angle=tmp
            index(i)=j
         endif
       enddo
      enddo
      do i=1,3
         k=index(i)
         if(k.gt.1 .and. k.lt.20) then
            trak_epv(i)=pv(k)
            if(trak_epv(i)<pv(k-1))trak_epv(i)=pv(k-1)
            if(trak_epv(i)<pv(k+1))trak_epv(i)=pv(k+1)
         endif
         if(k.eq.1) then
            trak_epv(i) = pv(k)
            if(trak_epv(i)<pv(k+1)) trak_epv(i)=pv(k+1)
            if(trak_epv(i)<pv(20)) trak_epv(i)=pv(20)
         endif
         if(k.eq.20) then
            trak_epv(i) = pv(k)
            if(trak_epv(i)<pv(1))trak_epv(i)=pv(1)
            if(trak_epv(i)<pv(k-1))trak_epv(i)=pv(k-1)
         endif
      enddo

C positron discriminator
      do i=1,3
```

```
        if(trak_epv(i).gt.0.2*exp(-0.007*(trak_epv(i)+ec(i))) .and.
     +   trak_epv(i).le.2.3*exp(-0.007*(trak_epv(i)+ec(i)))) then
           id(i)=1
        endif
        call hf1(13,float(id(i)),1.)
      enddo

C clump energy closet to 68.0(as in analyzer)
      best_pienu=-1000.0
      ip = -1
      do i=1,3
C         id(i)=1
         if((abs(ec(i)+trak_epv(i)-68.0).lt.abs(best_pienu-68.0))
     +     .and. (id(i).eq.1) .and.ec(i).gt.5.) then
            best_pienu=ec(i)+trak_epv(i)
            ip=i
         endif
      enddo

C initialization
      if(IDNEVT.eq.1) then
            a(1)=0.
            t(1)=0.

            acc(1)=0.
       endif

      t(1) = t(1)+WT*SQME

C cuts similar to ones used in analyzer, ht7 is pienuHI trigger

      IF(ip.gt.0) then
         IF((HT7.EQ.1) .and. (ecal.lt.200).and.(npv.gt.0).and.
     +        (ec(ip)*csi_e_norm.gt.51.).and.
     +        (ec(ip)*csi_e_norm.lt.74)) THEN
            discri=WT*SQME
            a(1) = a(1)+WT*SQME
C csi_e_norm factor to make energy scale fit
            call hf1(801, ec(ip)*csi_e_norm, 1.)
            call hf1(800300,trak_epv(ip), 1.)
          ELSE
```

```
            discri=0.
         ENDIF
      endif
C acc(1) contains acceptance
      acc(1)=a(1)/t(1)
      END
```

Appendix B

Selection Function for $\pi\beta$ decay

Following FORTRAN code was used as selection function in PAW to calculate the $\pi\beta$ decay acceptance.

```
C pibeta
      REAL FUNCTION discri()
      REAL
     +IR      ,TB      ,IP1     ,IP2     ,IP3     ,X0      ,
     +Y0      ,Z0      ,PX1     ,PY1     ,PZ1     ,T1      ,
     +PX2     ,PY2     ,PZ2     ,T2      ,PX3     ,PY3     ,
     +PZ3     ,T3      ,ETAR    ,EDGD    ,PV01    ,PV02    ,
     +PV03    ,PV04    ,PV05    ,PV06    ,PV07    ,PV08    ,
     +PV09    ,PV10    ,PV11    ,PV12    ,PV13    ,PV14    ,
     +PV15    ,PV16    ,PV17    ,PV18    ,PV19    ,PV20    ,
     +DEPV    ,MWX1    ,MWX2    ,MWY1    ,MWY2    ,MWZ1    ,
     +MWZ2    ,EC1     ,EC2     ,EC3     ,T12     ,T13     ,
     +T23     ,S12     ,S13     ,S23     ,PSQ     ,PC1     ,
     +PC2     ,PC3     ,LAM     ,IB      ,SDP     ,SDM     ,
     +TE1     ,TE2     ,A10     ,A11     ,A12     ,A13     ,
     +A14     ,A15     ,A16     ,A17     ,A18     ,A19     ,
     +A20     ,A21     ,A22     ,A23     ,A24     ,A25     ,
     +A26     ,A27     ,A28     ,A29     ,A30     ,A31     ,
     +A32     ,A33     ,A34     ,A35     ,A36     ,A37     ,
     +A38     ,A39     ,A40     ,A41     ,A42     ,A43     ,
     +A44     ,A45     ,A46     ,A47     ,A48     ,A49     ,
     +A50     ,TH1     ,PH1     ,TH2     ,PH2     ,TH3     ,
     +PH3     ,B07     ,B08     ,B09     ,B10     ,B11     ,
     +B12     ,B13     ,B14     ,B15     ,B16     ,B17     ,
```

```
     +B18     ,B19     ,B20     ,B21     ,B22     ,B23      ,
     +B24     ,B25     ,B26     ,B27     ,B28     ,B29      ,
     +B30     ,B31     ,B32     ,B33     ,B34     ,B35      ,
     +B36     ,B37     ,B38     ,B39     ,B40     ,B41      ,
     +B42     ,B43     ,B44     ,B45     ,B46     ,B47      ,
     +B48     ,B49     ,B50     ,C01     ,C02     ,C03      ,
     +C04     ,C05     ,C06     ,C07     ,C08     ,C09      ,
     +C10     ,C11     ,C12     ,C13     ,C14     ,C15      ,
     +C16     ,C17     ,C18     ,C19     ,C20     ,C21      ,
     +C22     ,C23     ,C24     ,C25     ,C26     ,C27      ,
     +C28     ,C29     ,C30     ,C31     ,C32     ,C33      ,
     +C34     ,C35     ,C36     ,C37     ,C38     ,C39      ,
     +C40     ,C41     ,C42     ,C43     ,C44     ,C45      ,
     +C46     ,C47     ,C48     ,C49     ,C50     ,D01      ,
     +D02     ,D03     ,D04     ,D05     ,D06     ,D07      ,
     +D08     ,D09     ,D10     ,D11     ,D12     ,D13      ,
     +D14     ,D15     ,D16     ,D17     ,D18     ,D19      ,
     +D20     ,D21     ,D22     ,D23     ,D24     ,D25      ,
     +D26     ,D27     ,D28     ,D29     ,D30     ,D31      ,
     +D32     ,D33     ,D34     ,D35     ,D36     ,D37      ,
     +D38     ,D39     ,D40     ,H01     ,H02     ,H03      ,
     +H04     ,H05     ,H06     ,H07     ,H08     ,H09      ,
     +H10     ,H11     ,H12     ,H13     ,H14     ,H15      ,
     +H16     ,H17     ,H18     ,H19     ,H20     ,V01      ,
     +V02     ,V03     ,V04     ,V05     ,V06     ,V07      ,
     +V08     ,V09     ,V10     ,V11     ,V12     ,V13      ,
     +V14     ,V15     ,V16     ,V17     ,V18     ,V19      ,
     +V20     ,ECAL    ,ECAV    ,CVFR    ,CVBA    ,CVTO     ,
     +CVSL    ,CVSR    ,ECVE    ,TTAR    ,TDGD    ,TMPV     ,
     +TMMW    ,TCALO   ,TCALOVET,TCOSMV  ,WT      ,SQME     ,
     +RA      ,NCL     ,NSCL    ,NCLH    ,NSCH    ,THT12    ,
     +HT7     ,HT8     ,HT11    ,WC      ,NH1     ,NH2      ,
     +DH1     ,DH2     ,TR      ,PI0     ,NEU     ,GAM      ,
     +DEG1    ,DEG2    ,REG1    ,REG2    ,SQM1    ,SQM2     ,
     +SQM3    ,THTC    ,LT7     ,LT8     ,LT11    ,TDC1     ,
     +TDC2    ,SEED1   ,SEED2   ,CMAX    ,ENAI    ,ENAV     ,
     +TNAI    ,TNAV    ,NPV
*
      LOGICAL         CHAIN
      CHARACTER*128   CFILE
*
```

```
      COMMON /PAWCHN/ CHAIN, NCHEVT, ICHEVT
      COMMON /PAWCHC/ CFILE
*
      COMMON/PAWIDN/IDNEVT,OBS(13),
     +IR      ,TB      ,IP1     ,IP2     ,IP3     ,X0      ,
     +Y0      ,Z0      ,PX1     ,PY1     ,PZ1     ,T1      ,
     +PX2     ,PY2     ,PZ2     ,T2      ,PX3     ,PY3     ,
     +PZ3     ,T3      ,ETAR    ,EDGD    ,PV01    ,PV02    ,
     +PV03    ,PV04    ,PV05    ,PV06    ,PV07    ,PV08    ,
     +PV09    ,PV10    ,PV11    ,PV12    ,PV13    ,PV14    ,
     +PV15    ,PV16    ,PV17    ,PV18    ,PV19    ,PV20    ,
     +DEPV    ,MWX1    ,MWX2    ,MWY1    ,MWY2    ,MWZ1    ,
     +MWZ2    ,EC1     ,EC2     ,EC3     ,T12     ,T13     ,
     +T23     ,S12     ,S13     ,S23     ,PSQ     ,PC1     ,
     +PC2     ,PC3     ,LAM     ,IB      ,SDP     ,SDM     ,
     +TE1     ,TE2     ,A10     ,A11     ,A12     ,A13     ,
     +A14     ,A15     ,A16     ,A17     ,A18     ,A19     ,
     +A20     ,A21     ,A22     ,A23     ,A24     ,A25     ,
     +A26     ,A27     ,A28     ,A29     ,A30     ,A31     ,
     +A32     ,A33     ,A34     ,A35     ,A36     ,A37     ,
     +A38     ,A39     ,A40     ,A41     ,A42     ,A43     ,
     +A44     ,A45     ,A46     ,A47     ,A48     ,A49     ,
     +A50     ,TH1     ,PH1     ,TH2     ,PH2     ,TH3     ,
     +PH3     ,B07     ,B08     ,B09     ,B10     ,B11     ,
     +B12     ,B13     ,B14     ,B15     ,B16     ,B17     ,
     +B18     ,B19     ,B20     ,B21     ,B22     ,B23     ,
     +B24     ,B25     ,B26     ,B27     ,B28     ,B29     ,
     +B30     ,B31     ,B32     ,B33     ,B34     ,B35     ,
     +B36     ,B37     ,B38     ,B39     ,B40     ,B41     ,
     +B42     ,B43     ,B44     ,B45     ,B46     ,B47     ,
     +B48     ,B49     ,B50     ,C01     ,C02     ,C03     ,
     +C04     ,C05     ,C06     ,C07     ,C08     ,C09     ,
     +C10     ,C11     ,C12     ,C13     ,C14     ,C15     ,
     +C16     ,C17     ,C18     ,C19     ,C20     ,C21     ,
     +C22     ,C23     ,C24     ,C25     ,C26     ,C27     ,
     +C28     ,C29     ,C30     ,C31     ,C32     ,C33     ,
     +C34     ,C35     ,C36     ,C37     ,C38     ,C39     ,
     +C40     ,C41     ,C42     ,C43     ,C44     ,C45     ,
     +C46     ,C47     ,C48     ,C49     ,C50     ,D01     ,
     +D02     ,D03     ,D04     ,D05     ,D06     ,D07     ,
     +D08     ,D09     ,D10     ,D11     ,D12     ,D13     ,
```

```
     +D14      ,D15      ,D16      ,D17      ,D18      ,D19      ,
     +D20      ,D21      ,D22      ,D23      ,D24      ,D25      ,
     +D26      ,D27      ,D28      ,D29      ,D30      ,D31      ,
     +D32      ,D33      ,D34      ,D35      ,D36      ,D37      ,
     +D38      ,D39      ,D40      ,H01      ,H02      ,H03      ,
     +H04      ,H05      ,H06      ,H07      ,H08      ,H09      ,
     +H10      ,H11      ,H12      ,H13      ,H14      ,H15      ,
     +H16      ,H17      ,H18      ,H19      ,H20      ,V01      ,
     +V02      ,V03      ,V04      ,V05      ,V06      ,V07      ,
     +V08      ,V09      ,V10      ,V11      ,V12      ,V13      ,
     +V14      ,V15      ,V16      ,V17      ,V18      ,V19      ,
     +V20      ,ECAL     ,ECAV     ,CVFR     ,CVBA     ,CVTO     ,
     +CVSL     ,CVSR     ,ECVE     ,TTAR     ,TDGD     ,TMPV     ,
     +TMMW     ,TCALO    ,TCALOVET,TCOSMV    ,WT       ,SQME     ,
     +RA       ,NCL      ,NSCL     ,NCLH     ,NSCH     ,THT12    ,
     +HT7      ,HT8      ,HT11     ,WC       ,NH1      ,NH2      ,
     +DH1      ,DH2      ,TR       ,PI0      ,NEU      ,GAM      ,
     +DEG1     ,DEG2     ,REG1     ,REG2     ,SQM1     ,SQM2     ,
     +SQM3     ,THTC     ,LT7      ,LT8      ,LT11     ,TDC1     ,
     +TDC2     ,SEED1    ,SEED2    ,CMAX     ,ENAI     ,ENAV     ,
     +TNAI     ,TNAV     ,NPV
*
      vector a(1)
      vector t(1)
      vector acc(1)
      vector ec(3)
      vector pv(20)
      vector id(3)
      vector index(3)
      vector th(3)
      vector phi(3)
      vector px(3)
      vector py(3)
      vector pz(3)
      vector trak_epv(3)
      vector tmp_ec(3)

      vector tntp200(4)

C initialization
      if(IDNEVT.eq.1) then
```

```
         total = 0.0
         a(1)=0.0
         t(1)=0.
         acc(1)=0.
      endif

C 2000 pv e adjustment
      fac = 1.005

      index(1)=-1
      index(2)=-1
      index(3)=-1
      th(1)=th1
      th(2)=th2
      th(3)=th3
      phi(1)=ph1
      phi(2)=ph2
      phi(3)=ph3
      id(1)=-1
      id(2)=-1
      id(3)=-1
      ec(1)=ec1
      ec(2)=ec2
      ec(3)=ec3
      phi(1)=ph1
      phi(2)=ph2
      phi(3)=ph3

      pv(1)=pv01*fac
      pv(2)=pv02*fac
      pv(3)=pv03*fac
      pv(4)=pv04*fac
      pv(5)=pv05*fac
      pv(6)=pv06*fac
      pv(7)=pv07*fac
      pv(8)=pv08*fac
      pv(9)=pv09*fac
      pv(10)=pv10*fac
      pv(11)=pv11*fac
      pv(12)=pv12*fac
      pv(13)=pv13*fac
```

```
      pv(14)=pv14*fac
      pv(15)=pv15*fac
      pv(16)=pv16*fac
      pv(17)=pv17*fac
      pv(18)=pv18*fac
      pv(19)=pv19*fac
      pv(20)=pv20*fac
      do i=1,20
         if (pv(i)<0.001)pv(i)=0.0
         if (pv(i)<0.062)pv(i)=0.0
      enddo
      PI = 3.1415926535

      total = total+wt*sqme

C sort ec1,2,3 from largest down
      clump_number_cut=0.
      do i=1,3
         tmp_ec(i)=ec(i)
      enddo
      do i=1,3
         do j=i+1,3
            if(tmp_ec(i)<tmp_ec(j))then
               tmp=tmp_ec(i)
               tmp_ec(i)=tmp_ec(j)
               tmp_ec(j)=tmp
            endif
         enddo
      enddo

C Clump number cut
      IF(tmp_ec(2).ge.4.0) clump_number_cut=2.
C ht11 is pibetaHI trigger
      if(clump_number_cut.lt.2 .or. ht11.ne.1) goto 999

C find the pv which registers largest energy
      ipc1_index=-1
      min_dif=1000.0
      do i=1,20
       if(abs(pv(i) - pc1*fac)<min_dif) then
          ipc1_index=i
```

```
          min_dif=abs(pv(i)-pc1*fac)
       endif
      enddo

C component of unit momentum, or direction of momentum
      do i=1,3
       px(i)=sin(PI/180.*th(i))*cos(PI/180.*phi(i))
       py(i)=sin(PI/180.*th(i))*sin(PI/180.*phi(i))
       pz(i)=cos(PI/180.*th(i))
      enddo

C assign pv to clumps
      min_angle=180.
      do i=1,3
       do j=1,20
        tmp=abs(phi(i)-(j*360./20.-9.))
         if (tmp.gt.180.)tmp=360.-tmp
         if (tmp<min_angle) then
            min_angle=tmp
            index(i)=j
         endif
       enddo
      enddo

C assign pv to track
      do i=1,3
        k=index(i)
        if(k.ge.1 .and. k.le.20) trak_epv(i)=pv(k)
      enddo

C particle ID
      do i=1,3
         if(trak_epv(i)<0.2*exp(-0.007*(trak_epv(i)+ec(i)))) id(i)=1
      enddo

C best gamma pair, using pion invariant mass
     min = 9000000.0
      i1=1
      i2=1
      do i=1,2
       do j=i+1,3
```

```
        mpi_inv = 9000000.0
        if (id(i).eq.1.and.id(j).eq.1) then
           mpi_inv=(ec(i)+ec(j))**2 -(ec(i)*px(i)+ec(j)*px(j))**2 -
     +              (ec(i)*py(i)+ec(j)*py(j))**2 -
     +              (ec(i)*pz(i)+ec(j)*pz(j))**2
           if ( abs(mpi_inv- 18216.9) < abs(min) ) then
              min = mpi_inv - 18216.9;
              i1=i;
              i2=j;
           endif
        endif
       enddo
      enddo
      mpi0=-1000.;

C angle between two gamma's
      if ( i1>1 .or. i2>1 ) then
        best_pi0 = ec(i1) + ec(i2)
         temp_tmp2 = px(i1)*px(i2)+py(i1)*py(i2)+pz(i1)*pz(i2);
         if ( abs(temp_tmp2) .le. 1.000000000000001 ) then
            temp_tmp2 = 57.29578*acos(temp_tmp2)
         else
            temp_tmp2 = -1000.0;
         endif
         mpi0 = sqrt (abs(min+18216.9));
      else
         temp_tmp2=-1000.0
         best_pi0=-1000.0
      endif


      TEC1=ec(i1)
      TEC2=ec(i2)


      tmp3=-1000.0

      IF ((TEC1+TEC2)>10.) THEN
         RATIO12 =TEC1/(TEC1+TEC2)
      ELSE
         RATIO12 = 0.
```

```
      ENDIF

C pibeta discriminator
      IF(HT11 .AND. i1+i2.gt.2.and.temp_TMP2>0) THEN
        IF(ABS(RATIO12-0.48)<0.08 .AND. temp_TMP2>(-15.*SQRT(1.-(1./0.08
     *   )*(RATIO12-0.48)*(1./0.08)*(RATIO12-0.48))+180.)) THEN
           TMP3=1.
         ELSE IF (ABS(RATIO12-0.47)<0.14 .AND. temp_TMP2>(-19.*SQRT(
     *           1.-(1./0.14)*(RATIO12-0.47)*(1./0.14)*
     *           (RATIO12-0.47))+180.)) THEN
           TMP3=2.
         ENDIF
      ENDIF

C all cuts used in analyzer
      IF(HT11.EQ.1.and.tmp3>0 .and.clump_number_cut
     +  .and.ecal<200. .and.abs(mpi0-137.)<50.) THEN
         discri=WT*SQME
         a(1) = a(1)+WT*SQME
      ELSE
         discri=0.
      ENDIF
 999  continue
      t(1)=total

C acc(1) contains acceptance
      acc(1)=a(1)/t(1)
      END
```

Appendix C

MINUIT code for $\pi\beta$ timing fit

MINUIT routine to fit $\pi\beta$ timing spectrum.

```
      PROGRAM GATE
      IMPLICIT DOUBLE PRECISION (A-H, O-Z)
      EXTERNAL FUN
      EXTERNAL FUNC
      COMMON/EXPERIM/EEXP
      DOUBLE PRECISION EEXP(300)
      INTEGER I,J,K,N

      N=300
      OPEN(UNIT=5,FILE='gate.dat',STATUS='OLD')
      OPEN(UNIT=10,FILE="pb_t01.dat",STATUS='OLD')
C      OPEN(UNIT=10,FILE="yy.dat",STATUS='OLD')
      READ(10,*)(EEXP(I),I=1,N)
      CLOSE(10)
C      CALL MINTIO(5,6,7)
      CALL MINUIT(FUNC,0)
      STOP
      END


      SUBROUTINE FUNC(NPAR,GRAD,FVAL,XVAL,IFLAG,FUTIL)

      IMPLICIT DOUBLE PRECISION (A-H,O-Z)
      EXTERNAL FUN
      EXTERNAL DGAUSS
      DOUBLE PRECISION CHISQR,TAO,X0,A1,A2,S,A,TMP,EPS,FUN,DGAUSS
```

```
      COMMON/BLOCK/TAO,X0,A1,A2,S,A
      COMMON/EXPERIM/EEXP
      COMMON/RATE/PERIOD,RATE,G
      DOUBLE PRECISION EEXP(300)
      INTEGER I,J,K,N,COUNTER
      DOUBLE PRECISION  RESULT(300),tmp1,sum,LEFT,RIGHT,PERIOD
     +                  , RATE,RESULT1(300),G
      DIMENSION XVAL(*), GRAD(*)

      RATE=0.6E6
C PERION IS IN NUMBER OF PACKETS
      PERIOD=1/(19.750e-9*RATE)
C      G=1./PERIOD
      write(*,*) "period=",period
      sum=0.0
      COUNTER=0
      TAO = XVAL(1)
      A1=XVAL(2)
      A2=280
      S=XVAL(3)
      A=XVAL(4)
      G=19.750e-9*XVAL(5)
      N=300
      EPS=0.00000000000001
      write(*,*)TAO,A1,S,A,XVAL(5)
      DO I=0,N-1
       TMP=0.0
       DO K=0,9
         X0=(DBLE(I)*10.+DBLE(K))*0.05+0.025
         if((X0-6.*S).LT.A1) THEN
            LEFT = A1
         ELSE
            LEFT = X0-6.*S
         ENDIF
         RIGHT = X0+6.*S
c DGAUSS(FUN,LEFT,RIGHT,EPS)
         tmp1=DGAUSS(FUN,LEFT,RIGHT,EPS)*(1-SSUM(X0)+
     +       (4*G*EXP(-X0/TAO)-G)*(
     +            EXP(-19.75/TAO)/(1.-EXP(-19.75/TAO))))
```

```
            TMP=TMP+tmp1

            if (tmp<0.0001) tmp=0.0
          ENDDO
         RESULT(I+1)=TMP/10.
         RESULT1(I+1)=RESULT(I+1)
         ENDDO

         CHISQR=0.0
         DO I=1,A2
            IF((I.ge.35.and.I.le.45).or.(I.ge.75.and.I.le.85).or.
     +         (I.ge.115.and.I.le.125).or.(I.ge.155.and.I.le.165).or.
     +         (I.ge.205.and.I.le.215).or.(I.ge.245.and.I.le.255)
     +         ) goto 12
               IF(EEXP(I)>0.000001) THEN
                  CHISQR=CHISQR+((EEXP(I)-RESULT(I))**2/(EEXP(I)))
                  counter = counter+1
               ENDIF

12       CONTINUE
         sum = sum+result(I)
         ENDDO
         DO I=A2+1, 300
            result(I)=0.
         enddo

         FVAL=CHISQR
         WRITE(*,*) counter,chisqr
         OPEN(unit=90,FILE='fort.90', status='unknown')
         write(90,22) result,RESULT1
22       format(F12.5)
         close(90)
         OPEN(unit=91,FILE='fort.91', status='unknown')

         close(91)
         IF(IFLAG.EQ.3) THEN
            WRITE(*,*) counter, ' channels SUM= ', sum
         ENDIF

         RETURN
```

```
      END

      DOUBLE PRECISION FUNCTION FUN(X)
      IMPLICIT NONE
      DOUBLE PRECISION TAO,X0,A1,A2,S,A,X
      COMMON/BLOCK/TAO,X0,A1,A2,S,A


      IF (X<A1 .OR. X>A2) THEN
         FUN=0.0
      ELSE
         FUN=EXP(A-X/TAO)*EXP(-(X-X0)*(X-X0)/(2*S*S))
C         fun=exp(a-x/tao)
      ENDIF
      RETURN
      END FUNCTION

      DOUBLE PRECISION FUNCTION SSUM(t)
      IMPLICIT NONE
      INTEGER N,I
C     G IS THE PROBABILITY
      COMMON/RATE/PERIOD,RATE,G
      DOUBLE PRECISION TMP,RATE,G,step
      COMMON/BLOCK/TAO,X0,A1,A2,S,A
      DOUBLE PRECISION T_RF,TAO,X0,A1,A2,S,A,PERIOD,facto,T


      N = 10
      T_RF = 19.750
      TMP=0.0
      DO I=1, N
        TMP=TMP+G*step(T-I*T_RF)
      ENDDO
      SSUM=TMP
      END FUNCTION

C     STEP FUNCITON step
      DOUBLE PRECISION FUNCTION step(X)
      IMPLICIT NONE
      DOUBLE PRECISION X,tmp
```

```
IF(X<0.) THEN
   tmp=0.0
ELSE
   tmp=1.0
ENDIF
step=tmp
END FUNCTION

DOUBLE PRECISION FUNCTION FACTO(N)
IMPLICIT NONE
INTEGER N,I
DOUBLE PRECISION TMP

TMP = 1.
DO I=1,N
   TMP = 1.*DBLE(N)*TMP
ENDDO
FACTO = TMP
END FUNCTION
```

Appendix D

Code to simulate π2e timing

C gate.F

```
      PROGRAM GATE
      IMPLICIT DOUBLE PRECISION (A-H, O-Z)
      EXTERNAL FUN
      EXTERNAL FUNC

      COMMON/EXPERIM/EXP
      REAL EXP(180),dummy(180)
      INTEGER I,J,K,N

      N=180
      OPEN(UNIT=5,FILE='gate.dat',STATUS='OLD')
      OPEN(UNIT=10,FILE="exp_dg01_e51_74.txt",STATUS='OLD')
      READ(10,*)(EXP(I),I=1,N)
      CLOSE(10)
C      CALL MINTIO(5,6,7)
      CALL MINUIT(FUNC,0)

      STOP
      END

C______________________________________________________________
      SUBROUTINE FUNC(NPAR,GRAD,FVAL,XVAL,IFLAG,FUTIL)

      IMPLICIT DOUBLE PRECISION (A-H,O-Z)
      EXTERNAL FUN
      EXTERNAL DGAUSS
```

```
COMMON/BLOCK/X0,A1,A2,S
COMMON/PARAMETER/ALP1,ALP2,ALP3,ALP4,LAMBAD_PI
COMMON/EXPERIM/EXP
DOUBLE PRECISION CHISQR,X0,A1,A2,S,TMP,EPS,FUN,DGAUSS,LEFT
DOUBLE PRECISION RIGHT,LEFT_LIMIT,RANGE,LAMBAD_PI,CHI2
REAL EXP(180)
INTEGER I,J,K,N,NN,COUNTER
DOUBLE PRECISION  RESULT(180),tmp1(3600)
DIMENSION XVAL(*), GRAD(*)

RANGE = 3.
NN = 20
LEFT_LIMIT = -40.
A2   = 140.
A1   = XVAL(1)
S    = XVAL(2)
ALP1 = XVAL(3)
ALP2 = XVAL(4)
ALP3 = XVAL(5)
ALP4 = XVAL(6)
LAMBAD_PI = 1./XVAL(7)

N=180
EPS=0.0000000001

DO I=0,N-1
 TMP=0.0
 DO K=0,NN-1
   X0 = (I*DBLE(NN)+K)/DBLE(NN) - 40.
   IF ((X0+RANGE*S)>A2) THEN
      RIGHT=A2
   ELSE
      RIGHT=X0+RANGE*S
   ENDIF
   IF ((X0-RANGE*S)<LEFT_LIMIT) THEN
      LEFT=LEFT_LIMIT
   ELSE
      LEFT=X0-RANGE*S
   ENDIF
```

```
C         tmp1(I*NN+K+1) = DGAUSS(FUN,LEFT,RIGHT,EPS)
         tmp1(I*NN+K+1) = fun(X0)

C         tmp1(I*NN+K+1) = THETA(x0)*ALP2*PHI(x0)
C         tmp1(I*NN+K+1) = sum1(x0)
         TMP = TMP+tmp1(I*NN+k+1)/DBLE(20.)

         if (tmp<0.000001) tmp=0.0
       ENDDO
      if((I+1)<11) TMP = 0.0
      if((I+1)>30 .and. I<50) TMP = 0.0
      if((I+1)>170) TMP = 0.0
      RESULT(I+1)=TMP
      ENDDO
      CHISQR=0.0
      CHI2 = 0.0
      COUNTER=0
      DO I=1,N
         if((I.ge.19.AND.I.LE.24).OR.(I.ge.58.AND.I.LE.63).OR.(I.ge.73.
     +      AND.I.LE.83).OR.(I.ge.93.AND.I.LE.103).OR.
     +      (I.ge.113.AND.I.LE.123).OR. (I.ge.133.AND.I.LE.143).OR.
     +       (I.ge.153.AND.I.LE.163)) then
            GOTO 12
         endif

         IF(EXP(I)>0.001 .AND. RESULT(I)>0.001) THEN
            COUNTER = COUNTER+1
            CHISQR=CHISQR+((EXP(I)-RESULT(I))**2/EXP(I))
            IF(I>50 .AND. I<110) THEN
               CHI2 = CHI2+((EXP(I)-RESULT(I))**2/EXP(I))
            ENDIF
         ENDIF
 12      continue
      ENDDO
      FVAL=CHISQR

      write(*,*) 'result(60)=', result(60),'exp(60)=',exp(60)
      WRITE(*,*) COUNTER, chisqr, '    ', CHI2
      OPEN(unit=90,FILE='fort.90', status='unknown')
      write(90,22) result
 22   format(F20.5)
```

```
      close(90)
      OPEN(unit=91,FILE='fort.91', status='unknown')
      write(91,22) tmp1
      close(91)
      IF(IFLAG.EQ.3) THEN
         WRITE(*,*) 'SUM1 10-70=', INTSUM1(dble(10.))
         WRITE(*,*) 'ALP1,ALP2,ALP3,ALP4==', ALP1,ALP2,ALP3,ALP4
         WRITE(*,*) 'NUMBER OF EVENTS=Alp1*0.61308+Alp3*4.058 = ',
     +              Alp1*0.61308+Alp3*4.058
      ENDIF

      RETURN
      END
CC______________________________________________________
      DOUBLE PRECISION FUNCTION FUN(X)
      IMPLICIT NONE
      EXTERNAL F
      DOUBLE PRECISION X0,A1,A2,S,X,F
      COMMON/BLOCK/X0,A1,A2,S

      IF (X0>0) THEN
         IF (X<A1 .OR. X>A2) THEN
            FUN=0.0
         ELSE
            FUN=F(X)*EXP(-(X-X0)*(X-X0)/(2*S*S))
         ENDIF
      ELSE
         FUN=F(X)*EXP(-(X-X0)*(X-X0)/(2*S*S))
      ENDIF
C      write(*,*) 'funx(',x,')=',fun
      RETURN
      END FUNCTION
CC_____________________________________________________
      DOUBLE PRECISION FUNCTION F(T)
      IMPLICIT NONE
      EXTERNAL THETA
      EXTERNAL PHI
      EXTERNAL SUM1
      EXTERNAL SUM2
      COMMON/PARAMETER/ALP1,ALP2,ALP3,ALP4,LAMBAD_PI
      DOUBLE PRECISION ALP1,ALP2,ALP3,ALP4,LAMBAD_PI,THETA,PHI,SUM1
```

```
     +                  ,SUM2,T


      F=THETA(T)*ALP1*LAMBAD_PI*EXP(-LAMBAD_PI*T)+THETA(T)*ALP2*
     +  PHI(T)+ALP3*SUM1(T)+ALP4*SUM2(T)
      RETURN
      END FUNCTION
CC_____________________________________________________
      DOUBLE PRECISION FUNCTION SUM1(T)
      IMPLICIT NONE
      EXTERNAL THETA
      COMMON/PARAMETER/ALP1,ALP2,ALP3,ALP4,LAMBAD_PI
      DOUBLE PRECISION T_RF,LAMBAD_PI,S,THETA,T
      DOUBLE PRECISION ALP1,ALP2,ALP3,ALP4
      INTEGER N

      T_RF = 19.75
C      LAMBAD_PI = 1/26.03
      S = 0.0

      DO N=-100, 10
        IF (N .EQ. 0) GOTO 10
        S = S+THETA(T-T_RF*DBLE(N)-3.0)*LAMBAD_PI*EXP(-LAMBAD_PI*
     +   (T-T_RF*DBLE(N)))
 10     CONTINUE
      ENDDO
      SUM1 = S
      RETURN
      END FUNCTION
C_______________________________________________________
      DOUBLE PRECISION FUNCTION SUM2(T)
      IMPLICIT NONE
      EXTERNAL THETA
      EXTERNAL PHI
      COMMON/PARAMETER/ALP1,ALP2,ALP3,ALP4,LAMBAD_PI
      DOUBLE PRECISION ALP1,ALP2,ALP3,ALP4
      DOUBLE PRECISION T_RF,LAMBAD_PI,THETA,PHI,T,S
      INTEGER N

      T_RF = 19.75
C      LAMBAD_PI = 1/26.03
```

```
      S = 0.0

      DO N=-1000, 10
        IF(N.EQ.0) GOTO 20
        S = S+THETA(T-T_RF*DBLE(N)-3.0)*LAMBAD_PI*PHI(T-T_RF*DBLE(N))
 20     CONTINUE
      ENDDO
      SUM2=S
      RETURN
      END FUNCTION
CC_____________________________________________________
      DOUBLE PRECISION FUNCTION THETA(X)
      IMPLICIT NONE
      DOUBLE PRECISION X

      IF(X<=0.) THEN
         THETA=0.
      ELSE
         THETA=1.
      ENDIF
      RETURN
      END FUNCTION

CCC _______________________________________
      DOUBLE PRECISION FUNCTION PHI(T)
      IMPLICIT NONE
      COMMON/PARAMETER/ALP1,ALP2,ALP3,ALP4,LAMBAD_PI
      DOUBLE PRECISION ALP1,ALP2,ALP3,ALP4
      DOUBLE PRECISION LAMBAD_PI,LAMBAD_MU,T
C      LAMBAD_PI = 1/26.03
      LAMBAD_MU = 1/2197.03

      PHI=(LAMBAD_PI*LAMBAD_MU)*(EXP(-LAMBAD_PI*T)-EXP(-LAMBAD_MU*T))
     +    /(+LAMBAD_MU-LAMBAD_PI)
      RETURN
      END FUNCTION
C_________________________________________________
      DOUBLE PRECISION FUNCTION INTSUM1(x)
      IMPLICIT NONE
      EXTERNAL SUM1
      EXTERNAL DGAUSS
```

```
COMMON/PARAMETER/ALP1,ALP2,ALP3,ALP4,LAMBAD_PI
DOUBLE PRECISION ALP1,ALP2,ALP3,ALP4,L,R,eps,x
DOUBLE PRECISION SUM1,DGAUSS,LAMBAD_PI

L = 10.
R = 70.
EPS = 0.0000001
intsum1 = DGAUSS(SUM1,L,R,EPS)
RETURN
END FUNCTION
```

Appendix E

Properties of CsI scintillators

Table E.1: Optical properties of the pure CsI scintillators used for the PIBETA calorimeter (Manufacturers: Bicron Corporation and Kharkov Institute for Single Crystals).

Quantity	Average Value
Density	$4.53\,\mathrm{g/cm^3}$
Radiation Length	1.85 cm
Refractive Index at 500 nm	1.80
Refractive Index at 315 nm	1.95
Nuclear Interaction Length	$167\,\mathrm{g/cm^2}$
$dE/dx\|_{\mathrm{min}}$	$1.243\,\mathrm{MeV/g/cm^2}$
Photonuclear Absorption (π^0 photons)	0.675 %
Light Attenuation Length	103 cm
Fast Component Wavelength	305 nm
Fast Component Decay Time	7 ns
Slow Component Wavelength	450 nm
Slow Component Decay Time	35 ns
Lower Wavelength Cutoff	260 nm
Fast-to-Total Light Output Ratio	0.76
Light Output	66.2 Photoel./MeV
Light Output Nonuniformity	+0.28 %/cm
Light Output Temperature Coefficient	$-1.56\,\%/^\circ\mathrm{C}$
Time Resolution (wrt PV tag)	0.68 ns
Stability	Slightly Hygroscopic

Bibliography

[1] (Particle Data Group), Phys. Rev. D 66, 2002.

[2] I.S. Towner et al, arXiv:nucl-th/9809087 29 Sep 1998.

[3] B.G. Erozolimsky et al, Sov. J. Nucl. Phys. 53:260-262,1991.

[4] M.B. Kreuz et al, arXiv:hep-ph/0312124, Sep 2002.

[5] P. Depommier et al. Nucl. Phys. B4 (1968) 189.

[6] W.K. McFarlane et al, Phys. Rev. D 43, 547(1985).

[7] G. Czapek et al., Pys. Rev. Lett. 70(1993) 17.

[8] B.B. Binon et al., Nucl. Instr. and Meth.332(1993) 419.

[9] F. Halzen et al, Quarks and Leptons, J. Wiley & Sons, 1984.

[10] T.D. Lee and C.N. Yang, Phys. Rev. 104, 254(1956).

[11] C. S. Wu et al., Phys. Rev. 105, 1413 (1957).

[12] R.P. Byron, Particl Phys. at the New Millennium, Springer-Verlag NY, 1996

[13] S.S. Gershtein, I.B. Zeldovich, Soviet Phys. Jetp 2,576(1956); R.P. Feynman, M. Gell-Mann, Phys. Rev. 109, 193(1958).

[14] A. Sirlin. Phys. Rev. 164, 5(1967).

[15] Elementary Particle Physics, Addison-Wesley Pub. Company, Inc (1964).

[16] A. Sirlin. Rev. Mod. Phys. 50, 573 (1978).

[17] A. Sirlin, Letter to D. Pocanic, 19 Mar. 1989.

[18] Maple 6, Waterloo Maple Inc.

[19] W.J. Marciano & A. Sirlin, Phys. Rev. Lett. 56(1986) 1(22:25).

[20] W. Jaus, Phys. Rev. D 63, 053009(2001).

[21] K.L. Brown, D.C. Carey, Ch. Iselin, and F. Rothacker, Transport: A Computer Program for Designing Charged Particle Beam Transpost Systems, CERN Yellow Reposts 73-16/80-04 (CERN, Geneva, 1973/1980).

[22] K. L. Brown, Ch. Iselin, and D. C. Carey, Decay Turtle, CERN Yellow Repost 74-2 (CERN, Geneva, 1974).

[23] U. Rohrer, Computer Control for Secondary Beam Lines at PSI, PSI Annual Report, Annex I (1988) 7.

[24] E. Frlez et al. Design, Commissioning and Performance of the PIBETA Detector at PSI, hep-ex/0312017, Submitted to Nucl. Instrum. & Meth.

[25] H. Kobayashi, A. Konaka, K. Miyake, T. T. Nakamura, T. Nomura, N. Sasao, T. Yamashita, S. Sakuragi, and S. Hashimoto, Kyoto University Preprint KUNS-900 (1987).

[26] S. Kubota, H. Murakami, J. Z. Ruan, N. Iwasa, S. Sakuragi, and S. Hashimoto, Nucl. Inst. and. Meth. A 273 (1988) 645.

[27] S. Kubota, S. Sakuragi, S. Hashimoto and J. Z. Ruan, Nucl. Inst. and Meth. A 268 (1988) 275.

[28] E. Frlez et. al. Nucl. Instr. and Meth. A 459(2001).

[29] V. V. Karpukhin et. al. , Nucl. Instrum. Methods A 418 (1998) 306.

[30] V. V. Karpukhin et. al. , Instrum. Exp. Tech. 42 (1999) 335.

[31] Bicron Corp. Catalog (Bicron Corp, Newbury, 1989).

[32] E. Frlez, et. al. Nucl. Inst. and Meth. A 440 (2000) 57.

[33] K. A. Assamagan, PhD Thesis (University of Virginia, Charlottesville, 1995).

[34] R. Brun et al., GEANT 3.21 DD/EE/94-1 (CERN, Geneva, 1994).

[35] F. James et al., MINUIT 94.1 D506 (CERN, Geneva, 1994).

[36] The Pion Beta Decay Experiment and A Remeasurement of the Panofsky Ratio. T. Flügel. Doctoral Dissertation.

[37] R. Gordon. IEEE Transactions on Nuc. Sci. Vol.NS-21, June 1974.

[38] W. J. Marciano, Phys. Rev. Lett. 71, 3629 (1993).

[39] E. Frlez et. al. hep-ex/0312017